INVESTIGATION ON NITRIC OXIDE AND SOOT OF BIODIESEL AND CONVENTIONAL DIESEL USING A MEDIUM DUTY DIESEL ENGINE

A Dissertation

by

HOSEOK SONG

Submitted to the Office of Graduate Studies of
Texas A&M University
in partial fulfillment of the requirements for the degree of

DOCTOR OF PHILOSOPHY

May 2012

Major Subject: Mechanical Engineering

Investigation on Nitric Oxide and Soot of Biodiesel and Conventional Diesel using a Medium Duty Diesel Engine

INVESTIGATION ON NITRIC OIXDE AND SOOT OF BIODIESEL AND CONVENTIONAL DIESEL USING A MEDIUM DUTY DIESEL ENGINE

A Dissertation

by

HOSEOK SONG

Submitted to the Office of Graduate Studies of
Texas A&M University
in partial fulfillment of the requirements for the degree of

DOCTOR OF PHILOSOPHY

Approved by:

Chair of Committee,	Timothy J. Jacobs
Committee Members,	Jerald A. Caton
	Je-Chin Han
	Sergio C. Capareda
Head of Department,	Jerald A. Caton

May 2012

Major Subject: Mechanical Engineering

ABSTRACT

Investigation on Nitric Oxide and Soot of Biodiesel and Conventional Diesel using a Medium Duty Diesel Engine. (May 2012)

Hoseok Song, B.S., Inha University, South Korea;

M.S., Kansas State University

Chair of Advisory Committee: Dr. Timothy Jacobs

Biodiesel has been suggested as an alternative fuel to the petroleum diesel fuel. It beneficially reduces regulated emission gases, but increases NO_x (nitric oxide and nitrogen dioxide) Thus, the increase in NO_x is the barrier for potential growth of the biodiesel fuel. In general, NO_x formation is dominated by flame temperature. Interestingly, soot can play a role as a heat sink as well as a heat transfer media to high temperature gases. Thus, the cooling effect of soot may change the flame temperature and therefore, NO_x emissions.

In this study, emphasis is placed on the relationship between soot and NO (Nitric oxide) formation. For the experimental study, a metallic fuel additive is used since barium is known to be effective to suppress soot formation during combustion. The barium additive is applied to #2D (Number 2 diesel fuel) by volume basis: 0.1, 0.25 and 0.5 %-v, and to the palm olein oil by 0.25 %-v. All the tests are carried out in a four-cylinder medium duty diesel engine, 4045 DI diesel engine, manufactured by John

Deere. For the analysis, an analytical model is used to estimate combustion temperature, NO concentration and soot emissivity.

The results show that NO concentration does not have the expected trade-off relation with soot. Rather, NO concentration is found to be more strongly affected by ambient temperature and combustion characteristics than by soot. The results of the analytical model show the reasonable NO estimation and the improvement on temperature calculation. However, the model is not able to explain the detailed changes of soot emissivity by the different fuels since the emissivity correlation is developed empirically for diesel fuel.

DEDICATION

To my parents and wife

ACKNOWLEDGEMENTS

First and foremost, I would like to gratefully and sincerely thank my advisor Dr. Timothy Jacobs for his guidance, understanding, patience, and friendship during my graduate study at Texas A&M University. It has been an honor to be his Ph. D. student. I really appreciate all his contribution of ideas and funding to make my research experience possible. I am also thankful for the enthusiasm he has provided as an internal combustion researcher.

I would like to thank all of the members of the Advanced Engine Research Laboratory. They have provided me with good advice and collaboration for my research. I am especially grateful for Brandon Tomkins, Josh Bittle, and a former member, Jason Esquivel, as they helped me acquire much valuable lab experience and many skills.

I also would like to thank Dr. Jerald Caton, Dr. Je-chin Han, and Dr. Sergio Capareda for their guidance and support in accomplishing my graduate career. It has been an honor to have them as my committee members.

Lastly, I would like to thank my family for all their love and encouragement. They have patiently stood beside me and encouraged me to achieve this career goal. I also would like to express special words to my wife, Yirang, for providing me with support and love, and being with me during my Ph. D. study. This big step in my life would not be forwarded and happy without them.

NOMENCLATURE

Symbols

A	Surface area
h	Specific enthalpy
h_c	Heat transfer coefficient
$\dot{m}_i$	Mass flow rate into the system.
m	Mass of burned fuel-air mixture
p	Cylinder pressure
$\dot{Q}$	Heat transfer rate
Q_R	Radiation heat transfer
R	Gas constant
r_b	Burned fuel mass fraction
T	Temperature
T_R	Radiation temperature
T_W	Wall temperature of a cylinder
t	Time
u	Specific internal energy
V_c	Cylinder volume
$\overline{v}_p$	Mean piston speed
ε	Emissivity
σ	Stefan-Boltzmann constant.

θ	Crank angle
ϕ	Fuel/air equivalence ratio

Subscripts

a	Air
b	Burned gas
g	Gas
o	Initial
u	Unburned
rad	Radiation

Notation

Δ	Difference
[ ]	Concentration, moles/cm^3
%-v	Volume percentage

Abbreviations

A/F	Air/fuel ratio
BA	Barium additive
B20	20%-v biodiesel with 80%-v diesel fuel
B100	100%-v biodiesel
CN	Cetane number

FSN	Filter smoke number
ID	Ignition delay
MBT	Maximum brake torque
SOI	Start of injection
TDC, ATDC, BTDC	Top dead center, after TDC, before TDC

The nomenclature is made based on the work by Heywood [1].

TABLE OF CONTENTS

Page

LIST OF FIGURES

Page

LIST OF TABLES

Page

1 INTRODUCTION

1.1 Motivation

Global warming has emphasized the need to reduce greenhouse gases. Energy security in the United States has also become an imminent issue. In order to solve these problems, various alternative methods have been suggested, and one of these is biodiesel fuels. Since biodiesel fuels are produced from domestic natural sources through the transesterification process [2], the strong dependence on foreign countries can be reduced. Also, biodiesel, due to its participation in a carbon cycle and its use in ultra-efficient diesel engines, is a type of alternative energy that contributes toward solving global warming and energy insecurity. The use of biodiesel fuels emits carbon dioxide (CO_2) through combustion, and their feedstock sources absorb CO_2 from the atmosphere through photosynthesis in a closed-loop CO_2 cycle as shown in Figure 1, while the use of petroleum diesel fuels builds up CO_2 in the atmosphere. Therefore, using biodiesel fuels can lead to reducing the accumulation of CO_2 in the atmosphere [3]. Additionally, the use of biodiesel fuels is shown to reduce carbon monoxide (CO), hydrocarbon (HC) and particulate matter (PM) emissions compared to conventional diesel fuels. These reductions in pollutants are critical for also maintaining healthy air in the United States.

This dissertation follows the style of Journal of Engineering for Gas Turbines and Power.

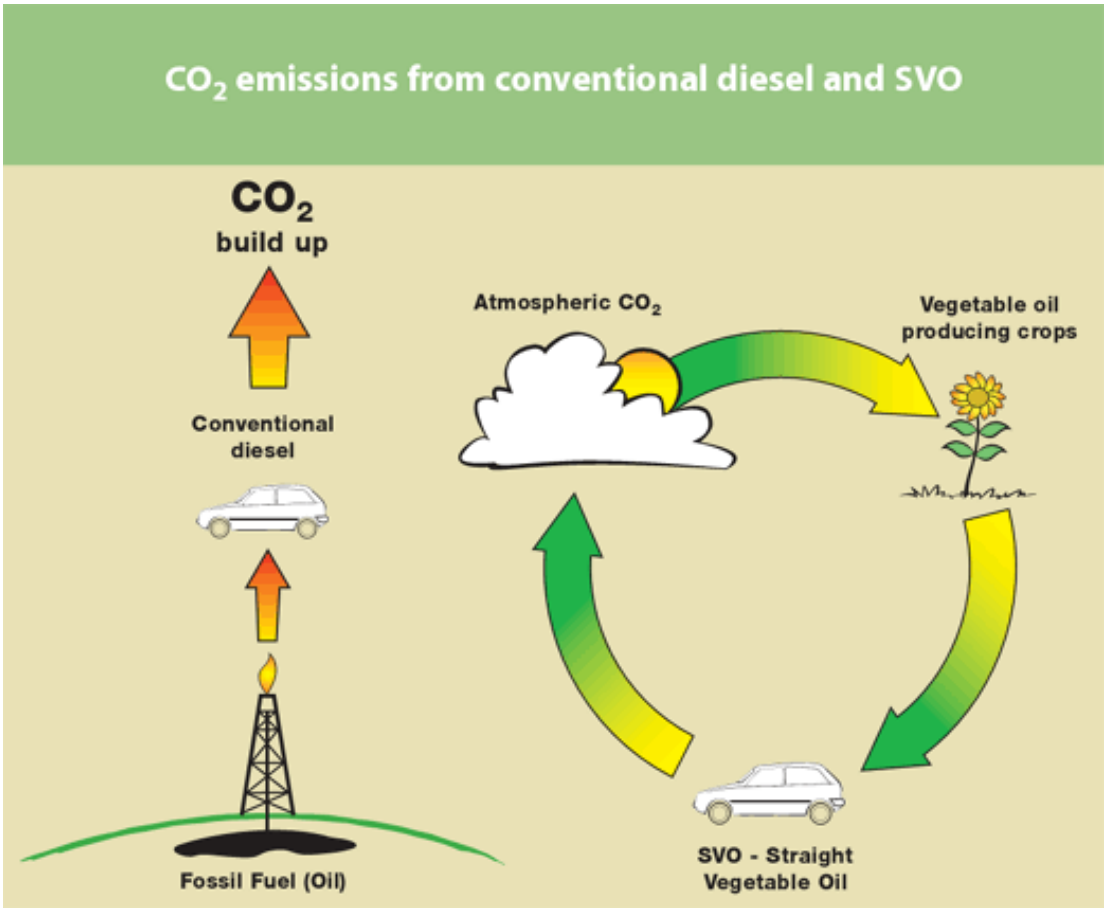

Figure 1 Comparison of CO_2 lifecycle between petroleum diesel and biodiesel fuels. (Source: biodieselprocessor.org)

The use of biodiesel, however, has been reported to increase oxides of nitrogen, NO_x, which could lead to increased tropospheric ozone formation, compared to the use of petroleum diesel fuel. The relative increase in NO_x is believed to largely result from thermal formation mechanisms; that is, relatively higher post-flame gas temperatures with biodiesel are likely the dominant factor to causing relatively higher NO_x formation [3], [4]. Correspondingly, post-flame gas temperature might be affected by the

concentration of soot that is normally formed during diesel combustion; higher soot concentrations increase radiation heat transfer, resulting in a reduction in flame temperature and thus in post-flame gas temperatures. Biodiesel, with its lower in-cylinder soot formation, tends to have lower radiation heat transfer than petroleum diesel does. This lower radiation heat transfer may partially contribute to higher post-flame temperatures of biodiesel, and thus higher NO_x emissions with biodiesel. However, this mechanism and the contribution of the radiation heat transfer to the biodiesel NO_x are not completely understood [3].

Therefore, understanding the NO_x emission in a diesel engine is essential to solve the problems in biodiesel combustions. The current study is focused on investigating the relationship between NO_x emissions and soot radiation in a diesel engine. Also, it is expected to establish the basis of a better combustion diesel engine with lower NO_x emissions.

1.2 Background Knowledge

1.2.1 Diesel Engine Combustion

Since the inception of the first diesel engine invented by Rudolf Diesel in the late 19^{th} century, diesel engines have been used in various sectors due to their higher fuel efficiency, durability, and longevity, compared to gasoline engines. The wide application of diesel engines includes passenger cars, trucks, construction machines, power generators, ships, locomotives, and airplanes.

There are emission problems, however, that diesel engines produce more particulate matter because combustion takes place in heterogeneous air-fuel mixture. Soot is a primary component of particulate matter. Moreover, diesel engines may produce more NO_x depending on engine operating condition, compared with gasoline engines. Interestingly, NO_x versus particulate matter trade-off is well known [4]. Thus, it is difficult to control and decrease both NO_x and particulate matter at the same time.

As emission regulations become more stringent over the years, the regulations require combustion engines to produce less and less emission gases. So the future of diesel engines is strongly dependent on the regulations. Thus, many studies about particulate matter and NO_x emissions from diesel engines have been carried out to meet these new regulations.

1.2.2 Biodiesel

Biodiesel has been suggested as an alternative fuel to the conventional diesel fuel and is considered to be renewable since its feedstock is produced through the

photosynthesis process with the energy from sunlight and carbon dioxide [2]. In addition to this benefit, biodiesel can be used in its pure form as well as a form blended with conventional diesel fuel without any engine modifications.

In terms of air pollutions, biodiesel can benefit in decrease of the regulated emissions such as hydrocarbon (HC), carbon monoxide (CO), and particulate matter (PM) [2]. Also, biodiesel can relatively reduce life-cycle CO_2 emissions because of the materials produced through the photosynthesis process.

On the other hand, biodiesel can lead to the increase in NO_x emissions [3], [5], [6]. Since NO_x has the direct effects on human health and an important role in atmospheric chemistry [7], there have been many studies to understand the increase in NO_x in biodiesel combustion. Thus, there are various explanations for NO_x formation in biodiesel combustion, which can be summarized into 4 categories as following:

1. Biodiesel has 5 to 10 percentage higher bulk modulus than number 2 diesel (#2D) fuels [2]. The higher bulk modulus can cause faster pressure propagation in the fuel system of engines and eventually, lead to earlier injection. Advanced injection yields in turn earlier start of combustion and, thus, leads to longer residence time and higher in-cylinder temperature [8]. As a result, NO_x emissions might be increased [1], [3]. However, the advanced injection is not observed in common rail fuel system [9].

2. Biodiesel has higher cetane number than conventional diesel fuels, which causes earlier ignition [10]. This yields the combustion products to have a

longer residence time at high temperatures. Consequently, biodiesel combustion might be able to produce more NO_x.

3. Biodiesel is an oxygenated fuel [2]. The presence of oxygen in fuel likely helps less production and more oxidation of soot [3], [10], and consequently reduces the radiation heat loss from the combustion flame to surroundings. Soot might change the flame temperature, which is estimated to be 50 to 60 K [4]. Thus, biodiesel may have higher flame temperature and can lead to increase in thermal NO, which is related to the radiation [8].

4. The difference in fuel chemistry may have the prompt NO mechanism [2]. For this reason, biodiesel fuel might have different chemical kinetics pathways to form NO_x.

1.2.3 NO Formation

NO is one of the regulated emission gases and is regulated with NO_2 as NO_x. The EPA (Environmental Protection Agency) standard for combined NO_x and HC is 4.0 g/kW·hr, which is applicable to Tier 3 non-road diesel engines with the rated power ranging from 130 to 225 kW. As mentioned previously, the standard becomes more stringent.

Among those emission gases, NO is of interest in this study. In general, there are three mechanisms of NO formation; 1) thermal NO formation, 2) prompt NO formation, and 3) NO formation from nitrogen in the fuel.

First of all, NO formation from fuels is usually not considered in internal combustion studies [1], [11], since diesel and gasoline fuels contain little amount of nitrogen.

Regarding the prompt mechanism, Fenimore [12] shows the faster and transient formation of NO in the primary reaction zone where hydrocarbon is burning. It is shown that the richer fuel-air mixture, the more NO in the primary zone. However, when the fuel-air mixture is lean, the NO formation in the primary zone is negligible. Even though rich heterogeneous pockets in the fuel-air mixture might support prompt mechanism, it is widely acknowledged that thermal mechanism is the dominant form of NO formation in diesel combustion.

Since diesel combustions undertake at high temperatures, most of the NO formation is explained via the thermal mechanism, which is also called the extended Zeldovich mechanism summarized by Lavoie et al.[13]:

$$O + N_2 \leftrightarrow NO + N \qquad 1.1$$

$$N + O_2 \leftrightarrow NO + O \qquad 1.2$$

$$N + OH \leftrightarrow NO + H \qquad 1.3$$

The first reaction requires high energy and is strongly dependent on high temperature, since the N_2 has triple bond. That is the reason, again, why this mechanism

is referred to as the thermal NO mechanism [14]. This thermal mechanism is usually unimportant under 1800 K [15].

Based on the thermal NO mechanism, NO concentration is generally calculated with an assumption that the reaction rates in a flame are so fast that the burned gases are almost in thermodynamic equilibrium. Thus, O, O_2, H, OH, and N_2 are calculated with N in quasi-steady state.

1.2.4 Soot Production in Diesel Engines

Diesel particulate matter (PM) is composed primarily of carbonaceous material (soot), whose fraction in particulates is higher than 50 % [1], [16]. The EPA standard for PM is 0.2 g/kW·hr, which is the limit to the current test engine. Soot is known to be inherent in diesel engines [17] due to their heterogeneous combustion. An average soot particle size of 25 nm diameter [18] and a certain amount of soot in exhaust gases causes a black smoke. The small size of soot is likely to be inhaled into, and deposited in human lungs. As a result, it may cause lung cancer [19]. Also, it is harmful to engines since the deposition of soot deteriorates engine performance.

Soot is formed from unburned fuel in rich mixture regions at high temperature, and the formed soot is oxidized at the same time. Thus, the exhausted soot in diesel engines is the result of soot formation and oxidation. Soot is formed in the order of milliseconds, and the complex diesel combustion makes it difficult to understand the detailed processes of soot production [1]. However, soot production is routinely summarized into six processes: 1) pyrolysis, 2) nucleation, 3) surface growth, 4)

coalescence, 5) agglomeration, and 6) oxidation. In many literatures, these processes are explained similarly in detail as following.

In fuel pyrolysis, fuels change their molecular structure at high temperature without oxidation [16]. Through the pyrolysis process, gas-phase precursors of soot are formed such as unsaturated hydrocarbons, and polycyclic aromatic hydrocarbons (PAH) [20]. Via nucleation, the gas-phase species condense to form the first recognizable soot particles, which are called soot nuclei.

After the soot nuclei are formed, the particles grow in mass and volume through the following processes: surface growth, coalescence, and agglomeration. Through the surface growth process, the soot nuclei gain mass from receiving gas-phase hydrocarbons on their hot reactive surface [16]. This process increases soot mass, but the number of particles does not change.

Coalescence is the process of combining soot particles. Spherical particles collide with each other and combine together into new spherical particles. Opposite to surface growth, the total mass of soot particles does not change, while the number of soot particles decreases.

Like coalescence process, agglomeration is the process of combining particles to form soot agglomerates, which are called soot particles. They are usually in chain-like structure, but in some cases in cluster structure. However, the individual particles maintain their shape.

While the five formation processes are occurring, soot is oxidized by the attack of oxidizing species such as O_2 and OH radical. It is known that soot is oxidized mainly

by OH under fuel-rich and close-to-stoichiometric condition [1], while soot is oxidized by both O_2 and OH [21] under lean condition.

The soot from the competition between soot formation and oxidation plays an important role as the source of radiation heat flux in diesel combustion. The radiation heat transfer is observed to be on the same order of the convection heat transfer during diesel combustion, whose fraction of total heat transfer is about 40 % [22]. As mentioned above, the soot radiation likely reduces the flame temperature and, consequently, reduces the thermal NO formation. This relation is investigated in the current study.

1.2.5 Additives

In order to reduce soot emissions, there have been various attempts to decrease soot emission from diesel engines. One of these attempts uses metallic additives, predominantly, a barium additive. Barium is one of alkaline earth metals, which is known to be one of the most effective metals in reducing soot formation [23], [24].

Many studies show that barium suppresses soot emissions. Norman et al. [25] show that a barium additive reduces opacity up to 30 to 55 %, and that more cleanliness and less wear of most engine parts are caused by the barium additive. Similar experimental results are shown by Truex et al. [26] by using Lubrizol 556 barium additive. Fuels are treated with 0.25 %-v of the additive. The barium additive reduces exhaust opacity up to 30 to 40 % measured by a smoke meter. The opacity reduction does not correlate with total particulate mass because the added barium is emitted in

particulate emissions. The disagreement between the opacity and the particulate mass is observed by Draper et al. [27]. Thus, both studies suggest that the smoke suppression may be due to the change in chemical composition or size distribution of soot by the additive. Additionally, it is observed that the carbonaceous material is reduced to about 30% in the mass of emission by using the barium additive. So it is reasonable that the reduction of carbon material is related to the reduction of opacity. In other words, the barium additive is effective to reduce carbon materials, and, consequently, to reduce opacity.

Cotton et al. [23] suggest a chemical mechanism that, when the concentration of hydroxyl radical (OH) is below the equilibrium (diffusion flame), the additive catalyzes the dissociation of water and hydrogen to produce hydroxyl radicals, which cause the oxidation of soot. In an opposite situation (premixed flame zone), the additive catalyzes the recombination of radicals so that the concentration is reduced to equilibrium. It is shown that barium, NO, and SO (sulfur oxide) catalyze the dissociation of water and hydrogen to produce hydroxyl radicals in diffusion flames, so the number of barium, NO, and SO are decreased.

Bluweicz et al. [24] shows the ionization effect that the ionization of the barium in the flame decreases the soot collection rate, the number of soot precursors, and the particle size. They conclude that the anti-soot effects of barium additive are caused by the higher ion level due to the additive compared to that of the natural flame. They suggested that adding the barium additive may reduce the number of hydrocarbon nuclei ($C_nH_m^+$ $\mathrm{C_nH_m^+}$), and this reduction causes the number of solid charged particles to be

reduced. Also, the increase of electron by adding barium interrupts the coagulation of ionized solid particles, and, thus, causes the particle size to become smaller. Thus, adding barium additive reduces the formation of soot, and also reduces the particle size.

Haynes et al. [28] shows the both ionization and chemical mechanisms by using the barium additive. They show that the barium can produce sufficient ions to suppress the coagulation process of soot precursors. Also, it is shown that the barium additive increases OH which helps oxidation of soot, especially gaseous hydrocarbons, resulting in smaller soot particles. Thus, the barium additive affects both soot formation and oxidation during combustion. Also, it can be interpreted that the soot radiation might be reduced since the barium additive can shorten the presence time of soot during combustion.

For above reasons, a barium additive is selected to control soot formation in the current study and to possibly investigate the relation between soot radiation and NO formation.

1.2.6 Analytical Models

In order to better understand combustion processes inside an internal combustion engine, a zero-dimensional simulation method is often used. This model does not have spatial resolution in simulation of combustion processes, so it is called a zero-dimensional model [29]. Recently, multidimensional modeling has been dominant because it can simulate combustion phenomena visually and predict combustion results in three dimensions; so it requires high computer power due to its complexity.

A zero-dimensional model, however, is still selected in engine research because it is simple, but useful for parametric investigations on heat release and heat transfer rates with experimental data [29], [30], [31]. The zero-dimensional model to calculate heat release is a diagnostic, not a predictive, model; it needs input data such as in-cylinder pressure. For simplicity, it is generally assumed that the contents in the cylinder chamber are uniform in pressure and temperature at any instant. This assumption facilitates calculations of the model to use the first law of thermodynamics, conservation of mass, and ideal gas law.

One of the early works of the zero-dimensional models is accomplished by Krieger et al.[30]. The authors introduce a single zone model to analyze diesel engines. All the thermal properties of products and reactants are calculated by using the correlations based on JANAF Tables [32].

Krieger et al. [30] also suggest a two-zone model: burned and unburned zones. The authors estimate the initial flame temperature where the combustion process begins, by using the adiabatic flame temperature, which means that the enthalpies of the burned zone and unburned zones are equal. The results show the change of temperature, volume and burning fuel mass fraction for each zone. Similar studies of the two-zone model are carried out by others [33], [34], [35].

Based on the concept of the previous models, a two-stage model is developed by Szekely et al. [31]. It is composed of four zones: the unburned rich- and lean-zones, and the burned rich- and lean- zones. Compared to a single zone model, it estimates more realistic gas temperatures which allow the modeling of thermally formed NO and

radiation heat flux. Similar to the other zero-dimensional models, temperature gradient, pressure wave, and non-equilibrium gas composition are ignored in each zone. The authors also investigate radiation heat transfer by using the gas emissivity correlation suggested by Sitkei [36], and the soot emissivity correlation suggested by Kunitomo et al. [37].

1.3 Objective

As introduced above, the increase in NO emission with biodiesel combustion is barrier to its future as an alternative fuel. Of the possible explanations, the soot radiation effect seems to be the dominant factor in NO formation. Thus, it is essential to understand the NO increase in the biodiesel fuel combustion and the relation between NO and soot radiation. So the current study is carried out in majorly three parts: diesel fuel test, biodiesel test, and analytical modeling.

In the first study, the diesel fuel is prepared and mixed with the barium additive. It is designed to investigate the soot effects on NO formation, since the additive is effective to reduce the soot concentration. Also, this study is to investigate the changes of soot and NO emissions with the various engine speeds and loads, which cause different combustion characteristics.

The study with the biodiesel fuel is designed to verify the possible effects of the barium additive on NO emissions, possibly, excluding the soot effects. The biodiesel is selected for this study because it produces lower soot in general and, thus, weakens the soot effects on NO formation.

Biodiesel fuels are also used to study the trends of NO and soot emissions by varying the biodiesel concentration and also the engine operating conditions. This study is to understand what causes NO to increase among combustion characteristics, biodiesel fuel effects, and other possible factors.

Along with the experimental work, the two-stage model is programed in FORTRAN to interpret the combustion processes in terms of combustion temperature, heat transfer rate, and apparent heat release rate. The priority of the two-stage model is to estimate the NO concentration, which would be used in a closed-loop control strategy for NO emission. However, it is possible that the temperature calculation does not capture the details of physical combustion processes since the calculation is manipulated with the heat transfer factor to match the combustion duration [31].Also, this study verifies the ability/inability of the analytical model to estimate soot emissivity, which cannot be measured through experiments.

In summary, this research is carried out to show:

1. The relation between soot and NO concentrations.
2. The trend of NO with combustion characteristics.
3. The causes for the biodiesel NO increase.
4. NO and soot emissivity estimation through the two-stage model.

2 EXPERIMENTAL METHODOLOGY AND APPARATUS

2.1 Test Engine

The test engine for this study is a Tier 3 medium duty diesel engine, 4045 DI Diesel Engine, manufactured by John Deere. Detailed specifications of the engine are shown in Table 1.

Engine torque is measured with a direct current (DC) dynamometer manufactured by General Electric. The engine is controlled by using a control unit developed by Drivven, San Antonio, Texas, enabling control of the amount of fuel injected, start and duration of injection, exhaust gas recirculation (EGR) level, and fuel injection pressure.

Table 1 Specifications of the test engine.

	Value
Displacement	4.5 L
Bore	106 mm
Stroke	127 mm
Compression Ratio	16.57 : 1
Peak Power	115 kW at 2400 rev/min
Peak Torque	575N·m at 1400 rev/min
Number of Valves/Cylinder	4
Fuel System	High pressure common rail, direct injection
Air System	Variable geometry turbo-charger (VGT) with exhaust gas recirculation (EGR)

2.2 Test Fuels

The test fuels are the commercially available #2 diesel (#2D) as a base fuel and the palm olein oil biodiesel. For the diesel fuel test, #2D is mixed with the barium additive (Lubrizol 565), which is provided by Lubrizol Corp., by volume basis: 0.0, 0.1, 0.25, 0.5 %-v. The case of 0 % means the pure #2D without the barium additive. The fuel mixture is prepared based on the manufacturer's recommended concentration, which is 0.25 %-v to a test fuel.

For biodiesel tests, the palm olein biodiesel (Green Earth Fuels, Houston, Texas) is used as B100, which means 100 %-v biodiesel. The biodiesel is mixed with the #2D by 20 to 80 %-v to make B20 fuel. For the B100 case, 0.25 %-v of the barium additive is applied to study the possible effects of the barium additive on NO emission.

Table 2 Summary of properties of diesel fuels.

Property (Units)	**Value**			**ASTM Method**
	#2D	#2D with 0.1% BA	#2D with 0.25% BA	
IBP (°C)	173.4	172.3	171.8	ASTM D86
FBP (°C)	340.5	340.1	339.6	ASTM D86
Lower Heating Value (MJ/kg)	43.008	42.999	42.979	ASTM D240N
Density (g/L)	825.5	825.6	826.3	ASTM D4052s
Viscosity (cSt)	2.247	2.256	2.259	ASTM D445 40c
Carbon Weight (%-weight)	85.81	86.09	86.0	ASTM D5291
Hydrogen Weight (%-weight)	13.41	13.53	13.4	ASTM D5291
Sulfur (ppm)	5.3	7.6	11.0	ASTM D5453
Cetane Number	51.3	50.8	48.9	ASTM D613
Saturate Con.(%-vol)	74.2	71.2	73.1	ASTM D1319
Olefin Con. (%-vol)	1.1	2.0	1.6	ASTM D1319
Aromatic Con.(%-vol)	24.7	26.8	25.3	ASTM D1319

Table 3 Summary of properties of biodiesel fuels.

Property (Units)	Value			ASTM Method
	B20	B100	B100 with 0.25% BA	
IBP (°C)	174.7	329	-	ASTM D86
FBP (°C)	343.9	357	-	ASTM D86
Lower Heating Value (MJ/kg)	41.6	37.193	-	ASTM D240N
Density (g/L)	844.6	875.7	-	ASTM D4052s
Viscosity (cSt)	2.763	4.741	-	ASTM D445 40c
Carbon Weight (%-weight)	84.06	76.18	-	ASTM D5291
Hydrogen Weight (%-weight)	13.08	12.37	-	ASTM D5291
Sulfur (ppm)	5.8	2.4	-	ASTM D5453
Cetane Number	56.5	64.3	-	ASTM D613
Saturate Con.(%-vol)	76.8	-	-	ASTM D1319
Olefin Con. (%-vol)	1.1	-	-	ASTM D1319
Aromatic Con.(%-vol)	22.1	-	-	ASTM D1319

The test fuels are analyzed using American Society of Testing and Materials (ASTM) standard procedures by the Southwest Research Institute. The fuel properties are tabulated in Table 2 and Table 3. The B100 with 0.25 % is not analyzed because the properties are likely to be similar to them of B100 like the #2D cases.

2.3 Data Measurements

All data acquisition and process control tasks are managed by a PC executing LabVIEW. The data acquisition system is composed of two parts: high and low speed systems.

The high-speed system is for the crank angle-resolved measurements such as in-cylinder pressure, needle lift profile, and injector current. The high-speed system is composed of NI (National Instruments) PXI-6123, PXI-PCI 8331, BNC-2090A

connector block, and the sensors. In general, the PC controls the PXI-6123 through PXI-PCI 8331. All the data are collected through BNC-2090A and sent to PXI-6123 module, which converts analog to digital signals.

The crank angle is measured using an optical encoder, which is mounted onto the front of the crankshaft. The encoder sends two channels to the high speed system. The first channel sends out a pulse for every 0.2 degree, and the second channel outputs one pulse for every rotation of the encoder, when the encoder is at 133 degrees before TDC. This offset is determined by using another hall-effect sensor carefully aligned with TDC.

According to the crank angle measured by the encoder, the in-cylinder pressure measurement is carried out using a piezoelectric pressure transducer (model: Kistler 6056A), which is mounted in #1 cylinder. A Kistler charge amplifier converts the small current output from the transducer to a voltage signal, which is recorded based on the crank angle resolution. Note that the in-cylinder pressure from #1 cylinder is used for data analysis, since the cylinder is most representative one out of 4 cylinders. This is justified through turning off one injector out of four at a time. The results show that the injector in #1 cylinder has the fuel amount closet to one quarter of the total fuel. The cylinder pressure data is the average of 300 engine cycles.

The needle lift profile is measured using the needle lift senor based on the eddy current principle. The sensor produces a linear electrical signal proportional to the distance of the needle from it. Along with the needle lift profile, the injector current is also measured using a current clamp.

For the low-speed system, sensors are connected to two Measurement Computing Corporation DAS6031 model 16 channel data acquisition boards for “low-speed”, or time-resolved, measurements. The low speed system records the relatively slow changing data such as emission gases, temperatures, smoke numbers, air and fuel flow rate. The each measurement is explained in the following.

Temperature of the intake manifold is measured by using a K-type thermocouple, which can measure temperatures up to 260 ^{o}C within an error of 2.2 ^{o}C. Temperatures of the exhaust manifold, post turbocharger, and pre compressor are measured by using high temperature thermocouples (model: T-26) manufactured by Temprel Inc. They can measure temperatures up to 900 ^{o}C with an error of 1.1 ^{o}C.

Pressures of the intake manifold, exhaust manifold, post turbocharger, and pre compressor are measured by using strain gauge pressure transducers (model: PX309-050A5V) manufactured by Omega Engineering, which have a pressure range from 0 to 3.45 bar with an error of 0.25 %.

The AVL 415S Smoke Meter used in this study is a filter-type smoke meter for measuring the soot content level in the exhaust gas from an internal combustion engine, which is passed through a filtered paper. Five samples are taken and averaged per engine condition for each exhaust smoke concentration. The smoke meter measures the reflectance of the paper filter as it is tuned for carbon black, and the result of the reflectance is displayed as Filter Smoke Number (FSN), which is a relative value and ranges from 0 to 10.

The emission gases are measured by using an automotive emission analyzer system, MEXA-7000 manufactured by HORIBA Inc., which measures the concentration of carbon monoxide (CO), carbon dioxide (CO_2), nitric oxide (NO), oxygen (O_2) and total hydrocarbon (THC) in exhaust gas from engines. Figure 2 shows the gas flow in the system. The raw emission samples from the exhaust pipe are filtered at 190 ^oC by the heated pre-filter and sent into the oven type heated analyzer (OVN) also at 190 ^oC, which is composed of THC and NO analyzers and is located separately from the system rack.

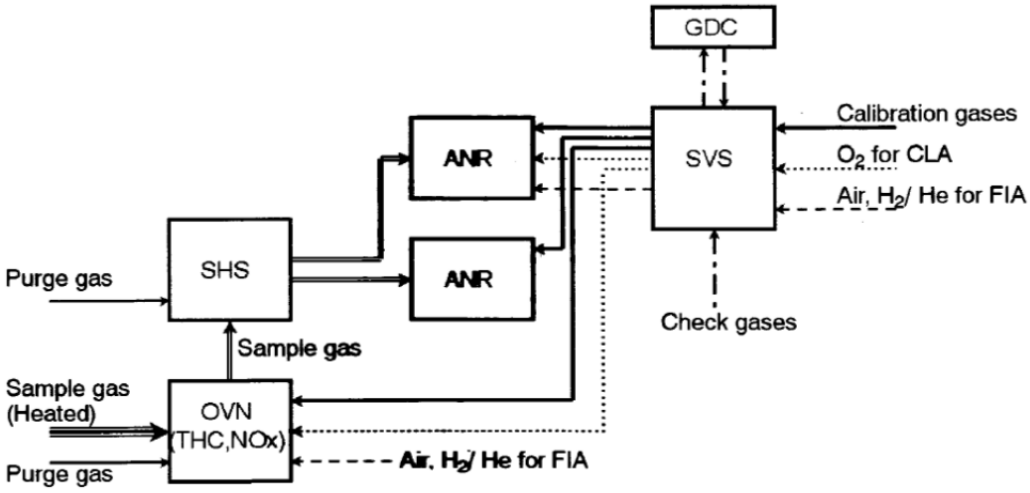

Figure 2 Exhaust gas flow in the emission gas analyzer.

The gas line for THC is maintained at about 190 ^oC to prevent condensation of heavy hydrocarbons and NO_x because the boiling temperature of hydrocarbons ranges from 116 to 191^oC. THC is measured by using the flame ionization method. The sampled gas is introduced into a hydrogen flame inside the analyzer. Then, the hydrocarbons in the sample produce ions when they react in the hydrogen flame. The

produced ions are detected by a metal collector, and resultant output voltage is measured, which is proportional to the concentration of the hydrocarbons.

NO analyzers first converts water soluble NO_2 to NO in a heated sample conversion module. This is done within the instrument, just prior to the reaction chamber. Then, NO is measured using the chemiluminescence detector, which is the industry standard method of measuring NO concentration. This method uses the reaction between NO and ozone (O_3), which produces light. The emitted light is measured by a photo multiplier tube (PMT) and is proportional to NO. Thus, NO can be measured based on the chemiluminescence method.

After measuring THC and NO, the sample gas is cooled down to condensate water at 5 ^{o}C by the sample handling unit (SHS) as shown in Figure 2.

The dehumidified sample gas is transferred to the rack for non-heated analyzer module (ANR). This system is composed of CO/CO_2 analyzer and O_2 analyzer. The analyzer system measures the concentrations of CO/CO_2 based on non-dispersive infrared detector (NDIR. The detector uses the infrared light absorption of CO/CO_2. The analyzer shines an infrared beam through a sample cell and measures the amount of infrared absorbed by the sample at the necessary wavelength. Thus, the analyzer is able to measure the volumetric concentration of CO/CO_2 in the sample gas.

The concentration of O_2 is measured by using magnetopneumatic method, which uses the magnetic characteristic of O_2. The analyzer passes O_2 to an uneven magnetic field, where the O_2 is drawn to the stronger side of the field. The O_2 causes the pressure

rise based on a non-magnetic gas (e.g., nitrogen) into the analyzer. The differential pressure between two gases is measured and is proportional to the concentration of O_2.

2.4 Methodology

For this study, the maximum brake-torque (MBT) timings are searched by varying the start of injection timing with diesel #2 D at 1400 rev/min with 50 and 250 ft-lbs, and at 2400 rev/min with 150 ft-lbs. Based on the found MBT timings, all the tests are carried out.

The diesel fuels are mixed with the barium additive to control the soot formation during combustion processes. This study is to change the soot amount by using the barium additive and to investigate the effects of soot on NO formation. Also, the changes in soot and NO are studied by varying the engine load and speed conditions, which cause different combustion characteristics. Note that the additive is just used as a research tool, so the barium additive cannot be a solution to soot emissions.

In order to separate the possible effects of the barium additive on NO formation, B100 is used with the barium additive since the pure biodiesel produce less soot and weakens the soot effect on NO formation.

Using the biodiesel fuels, various engine loads and speeds are tested to understand the changes in NO concentration since biodiesel generally produce more NO than the conventional diesel. It is expected to show what factor is dominant on NO formation.

The experimental data is analyzed and processed into heat release rate, heat transfer rate, temperature, and mass fraction. Soot emissivity is also estimated based on the calculated results.

3 THEORY OF ZONAL ANALYTICAL MODELS

3.1 Single-Zone Model

A single-zone model, which is introduced by Krieger et al.[30], is based on the first law of thermodynamics, the conservation of mass law, and the ideal gas law. It is assumed that the contents in a combustion chamber are in an open control volume, and that the control volume is in a thermodynamic equilibrium at any instant in time; thus there are no temperature and pressure gradients, non-equilibrium chemical composition, and fuel vaporization. The analytical model begins with the first law of thermodynamics, which is expressed as:

$$\frac{d\left(m\cdot u\right)}{d\theta}=u\frac{dm}{d\theta}+m\frac{du}{d\theta}=-p\frac{dV}{d\theta}+\dot{Q}+\sum_{i}\dot{m}_{i}\cdot h_{i} \qquad 3.1$$

where $\frac{d\left(m\cdot u\right)}{d\theta}$ is the change of internal energy inside a cylinder.

$p\frac{dV}{d\theta}$ is the mechanical work done on the surface.

$\dot{Q}$ is the heat transfer rate from the control volume surface to cylinder gases.

$\sum_{i}\dot{m}_{i}\cdot h_{i}$ is the flow energy through the control volume surface.

$\dot{m}_{i}$ is mass flow rate into the system.

m is mass of burned fuel-air mixture.

u is internal energy.

p is instantaneous cylinder pressure.

V is instantaneous cylinder volume.

θ is crank angle degree.

h is enthalpy of fuel-air mixture.

The ideal gas law is also applied to the gases in a combustion chamber, which is written as:

$$p \cdot V = m \cdot R \cdot T$$

$$V \cdot \frac{dp}{d\theta} + p \cdot \frac{dV}{d\theta} = R \cdot T \cdot \frac{dm}{d\theta} + m \cdot T \cdot \frac{dR}{d\theta} + m \cdot R \cdot \frac{dT}{d\theta} \qquad 3.2$$

Since the composition of the gases continues to change in temperature and pressure, the ideal gas constant R is assumed to be a function of temperature T and pressure p (due to their effect on the species composition through dissociation) and equivalence ratio ϕ. Therefore, the differential of the ideal gas constant can be expressed as:

$$\frac{dR}{d\theta} = \frac{\partial R}{\partial T} \cdot \frac{dT}{d\theta} + \frac{\partial R}{\partial p} \cdot \frac{dp}{d\theta} + \frac{\partial R}{\partial \phi} \cdot \frac{d\phi}{d\theta} \qquad 3.3$$

Similarly, the internal energy is also assumed to be a function of temperature, pressure, and equivalence ratio. Thus, the differential form of the internal energy is expressed as following:

$$\frac{du}{d\theta} = \frac{\partial u}{\partial T} \cdot \frac{dT}{d\theta} + \frac{\partial u}{\partial P} \cdot \frac{dp}{d\theta} + \frac{\partial u}{\partial \phi} \cdot \frac{d\phi}{d\theta} \qquad 3.4$$

Regarding the equivalence ratio, the equivalence ratio at any instant in time is given as [29],[30]:

$$\phi = \phi_0 + \left(\frac{1 + FA_0}{FA_s} \right) \cdot \left(\frac{m}{m_0} - 1 \right) \qquad 3.5$$

where ϕ is the equivalence ratio.

ϕ_0 is the initial equivalence ratio.

m is the instantaneous mass in the control volume.

m_O is the initial mass in the control volume.

FA_O is the initial fuel/air ratio prior to fuel injection.

FA_S is the stoichiometric fuel/air ratio.

Using Equations 3.1 through 3.5, the energy balance equation is rearranged to calculate the change of mass, $\frac{dm}{d\theta}$, shown as Equation 3.6. It is the mass flow rate, at which the fuel is inducted into a combustion chamber and immediately burned [29]. Thus, the instant change of mass can be treated as the mass burning rate with the assumption. If the fuel instantaneously reacted to equilibrium products right after entering the combustion chamber [29], the change of mass would imply the influence of in-cylinder pressure on the combustion in an engine with knowing the properties of the gases and the heat transfer rate inside the cylinder during combustion. The method to calculate the properties of the gases is introduced in section 3.4. The product of the mass flow rate and the lower heating value of a fuel is an apparent heat release rate, which can be approximated, but not be determined exactly [1].

$$\frac{dm}{d\theta}=\frac{m\cdot\left[-\frac{RT}{V}\frac{dV}{d\theta}-\frac{T\frac{\partial u}{\partial T}\left\{1+\frac{m}{R}\frac{\partial R}{\partial\phi}\left[\frac{1+FA_0}{FA_s m_0}\right]\right\}}{\left[1+\frac{T}{R}\frac{\partial R}{\partial T}\right]}-\frac{\partial u}{\partial p}\frac{dp}{d\theta}\right]+\dot{Q}}{u-h_f-\frac{T\frac{\partial u}{\partial T}}{\left[1+\frac{T}{R}\frac{\partial R}{\partial T}\right]}\left\{1+\frac{m}{R}\frac{\partial R}{\partial\phi}\left[\frac{1+FA_0}{FA_s m_0}\right]\right\}+m\frac{\partial u}{\partial\phi}\left[\frac{1+FA_0}{FA_s m_0}\right]} \qquad 3.6$$

The partial derivatives of the internal energy, *u*, and the ideal gas constant, *R*, with respect to a temperature, pressure, and equivalence ratio are obtained from the chemical equilibrium program, which is developed by Olikara and Borman [38] and is introduced in Appendix A.

This approach is to solve the energy equation by using the ideal gas law and the first law of thermodynamics with additional assumptions and initial conditions as following [29], [30]:

1. The initial temperature, pressure and volume.
2. The experimental pressure and volume data of the cylinder.
3. The expressions for the internal energy, enthalpy, and ideal gas constant of the combustion products and the reactants.
4. A correlation equation for calculating heat transfer inside a combustion chamber.
5. An estimated value of the temperature of a combustion chamber wall.
6. The geometry of a combustion chamber.

3.2 Two-Stage Model

The two-stage model assumes that the contents in a cylinder are in four control volumes [31]: unburned and burned stoichiometric-zones, and unburned and burned lean-zones. This model assumes that the combustion takes place at two stages. At each stage, only three out of four zones are active. At the first stage, the fuel in the unburned stoichiometric-zone transfers to the burned stoichiometric-zone through the combustion process, while the mixture of a fuel and air in the unburned lean-zone acts like ideal gases without exchanging mass to other zones as illustrated in Figure 3.

At the second stage, combustion starts in the unburned lean-zone. The mass of the unburned lean-zone is transferred to the burned lean-zone as shown in Figure 4, while the burned gases in the burned stoichiometric-zone are assumed to act like ideal gases under the assumption of the equilibrium compositions.

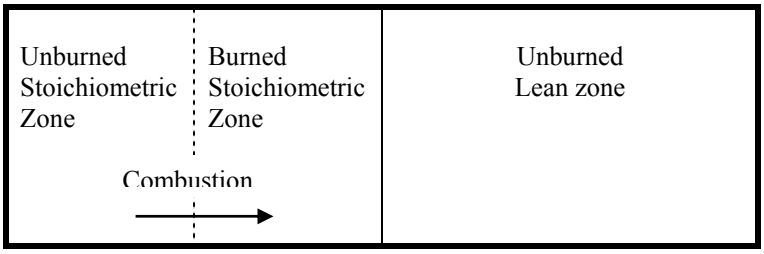

Figure 3 Conceptual figure at first stage of the two-stage model.

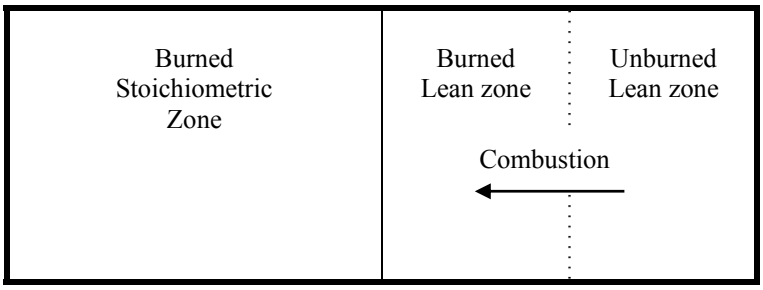

Figure 4 Conceptual figure at the second stage of the two-stage model.

The stoichiometric- and lean- zones are assumed to have, respectively, higher and lower equivalence ratios than the average value. The equivalence ratio of the stoichiometric-zone is decided regarding the auto-ignition and NO formation. The study by Morris et al. [39] shows that the auto-ignition occurs in the equivalence ratio ranging from 1 to 1.5. Additionally, the critical equivalence ratio for NO formation in high temperature and pressure burned gases is near stoichiometric [40]. It is critical period for NO formation when burned gas temperature is at maximum [1]. In the two-stage model, the maximum temperature and pressure are observed at the first stage in general. This is the reason why the equivalence ratio of the stoichiometric-zone is assumed to be at 1. The averaged equivalence ratio is determined experimentally based on the mass of the fuel-air mixture flow into the combustion chamber. The equivalence ratio of the lean-zone is initially calculated by using a correlation suggested by Szekely et al. [31].

$$\phi_l = 1.035 \cdot \phi_{\text{avg}} - 0.0917 \qquad 3.7$$

where ϕ_l is the equivalence ratio of the lean zone.
ϕ_{avg} is the averaged equivalence ratio.

However, the equivalence ratio of the lean-zone is adjusted based on the experimental NO results, since the above correlation is formulated by using two single-cylinder diesel engines: a 0.72 liter divided chamber engine and a 0.52 liter open chamber engine. Similar to the single-zone model, the thermodynamic properties are assumed to be a function of temperature, pressure, and equivalence ratio. Thus, the ideal

gas law can apply to this analytical model, and the ideal gas constant and internal energy of each zone can be expressed as:

$$\frac{dR_i}{d\theta} = \frac{\partial R_i}{\partial p} \cdot \frac{dp}{d\theta} + \frac{\partial R_i}{\partial T_i} \cdot \frac{dT_i}{d\theta} + \frac{\partial R_i}{\partial \phi_i} \cdot \frac{d\phi_i}{d\theta} \qquad 3.8$$

$$\frac{du_i}{d\theta} = \frac{\partial u_i}{\partial p} \cdot \frac{dp}{d\theta} + \frac{\partial u_i}{\partial T_i} \cdot \frac{dT_i}{d\theta} + \frac{\partial u_i}{\partial \phi_i} \cdot \frac{d\phi_i}{d\theta} \qquad 3.9$$

The subscript indicator, *i*, is designated to be *1* for the burned stoichiometric-zone, *2* for the unburned stoichiometric-zone, *3* for the burned lean-zone, and *4* for the unburned lean-zone.

The ideal gas law of each zone can be written as:

$$\frac{1}{p} \cdot \frac{dp}{d\theta} = \frac{1}{m_i} \cdot \frac{dm_i}{d\theta} + \frac{1}{R_i} \cdot \frac{dR_i}{d\theta} + \frac{1}{T_i} \cdot \frac{dT_i}{d\theta} - \frac{1}{V_i} \cdot \frac{dV_i}{d\theta} \qquad 3.10$$

The conservation of energy of each zone can be expressed similarly as:

$$\frac{d\left(m \cdot u\right)_i}{d\theta} = m_i \cdot \left(\frac{\partial u_i}{\partial p} \cdot \frac{dp}{d\theta} + \frac{\partial u_i}{\partial T_i} \cdot \frac{dT_i}{d\theta} \right) + u_i \cdot \frac{dm_i}{d\theta} = -p \cdot \frac{dV_i}{d\theta} + \frac{\delta Q_i}{d\theta} + h_i \cdot \frac{dm_i}{d\theta} \qquad 3.11$$

With arranging equations including the above ones, the fuel mass burning rate can be calculated. The more detailed derivations of equations are introduced in Appendix B.

The fuel mass burning rate of the stoichiometric zone can be simplified as:

$$\frac{dm_1}{d\theta}=\frac{\left\{\begin{array}{l}\frac{dT_2}{d\theta}\cdot\left[\frac{p\cdot V_2}{T_2}+\alpha_1\frac{m_1\cdot V_2}{V_1\cdot T_2}\frac{\partial u_1}{\partial T_1}\right]+\frac{dT_3}{d\theta}\left[\frac{p\cdot V_3}{T_3}+\alpha_1\frac{m_1\cdot V_3}{V_1\cdot T_3}\frac{\partial u_1}{\partial T_1}\right]-\frac{dV}{d\theta}\left[\frac{m_1\cdot\alpha_1}{V_1}\frac{\partial u_1}{\partial T_1}+p\right]\\ +\frac{dQ_1}{d\theta}-\frac{dp}{d\theta}\cdot\left[V_2+V_3+m_1\cdot\frac{\partial u_1}{\partial p}+m_1\cdot\alpha_1\frac{\partial u_1}{\partial T_1}\left(\frac{1}{p}-\frac{1}{R_1}\cdot\frac{\partial R_1}{\partial p}+\frac{V_2+V_3}{V_1\cdot p}\right)\right]\end{array}\right\}}{\left[u_1-u_2-\alpha_1\left(1-\frac{V_2\cdot m_1}{m_2\cdot V_1}\right)\frac{\partial u_1}{\partial T_1}\right]} \quad 3.12$$

The fuel mass burning rate of the lean-zone is arranged as:

$$\frac{dm_4}{d\theta}=\frac{\left\{\begin{array}{l}\frac{dT_1}{d\theta}\cdot\left[\left(p+\alpha_4\cdot\frac{m_4}{V_4}\cdot\frac{\partial u_4}{\partial T_4}\right)\cdot\left(\frac{V_1}{T_1}+\frac{V_1}{R_1}\cdot\frac{\partial R_1}{\partial p}\right)\right]+\frac{dT_3}{d\theta}\cdot\left[\frac{V_3}{T_3}\cdot\left(p+\alpha_4\frac{m_4}{V_4}\frac{\partial u_4}{\partial T_4}\right)\right]\\ -\frac{dV}{d\theta}\cdot\left(p+\alpha_4\frac{m_4}{V_4}\frac{\partial u_4}{\partial T_4}\right)\\ -\frac{dp}{d\theta}\cdot\left\{V_1+V_3+m_4\cdot\frac{\partial u_4}{\partial p}-\frac{pV_1}{R_1}\cdot\frac{\partial R_1}{\partial p}+\alpha_4\cdot m_4\cdot\frac{\partial u_4}{\partial T_4}\cdot\left(\frac{1}{p}-\frac{1}{R_4}\cdot\frac{\partial R_4}{\partial p}+\frac{V_1+V_3}{pV_4}-\frac{V_1}{V_4R_1}\cdot\frac{\partial R_1}{\partial p}\right)\right\}\\ +\frac{dQ_4}{d\theta}\end{array}\right\}}{\left[u_4-u_3-\alpha_4\cdot\left(1-\frac{V_3\cdot m_4}{V_4\cdot m_3}\right)\cdot\frac{\partial u_4}{\partial T_4}\right]} \quad 3.13$$

In the two-stage model, it is assumed that the combustion starts after the completion of injection to make the overall equivalence ratio constant, and that the combustion products at each zone do not mix with the other zone.

3.3 Heat Transfer

The heat transfer in a combustion chamber is classified into convection and radiation heat transfer. Due to the limit of the current experimental system, the

measurement of heat transfer inside cylinder cannot be carried out. Thus, well-known heat transfer correlations [41], [42] are employed to estimate the heat transfer and to understand its qualitative trend during combustion.

The correlation developed by Hohenberg [42] is used to calculate the total heat transfer that includes the convection and radiation heat transfers. Hohenberg treats the convection and radiation heat transfers as a lump. The total heat transfer coefficient is derived, empirically, based on the bore diameter, pressure, temperature, and gas velocity inside a cylinder. The correlation equation is expressed as:

$$h_c = C_1 \cdot V_c^{-0.066} \cdot p^{0.8} \cdot T^{-0.4} \cdot \left(\overline{v}_p + C_2\right)^{0.8}$$

where h_c is heat transfer coefficient [W/m^2·K]

p and T are pressure [kPa] and temperature [K] of the working fluid

V_c is cylinder volume [m^3]

$\overline{v}_p$ is mean piston speed [m/sec]

The constant C_1 is 130, and C_2 1.4.

After the total heat transfer is calculated, the soot emissivity is calculated independently. In general, the radiation in a diesel engine is divided into two parts: the luminous (soot) and non-luminous (gaseous) radiation. The radiation heat transfer rate at any crank angle is described as:

$$\frac{\delta Q_R}{d\theta} = \sigma \cdot \varepsilon \cdot A \cdot (T_R^4 - T_W^4)$$

where σ is Stefan-Boltzmann constant.

ε is total emissivity.

T_R is radiation temperature.

T_W is wall temperature of a cylinder.

A is surface area according to volume change of a combustion chamber.

Regarding the emissivity of combustion gas and soot particles, the non-luminous radiation is mainly due to the carbon dioxide and water vapor while the other gases of the combustion product gases such as H_2, O_2, and N_2 are relatively transparent to radiation and thus their radiation is negligible [1],[31]. However, the soot is more dominant compared to the non-luminous radiation during diesel combustions. Thus, the soot emissivity is calculated, which is the major factor to estimate the radiation heat flux, by using the correlation suggested by Morel et al. [43]:

$$\varepsilon_s = 1 - \exp\left(-1575 \cdot f_v \cdot T_R \cdot L\right)$$

where f_v is the soot volumetric fraction

T_R is the radiation temperature

L is the radiation path length.

The soot volumetric fraction is calculated as

$$f_v = \frac{m_s}{\rho_s \cdot V_b}$$

where m_s is the mass of soot

ρ_s is the density of soot.

$$L = 2.4 \cdot \frac{V_b}{A}$$

where V_b is the volume of the burned zone

A is its corresponding surface area.

The mass of soot is calculated as the method introduced by Morel et al. [43]. The soot formation in the burned zone is obtained by using the following equation:

$$\frac{dm_s}{dt} = A_1 \cdot \dot{m}_d \cdot \exp\left(\frac{-A_2}{T_b}\right) / \left(1 + 4.76 \cdot YO_2\right)$$

where $\dot{m}_d$ is the rate of burned fuel.

T_b is the temperature of the burned zone.

YO_2 is the mole fraction of O_2.

The constant A_1 is 0.30, and A_2 is 3000.

The soot oxidation rate is calculated by using the following equation:

$$\frac{dm_{so}}{dt} = -B_1 \cdot \frac{m_s}{\rho_s \cdot d_s} \cdot \exp\left(\frac{-B_2}{T_R}\right) \cdot PO_2^{1/2}$$

where ρ_s is soot density of 900 kg/m^3.

d_s is diameter of an elementary soot particle.

PO_2 is the partial pressure of oxygen in the burned zone.

The constant B_1 is 0.4, and B_2 is 10000.

The diameter of soot particles is assumed to be $d_s = 0.16 \cdot \phi_{avg}$.

Based on the study by Morel et al. [43], the radiation temperature is calculated to be 0.9 times the temperature of the burned gas until the burned gas temperature reaches its maximum value. After the burned gas temperature reaches the maximum, the radiation temperature is estimated as a function of the burned fraction, temperature, and maximum temperature of the burned gas. The suggested model is expressed as:

$T_R = 0.9 \cdot T_b$; Up to the maximum temperature

$T_R = 0.9 \cdot \left[r_b \cdot T_b + \left(1 - r_b\right) \cdot T_{b,\max} \right]$; After the maximum temperature

where subscript, *R*, means radiation

Subscript, *b*, means the burned zone

Subscript, *max*, means the maximum value

T is temperature

r_b is the burned fuel mass fraction

3.4 Chemical Reaction

Thermodynamic properties of the product gas mixture in a combustion chamber are assumed to be a function of temperature, pressure, and equivalence ratio. Through this approach, the properties of the product gas mixture, and their derivatives can be calculated. In this section, the basis of the chemical reactions is introduced and is based on the work by Olikara et al. [38].

In this approach, the combustion is assumed to take place with air and hydrocarbon fuel which contains C, H, O, and N atoms. It is assumed that the product species from combusting the air fuel mixture consist of 12 species: H, O, N, H_2, OH, CO, NO, O_2, H_2O, CO_2, N_2 and Ar in gas phase. This gas mixture is assumed to be in an equilibrium state at any instant in time. For example, the combustion with a fuel, $C_n H_m O_l N_k$, and air at an equivalence ratio takes place and the combustion product gases stay in an equilibrium state.

Olikara et al. [38] has developed a computational program to calculate the thermodynamic properties as the above equations are introduced. The computational program is introduced in Appendix A in detail. By using the computation program, the mole fraction of each product of 12 species can be calculated and is used to estimate the thermodynamic properties and the derivative of them in terms of a pressure, temperature, and equivalence ratio.

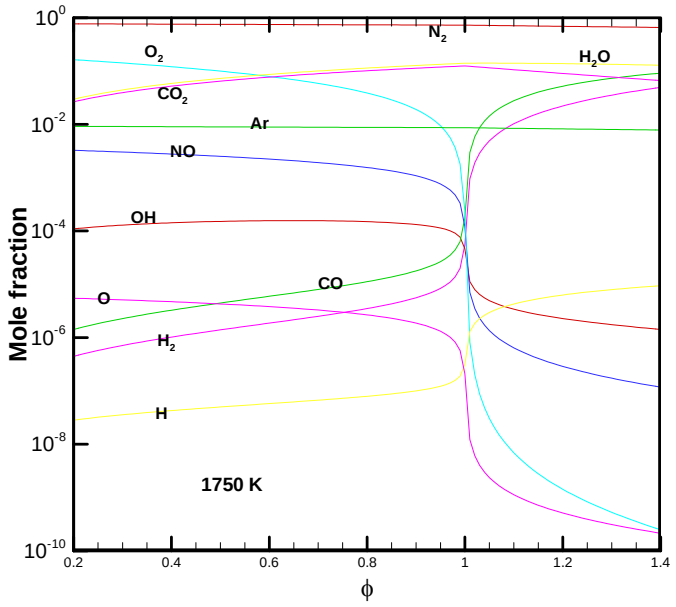

(a)

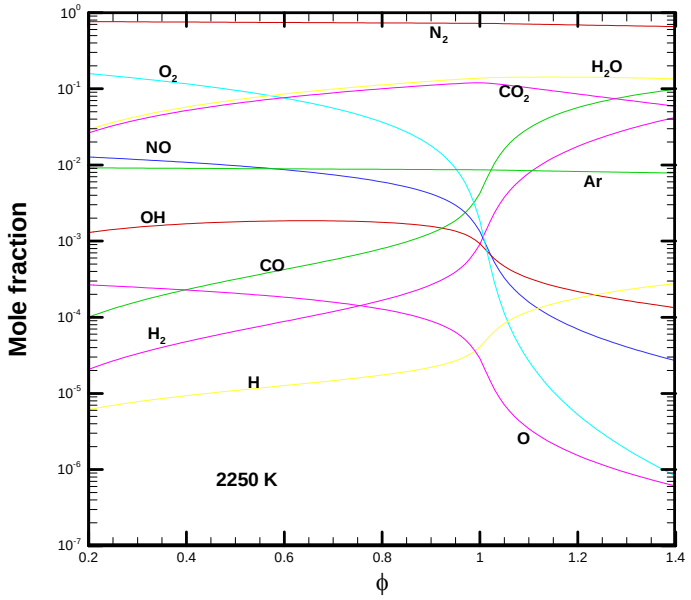

(b)

Figure 5 Mole fraction of equilibrium combustion products of isooctane-air mixtures as a function of equivalence ratio at 30 atmosphere and (a) 1750K; (b) 2250 K and (c) 2750 K [1].

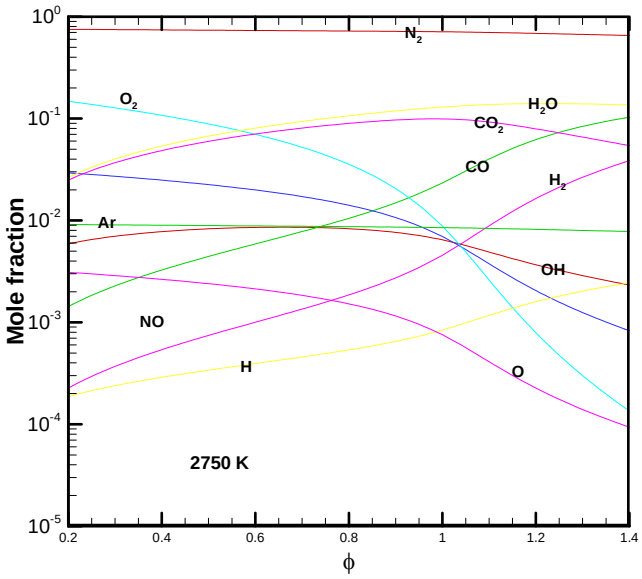

(c)

Figure 5. Continued.

For the thermodynamic properties and equilibrium composition, the computational program developed by Olikara and Borman [38] is adopted as a subroutine of the analytical model. To validate the program, the mole fractions of combustion products of isooctane-air mixtures are calculated and compared with the work by Heywood [1]. Figure 5 shows the mole fractions as a function of fuel/air equivalence ratio at 30 atmospheres and three different temperatures. The general trend of equilibrium mole fractions is the same as the reference [1].

The subroutine program for the thermodynamic properties is validated with the internal energy as a function of temperature and pressure. Figure 6 (a) shows the internal energy versus temperature for the unburned and burned gas mixtures of isooctane-air mixture. The circle symbols show the values from graphs by Heywood [1]. The figure

shows that the internal energy increases with pressure above 2000 K. Figure 6 (b) shows the internal energy of the unburned mixture with equivalence ratio. It shows that the internal energy of burned mixture of isooctane is increased with equivalence ratio as shown in [1]. From those validations, it is concluded that the two-stage model is reasonable enough to calculate the equilibrium mole fractions and thermodynamic properties.

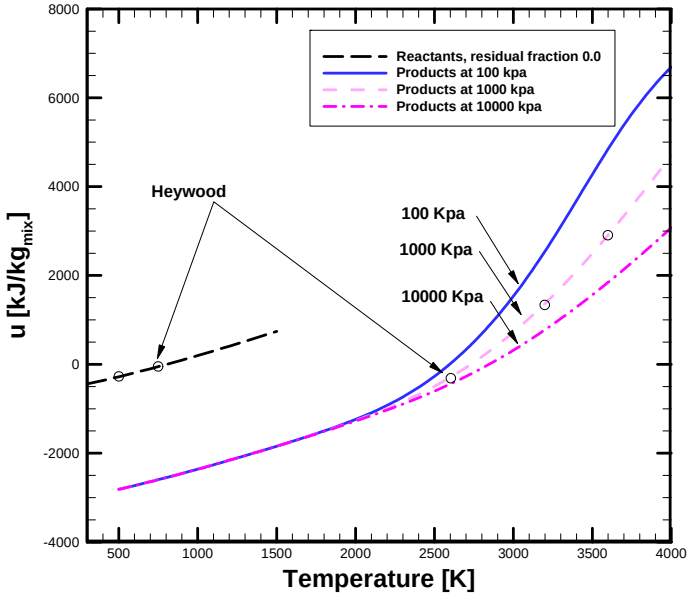

(a)

Figure 6 Thermodynamic properties calculated by the subroutines of the two-stage model: (a) Internal energy of unburned and burned mixtures; (b) Internal energy of unburned gases at various equivalence ratios.

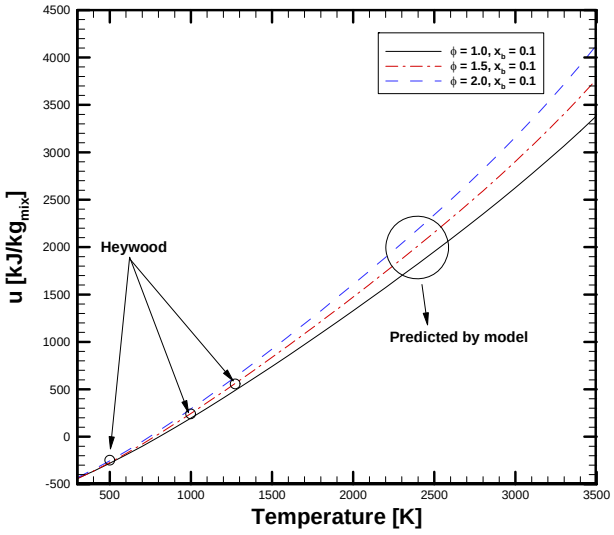

(b)

Figure 6 Continued.

3.5 NO Formation

In order to calculate NO concentration, the extended Zeldovich mechanism is used:

$$O + N_2 \leftrightarrow NO + N \qquad 3.14$$

$$N + O_2 \leftrightarrow NO + O \qquad 3.15$$

$$N + OH \leftrightarrow NO + H \qquad 3.16$$

It has an assumption that the reaction rates in a flame are so fast that the burned gases are almost in thermodynamic equilibrium. Thus, O, O_2, H, OH, and N_2 are calculated with the equilibrium assumption and then the NO formation rate is calculated

by their concentrations. Kinetic rate constants for NO formation mechanism are given by Dean et al. [44] as shown in Table 4.

Table 4 Reaction rate expression for nitrogen.

Reaction	Rate constant $\left[cm^3 / mol \cdot \sec\right]$
$O + N_2 \rightarrow NO + N$	$1.95\times10^{14} \cdot \exp(-38660/T)$
$N + O_2 \rightarrow NO + O$	$9.0\times10^{9} \cdot T \cdot \exp(-3270/T)$
$N + OH \rightarrow NO + H$	$1.1\times10^{14} \cdot \exp(-565/T)$

The calculation for NO concentration is compared with the study by Caton [14]. For the validation and caparison with work by Caton [14], a gasoline surrogate (C_7H_{17}) is used as a fuel, and both the pressure and the equivalence ratio are assumed as constants of 1000 kPa and 1.0, respectively. As the results are shown in Figure 7, the calculated NO reaches its equilibrium value gradually. For the case of 2600 K, it takes 0.004 seconds to reach the equilibrium value. For the case of 2500 K, it is about 0.013 seconds. For the lowest temperature of 2400 K, the actual NO amount increases slowly compared to the other cases, and it takes 0.053 seconds. It shows that the decrease of temperature causes the concentration of NO to be kinetically limited. Below a certain temperature, NO concentration becomes “frozen” regardless of what the associated equilibrium concentration should be at the lower temperature [14].

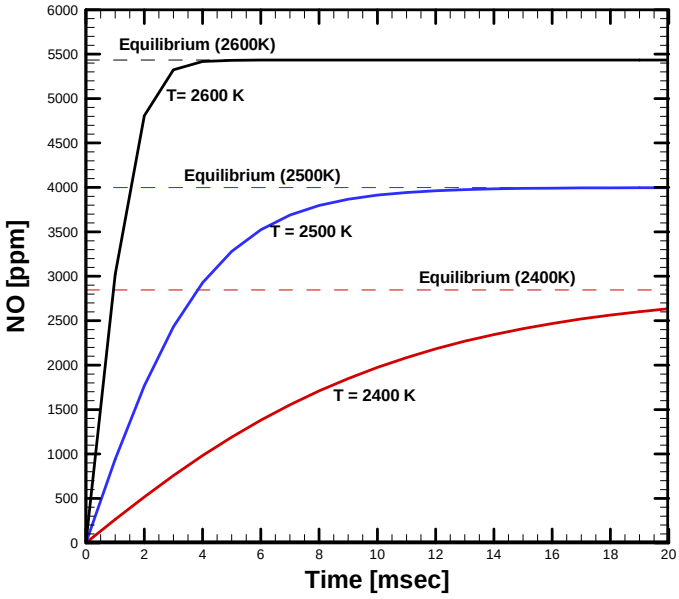

Figure 7 Nitric oxide concentration as a function of time and three equilibrium temperatures at 1000 kPa and an equivalence ratio of 1.0.

3.6 Data Processing

One of the main inputs in the heat release analysis is the in-cylinder pressure data versus crank angle data. Rapidly running engines may generate high-frequency waves [45], which are the local pressure deviations from average pressure. Some of the waves can be introduced by the instrumentation as “noise”; however most of them are generated by combustion process [30]. Thus, the measured pressure data generally includes high frequency waves.

The zero-dimensional analytical models assume that the pressure inside a cylinder is uniform while ignoring any pressure gradients that may actually exist during combustion. Additionally, high amounts of “noise” in the pressure data results in nearly

incomprehensible and unusable heat release data. Thus, it is desirable that the noisy data be removed. Several studies emphasize the importance of filtering pressure data to remove the waves, because small oscillation in pressure data causes wild oscillation in the heat release calculation [29],[30],[46]. Usually, pressure data is averaged over many cycles, and then is smoothed to obtain a well behaved pressure data [29]. There are two general methods to smooth pressure data: a spline smoothing method and a low pass filtering method. A spline smoothing method is to interpolate pressure data and remove the ripples in the pressure data; while a low pass filtering removes ripples above a cutoff frequency because the ripples are generated by high frequency acoustic pressures.

Theoblad et al. [45] shows that the spline is not effective in removing ripples, because the method changes heat release rate due to a large reduction in the value of peak pressure. On the other hand, the low pass filter is shown to be effective in smoothing pressure data. However, the low pass filtering method decreases the peak value of the heat release rate in premixed combustion phase with decreasing the cutoff frequency. Thus, a proper cutoff frequency might be the one that does not decrease the peak value of the heat release rate of premixed combustion.

In this study, the low pass filtering method is selected over the spline smoothing method. A subroutine program of the Compaq Extended Math Library (CXML), sfilter_nonrec, is used, which provides the low pass filtering. In order to find a proper cutoff frequency, a set of pressure data is used, which is measured at an engine speed of 1400 rev/min and a torque of 250 ft-lbs with petroleum diesel fuel. The pressure data is the average of about 300 cycles at a high load condition. By using the pressure data, the

mass burning rates are calculated and, then, used to judge the cutoff frequency of the low pass filtering. Figure 8 shows the mass burning rate according to cutoff frequency, which is normalized value. The mass burning rate calculated from the cycle-averaged and unfiltered pressure data shows ripples. The result with the cutoff frequency of 0.05 shows the smoothed mass burning rate without ripples. However, the peak value of the premixed combustion is decreased as mentioned in the study [45]. It is observed that the peak value of the premixed combustion is increased with the cutoff frequency, while the peak value of the mixing-controlled combustion is not affected. However, the ripples start appearing above a certain cutoff frequency, which is 0.15 in this study. Therefore, the cutoff frequency needs to be selected in the range between 0.1 and 0.15. The frequency range might help to avoid a big reduction of the peak value in the premixed combustion phase, and to remove ripples in the rate of burning mass.

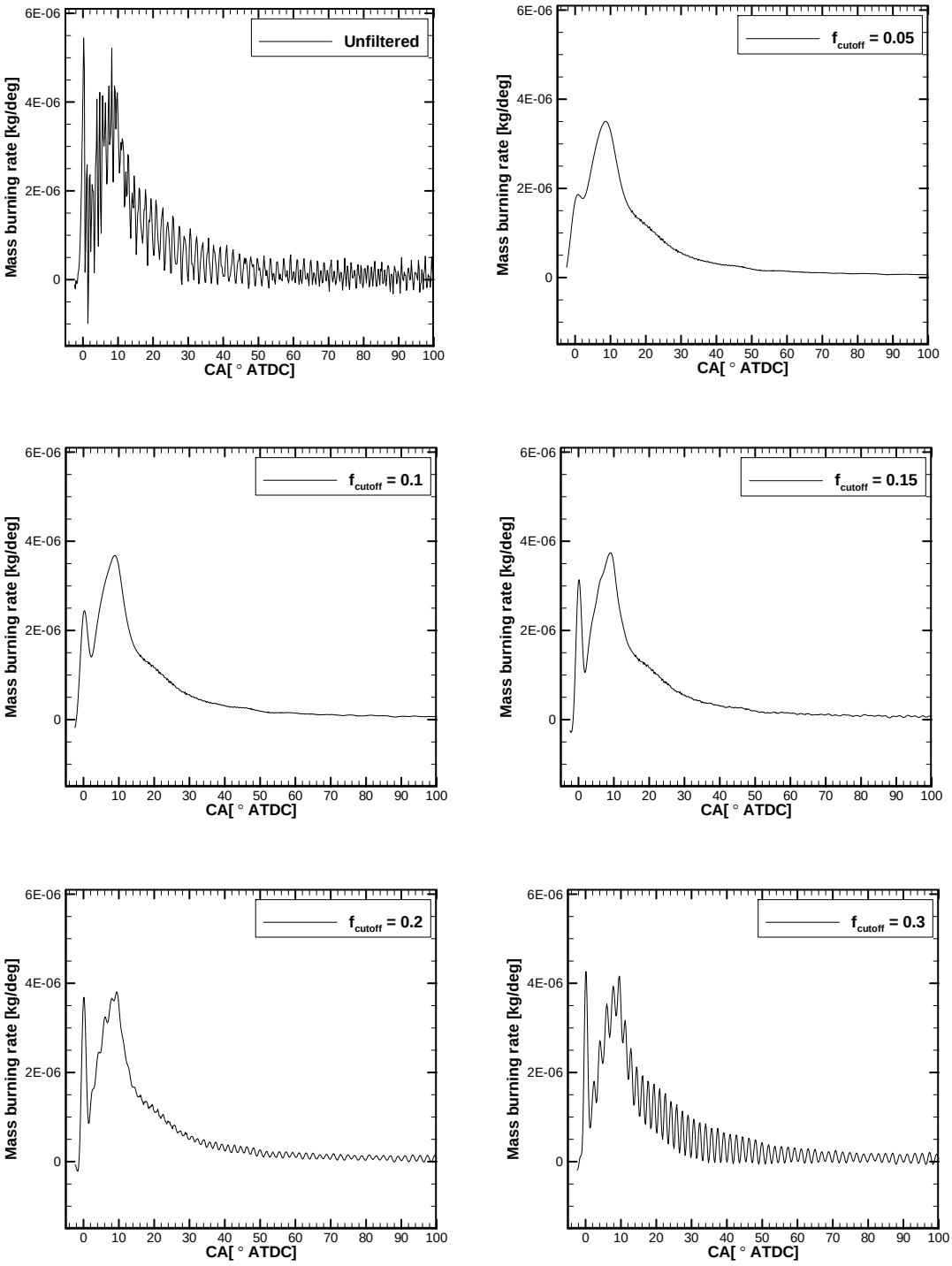

Figure 8 Mass burning rate from original and filtered pressure data.

4 RESULTS AND DISCUSSION OF #2 DIESEL TESTS

#2D tests are carried out and analyzed by using the single-zone and, mainly, the two-stage model: four fuel cases at each engine operating condition with varying amounts of the barium additive by volume basis: 0, 0.1, 0.25 and 0.5%-v. In this section, the results from the experimental data and the analytical models are introduced.

4.1 Maximum Brake Torque

The first test is to find the maximum brake-torque (MBT) by sweeping the fuel injection timing. The engine loads are set at 50 and 250 ft-lbs with the engine speed of 1400 rev/min. The other condition is at 150 ft-lbs and 2400 rev/min.

As shown in Figure 9(a), the MBT for a given mass of fuel and air, which can give the torque about 50 ft-lbs at 1400 rev/min, is found when fuel is injected at around -10° after top dead center (ATDC). The torque increases, reaches the peak value, and decreases with varying the injection timing. Regarding the scale of y-axis, the difference of torque is not significant near -10° ATDC as shown in Figure 9(a) since the fuel flow is kept almost constant. Thus, the start of injection (SOI) at 50 ft-lbs and 1400 rev/min is defined to be -10°.

Similarly, the MBT at 1400 rev/min and 250 ft-lbs is found when the fuel injection is started at -15° ATDC as shown in Figure 9 (b). The SOI for the case of 2400 rev/min and 150 ft-lbs is found to be -20° ATDC as shown in Figure 9(c). Both cases clearly show the maximum torque values. The found SOI is summarized in Table 5.

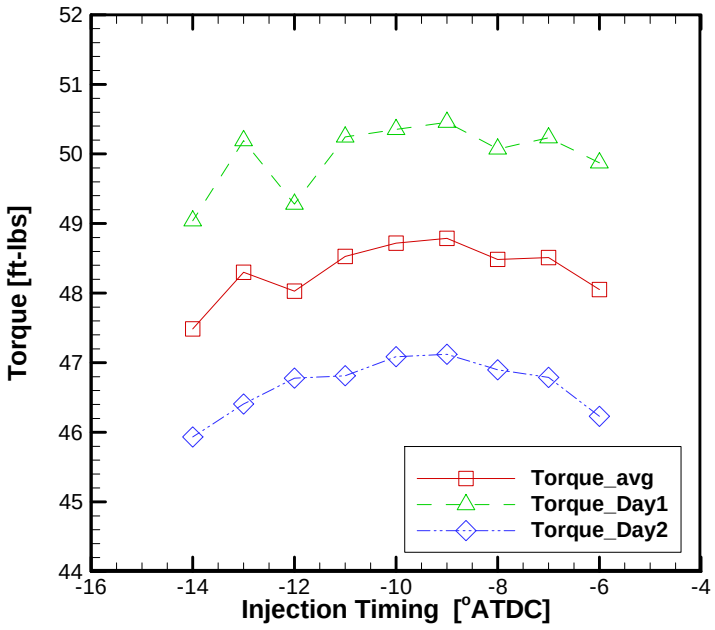

(a)

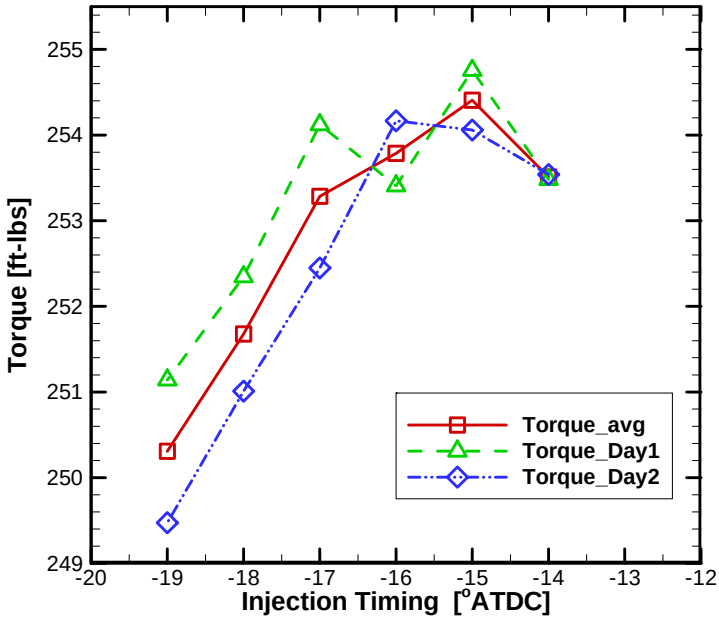

(b)

Figure 9 MBT at the engine running conditions with #2D: (a) 1400 rev/min and 50 ft-lbs, (b) 1400 rev/min and 250 ft-lbs, and (c) 2400 rev/min and 150 ft-lbs.

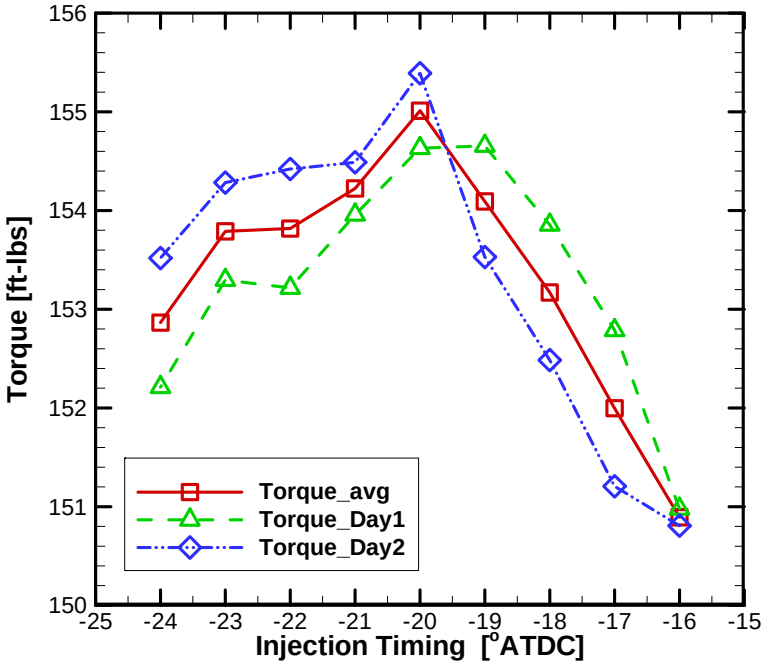

(c)

Figure 9 Continued.

Table 5 Start of injection timing for each test condition.

Test condition	SOI (° ATDC)
1400 rev/min and 50 ft-lbs	-10
1400 rev/min and 250 ft-lbs	-15
2400 rev/min and 150 ft-lbs	-20

4.2 Start of Combustion

Regarding the two-stage model, the start of combustion (SOC) needs to be defined since the two-stage model is triggered at SOC point, which is based on the heat

release rate result from the single-zone model. In general, the single-zone model shows that the heat release rate changes from negative to positive followed by fast increase near TDC [29]. The crank angle position for the zero heat release is defined as SOC.

Figure 10 shows an example at 1400 rev/min and 50 ft-lbs. The figure shows the negative rate, which can be interpreted as the temperature and pressure decrease due to the fuel evaporation before the SOC [1]. Figure 11 and Figure 12 show the heat release rate at 250 ft-lbs and 1400 rev/min, and 150 ft-lbs and 2400 rev/min, respectively. Similarly, the figures show the negative heat release before the dramatic increase.

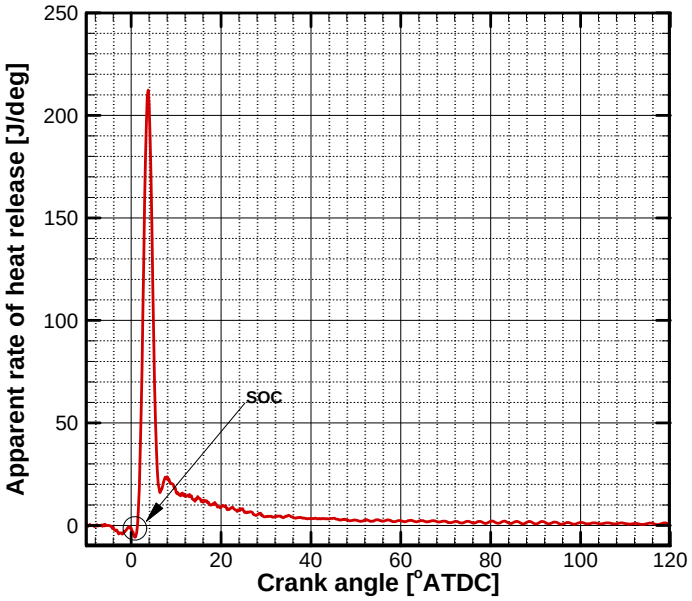

Figure 10 Rate of heat release with #2D at 1400 rev/min and 50 ft-lbs by using the single-zone model.

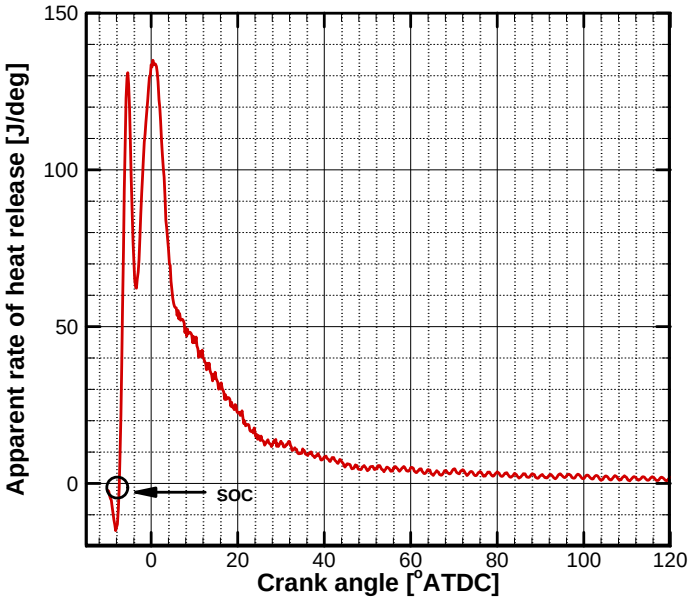

Figure 11 Rate of heat release with #2D at 1400 rev/min and 250 ft-lbs by using the single-zone model.

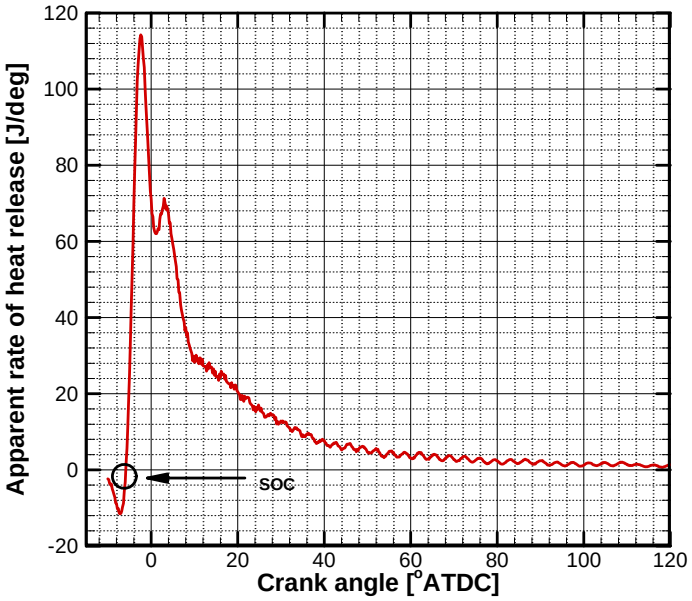

Figure 12 Rate of heat release with #2D at 2400 rev/min and 150 ft-lbs by using the single-zone model.

Table 6 shows the SOC of two different days under the identical fuel conditions, injection timing and engine operating condition. Each case has same or slightly different SOC for different days. Looking at the intake air temperature, generally higher intake air temperature causes earlier combustion except for several outliers as shown in Figure 13. In other words, if the ambient air temperature is higher, the SOC takes place earlier. Regarding the crank angle resolution of 0.2 °, the difference of SOC timing between two days is negligible. The fuels mixed with the barium additive are also tested, but there is no noticeable advance or retard of combustion caused by the barium additive as shown in Table 6. At the defined SOC timing, the adiabatic flame temperature is calculated for the two-stage model to take as an initial temperature, and the following calculations are carried out with the thermodynamics and simplified chemical reactions. In addition to the starting point of the two-stage model, its ending point is defined at the exhaust valve opening, which occurs at around 115 °ATDC. Thus, all the results from the two-stage model are calculated from the SOC to about 115 °ATDC in the following sections.

Table 6 Start of combustion and ignition delay.

Engine condition	Barium (%)	SOC (°ATDC)		ID (°)	
		Day 1	Day 2	Day 1	Day 2
1400 rev/min & 50ft-lbs	0.0%	1.4	1.2	11.4	11.2
	0.1%	0.8	1.0	10.8	11.0
	0.25%	1.2	1.2	11.2	11.2
	0.5%	1.2	1.0	11.2	11.0
1400 rev/min & 250ft-lbs	0.0%	-7.2	-7.8	7.8	7.2
	0.1%	-7.6	-7.8	7.4	7.2
	0.25%	-7.4	-7.6	7.6	7.4
	0.5%	-7.4	-7.6	7.6	7.4
2400 rev/min & 150ft-lbs	0.0%	-5.8	-6.2	14.2	13.8
	0.1%	-6.2	-6.4	13.8	13.6
	0.25%	-6.0	-6.0	14.0	14.0
	0.5%	-6.2	-6.2	13.8	13.8

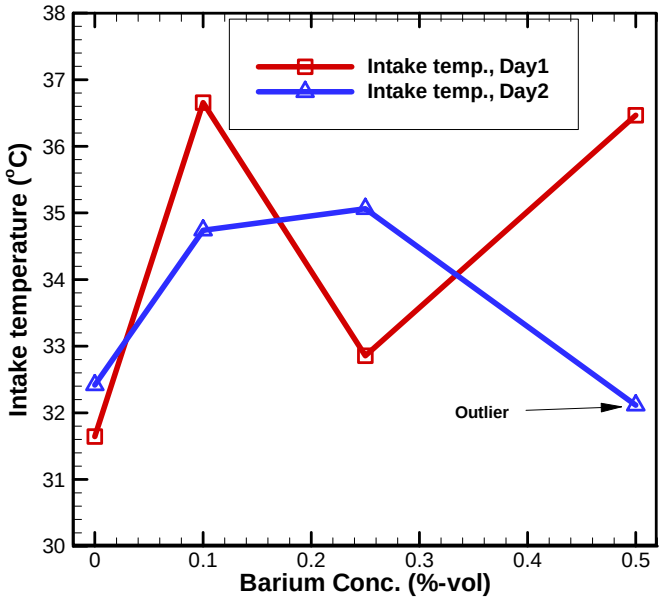

(a)

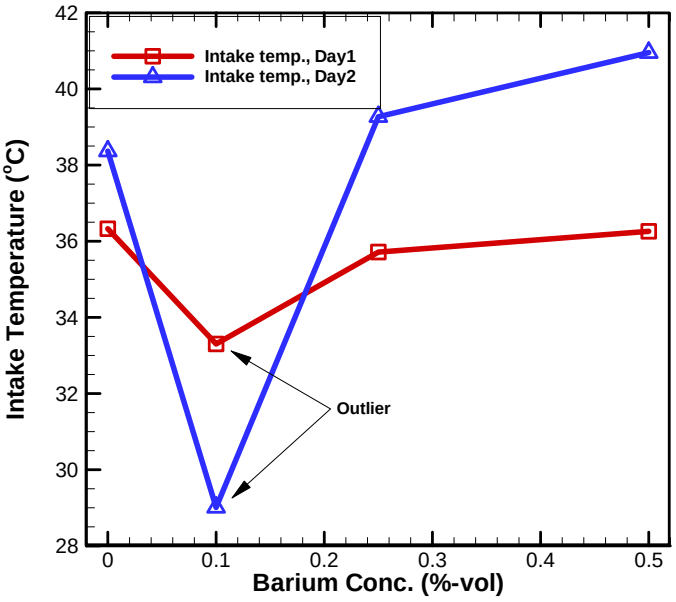

(b)

Figure 13 Daily change of intake temperature with #2D: (a) 1400 rev/min and 50 ft-lbs, (b) 1400 rev/min and 250 ft-lbs and (c) 2400 rev/min and 150 ft-lbs.

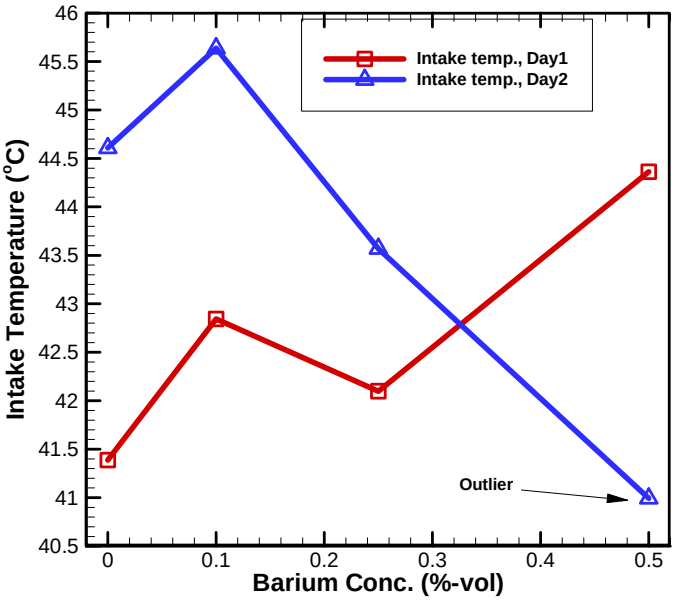

(c)

Figure 13 Continued.

4.3 Apparent Rate of Heat Release

With the definition of SOC based on the single-zone model, the apparent rates of heat release, which are named as heat release rate in the current study, are calculated by using the two-stage model.

As the results at 1400 rev/min and 50 ft-lbs are shown in Figure 14, the SOC is observed at 0.8 to 1.4 ° ATDC. It means that the ignition is delayed to about 10.8 to 11.4 ° after SOI. There are some changes in ignition delay (ID), but there is no clear tendency caused by the barium additive, also, as shown in Table 6. It seems that the amount of the additive does not cause the ignition to advance or retard.

As shown in Figure 14, the heat release rate increases dramatically after the start of combustion and decreases after reaching the peak rate. High heat release rate is observed slightly ATDC, likely due to the dominant premixed combustion phase. It is difficult to observe the diffusion combustion phase, which is a typical observation for light load conditions.

In this case, 90 % mass is burned by about 30 ° ATDC, and remaining 10% mass requires about another 85°. For engine purposes, the 90% mass fraction burn duration is of interest, which requires about 30° for this condition.

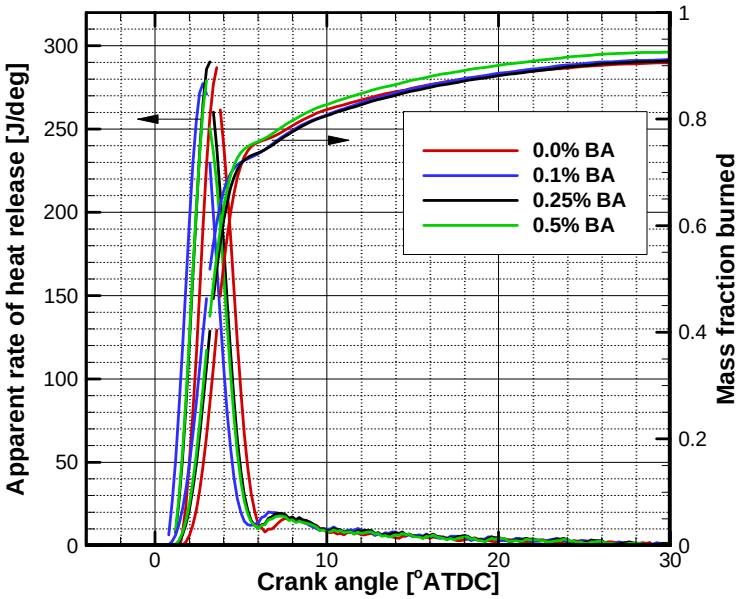

Figure 14 Comparison of the rate of heat release and mass fraction burned at 1400 rev/min and 50 ft-lbs with #2D.

Similarly, the heat release rate for the case at 1400 rev/min and 250 ft-lbs is illustrated in Figure 15. The injection timing of this case is set at -15° ATDC, and the SOC is calculated to be -7.8° to -7.2° ATDC. Again, the SOC is not definitively affected by the addition of the barium additive. The ignition delay is about 7.2° to 7.8° and is shorter than that of the previous case at 1400 rev/min and 50 ft-lbs. Lyn [47] describes that the increased ignition delay leads to higher maximum rate of heat release; based on this, it seems that the peak heat release rate for 50 ft-lbs is higher than for 250 ft-lbs since the lower load case has longer ignition delay.

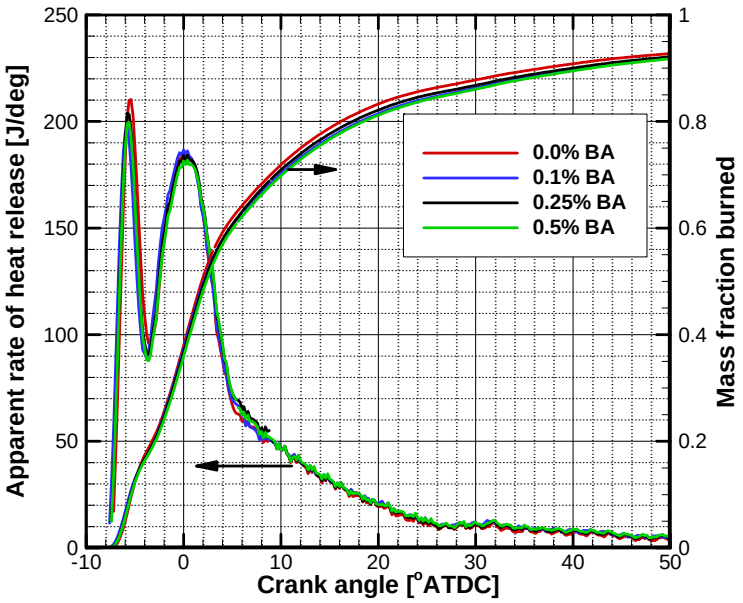

Figure 15 Comparison of the rate of heat release and mass fraction burned at 1400 rev/min and 250 ft-lbs with #2D.

In order for the engine to achieve the higher load, the intake manifold pressure is set at 1.2 bar as shown in Table 7, while the lower load case has about the ambient

pressure (about 1bar). It means that the cylinder entrains more air, and that there is more air to mix with fuel during the ignition delay. Also, the higher intake manifold pressure may cause the in-cylinder pressure to increase, the in-cylinder temperature to reach the fuel's combustible temperature earlier, and the ignition to advance, compared to the lower engine load case. As shown in Table 7, higher load case generally has higher intake air temperatures, which can advance the ignition. Thus, it may explain the shorter ignition delay for the higher load.

In terms of injection pressure, the higher load case has higher injection pressure of 900 bar while the lower load case has the injection pressure of 816 bar. Higher injection pressure helps the air and fuel mix to the ignitable limit. Thus, it can also advance the ignition.

However, it is difficult to compare the effect of injection timing on ignition delay since each SOI timing is defined based on the MBT tests. The higher load case has the advanced injection timing (15 ° BTDC) compared to the lower load case (10 ° BTDC).

Table 7 Intake manifold pressure and temperature

	Intake Manifold Pressure (bar)				Intake temperature (^{o}C)			
	0 %BA	0.1 %BA	0.25 %BA	0.5 %BA	0 %BA	0.1 %BA	0.25 %BA	0.5 %BA
50 ft-lbs	0.96	0.96	0.96	0.96	36.6	41.4	38.1	41.1
250 ft-lbs	1.20	1.20	1.20	1.20	43.7	39.5	44.9	46.0

Unlike the low load case, two combustion phases are observed at 1400 rev/min and 250 ft-lbs. The heat release rate is increased with SOC, and then decreased. This

phase of combustion is supposed to be the premixed combustion. After the premixed combustion phase, the diffusion mode is observed, which is controlled by the fuel-air mixing process [1], [48]. 90 % mass is burned by about 50 ° ATDC. While most of thermal energy is released during the premixed combustion phase at the lower load case, the majority of heat release is observed during the mixing-controlled phase at the higher load case. This difference is mainly caused by the amount of injected fuel. At the same speed, high load case needs more fuel to produce more torque.

For the case at 2400 rev/min and 150 ft-lbs, Figure 16 shows the similar heat release rate trend as at 1400 rev/min and 250 ft-lbs case. The SOC is observed to be -6.2° to -5.8° ATDC. Considering the SOI timing at -20° ATDC, the ignition delay is about 14 °. The 90 % fuel is burned by 40° ATDC. In this case, the stronger air motion lets more fuel-air mix to a combustible condition, so the premixed combustion phase occupies more portion of combustion duration in crank angle basis, and the width of the premixed combustion phase is a little bit wider compared to the case of 1400 rev/min and 250 ft-lbs. The figure also shows a smaller peak of the diffusion combustion phase mainly due to longer available time for premixed combustion than the previous case. Thus, the portion of the diffusion combustion phase is decreased. As shown in Figure 16, adding the barium additive causes little difference in the heat release rate.

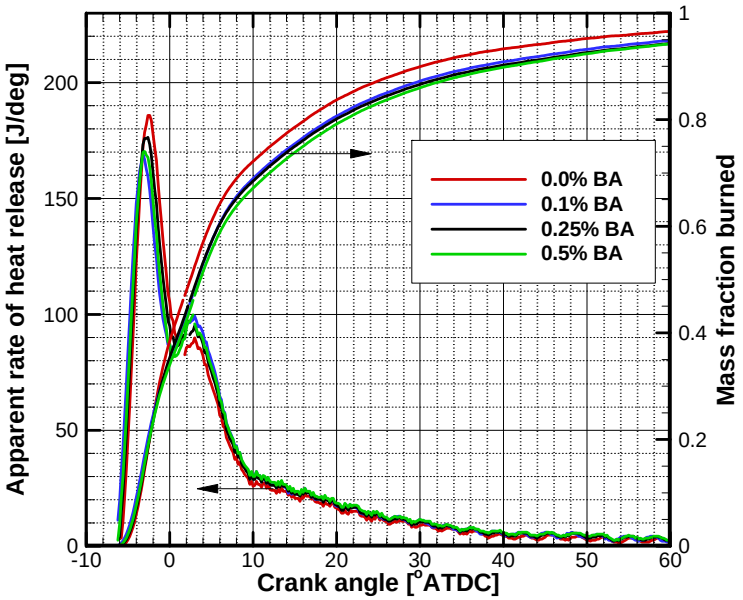

Figure 16 Comparison of the rate of heat release and mass fraction burned at 2400 rev/min and 150 ft-lbs with #2D.

4.4 Temperature Change

One of the improvements by using the two-stage model is to have more realistic temperature results compared to the single-zone model. This improvement enables the modeling of NO formation, which is highly dependent on temperature. The following results show the temperatures calculated from the two-stage model. As mentioned above, the low temperature calculated from the single-zone is an obstacle to modeling NO formation, because thermal mechanism of NO formation is not significant below 1800 K [15].

Figure 17 shows that the stoichiometric-zone temperature is much higher than that of single-zone model at the engine condition of 50 ft-lbs and 1400 rev/min with # 2

diesel fuel, while the temperature of the lean-zone is close to that of single-zone model and below 1800 K. Thus, the two-stage model makes it possible to model the NO formation with overcoming the lower temperature results of the single-zone model.

Figure 18 shows the temperature results for 1400 rev/min and 250 ft-lbs case. The results also show the comparison between the results of the two-stage model and the single-zone model. Temperatures of both the stoichiometric- and lean-zone are higher than that of the single-zone model as shown in the figure. According to the rate of heat release, most of the heat is released at the second stage, which corresponds to the lean-zone burning, thus the results show that the lean-zone has higher temperature than the single-zone model.

Figure 19 shows the calculated temperatures for the case of 2400 rev/min and 150 ft-lbs. Like the previous case, the temperature for the lean zone is higher than the criteria temperature of 1800 K, partially. Thus, the effect of the lean zone on NO concentration is not negligible. In the following section, the calculated NO concentration from the two-stage model is introduced and compared to the experimentally measured NO.

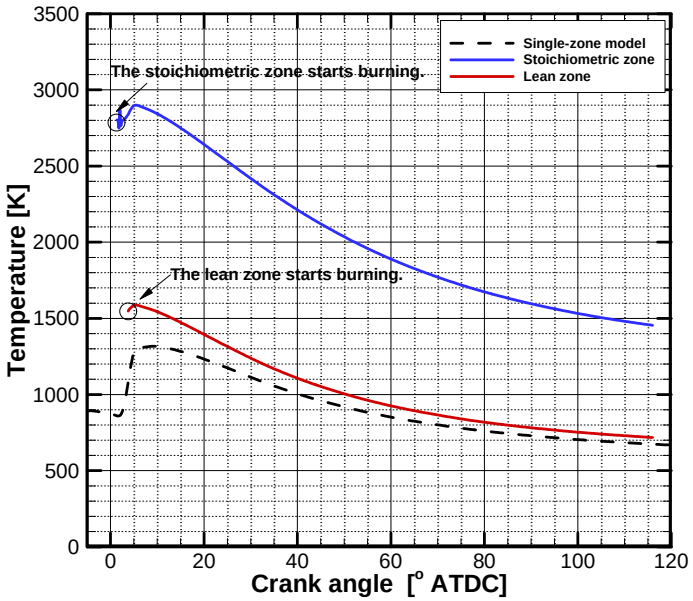

Figure 17 Gas temperatures calculated with the single-zone and the two-stage models for 1400 rev/min and 50 ft-lbs with #2D.

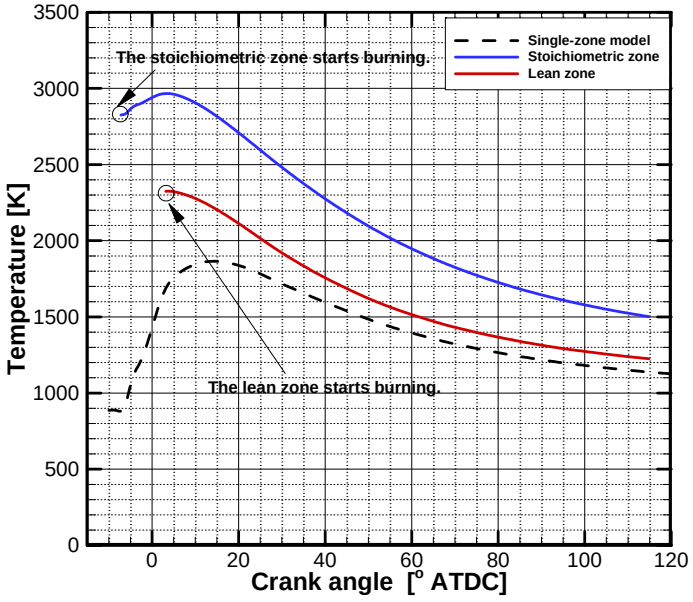

Figure 18 Gas temperatures calculated with the single-zone and the two-stage models for 1400 rev/min and 250 ft-lbs with #2D.

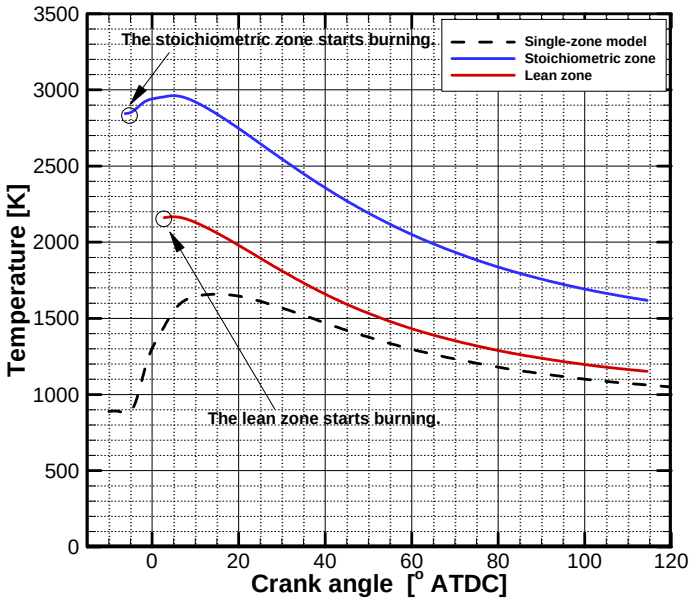

Figure 19 Gas temperatures calculated with the single-zone and the two-stage models for 2400 rev/min and 150 ft-lbs with #2D.

4.5 NO Concentration

In this section, the calculated NO concentrations from the two-stage model are introduced and are compared with the experimental measurements. Each figure shows the calculated values and measured ones. The calculation results at the same engine conditions show the similar trend regardless of the barium additive concentration, so one for each engine condition is presented. Before introducing the calculation results, it should be noticed that

1) The emission analyzer is only detecting NO.

2) The two-stage model does not capture NO_2 formation.

3) The data for this study are for only one cylinder out of 4 cylinders, whereas the measured NO concentration is an engine average.
4) A perfect match is unrealistic even though the final NO value from the calculation is close to the experimentally measured NO concentration.

NO concentrations at 50 ft-lbs are shown in Figure 20. The figure shows the results of computed NO concentrations, temperatures of each zone, and the mass averaged NO concentration. The mass averaged NO is mainly affected by the stoichiometric-zone because the NO concentration in the lean-zone is too small to be shown due to the low temperature below 1800 K. The calculated NO concentration is 486 ppm, while the measured one is 488 ppm. This result, again, shows the importance of temperature in the thermal mechanism of NO formation. Roughly, the temperature of the lean zone ranges close to that of the single zone model as shown in Figure 17, and the NO concentration is too small to be shown in Figure 20(a). Thus, it is difficult to model the NO formation by using the single-zone model.

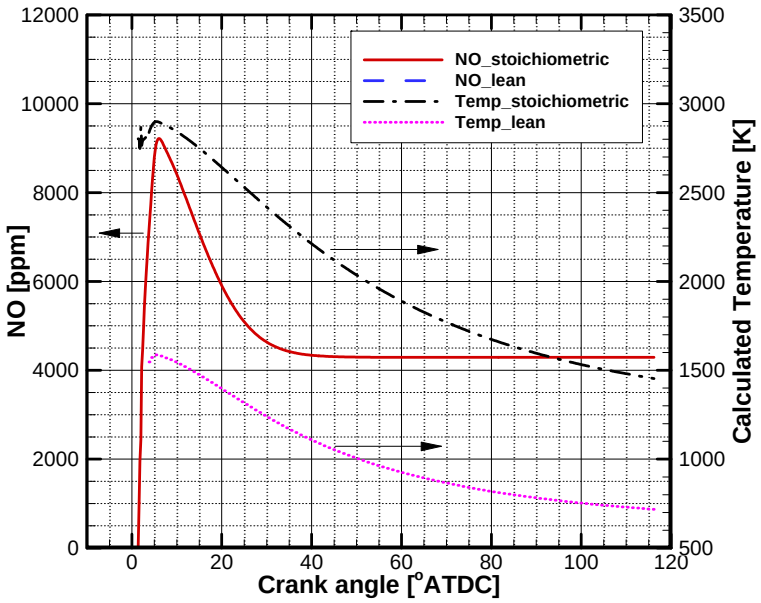

(a)

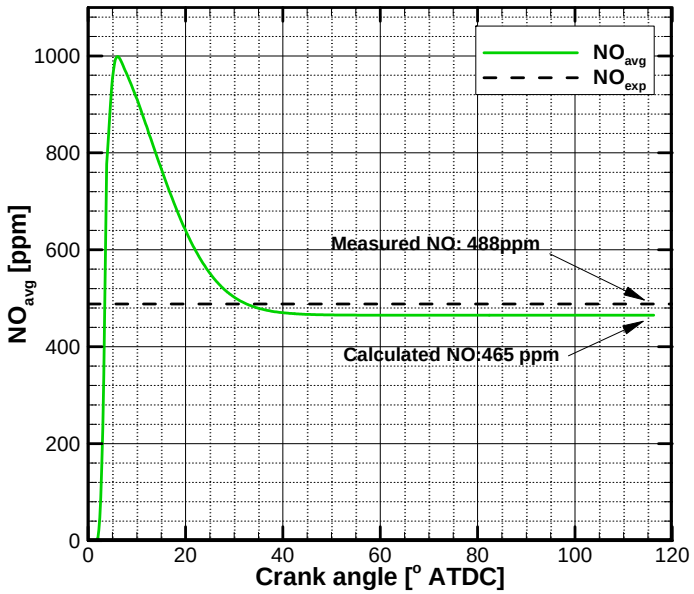

(b)

Figure 20 NO concentration with #2D at 1400 rev/min and 50 ft-lbs: (a) Zonal NO and temperatures, (b) Averaged NO concentration.

In the case at 1400 rev/min and 250 ft-lbs, the temperature in the lean zone ranges partially over 1800 K. The computed NO concentration in the lean zone is no longer negligible, and the mass averaged NO concentration is not only affected by the stoichiometric zone, but also by the lean zone. The NO concentration is mainly affected by the stoichiometric zone by 40° ATDC when the NO concentration in the stoichiometric zone freezes as shown in Figure 21(a). After this crank angle position, the averaged NO concentration is dominated by the lean zone and increases gradually with increasing mass burned in the lean zone.

For the last case at 2400 rev/min and 150 ft-lbs, Figure 22(a) and (b) show that the NO concentration is dominated by the stoichiometric zone, even though the lean zone produces some thermal NO. Considering the temperature of the lean zone, it is partially above the temperature limit of 1800 K, and causes the NO to form. The heat release rate shows the dominant combustion process in the premixed phase, but shows the small peak in the diffusion phase. So it is possible that at this operating condition, the second phase of combustion does not last long enough to produce substantial thermal NO.

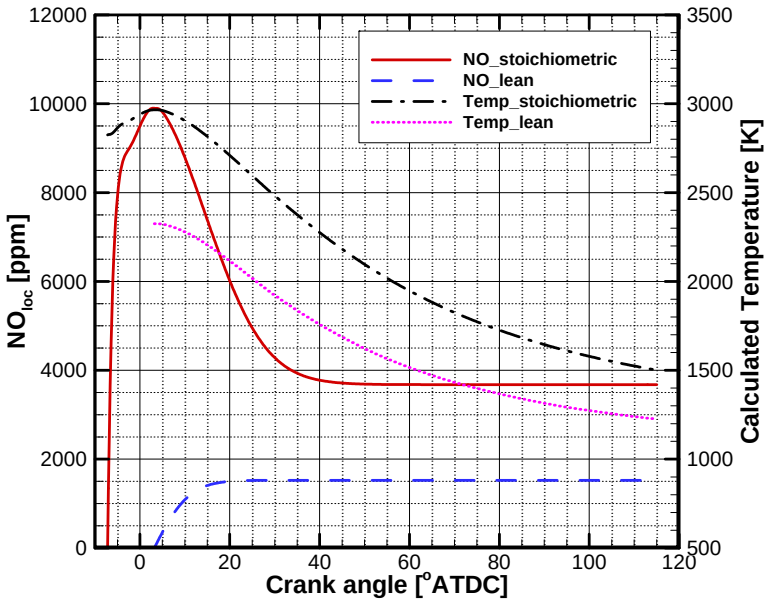

(a)

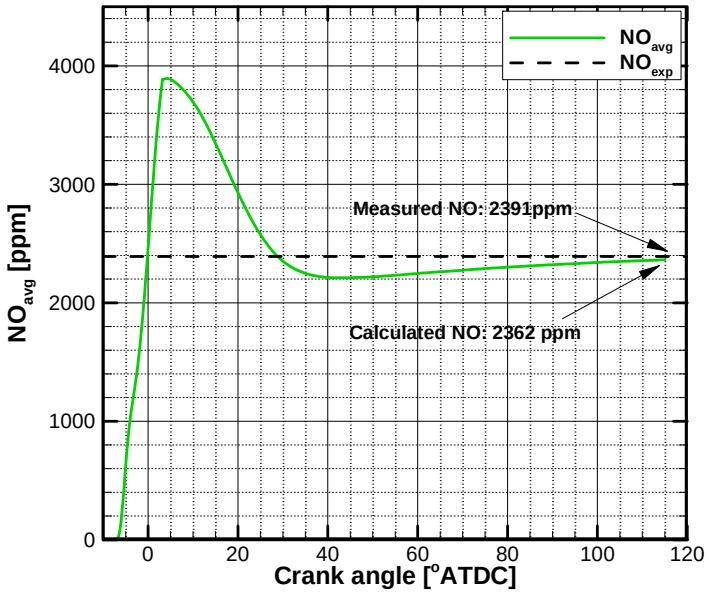

(b)

Figure 21 NO concentration with #2D at 1400 rev/min and 250 ft-lbs: (a) Zonal NO and temperatures, (b) Averaged NO concentration.

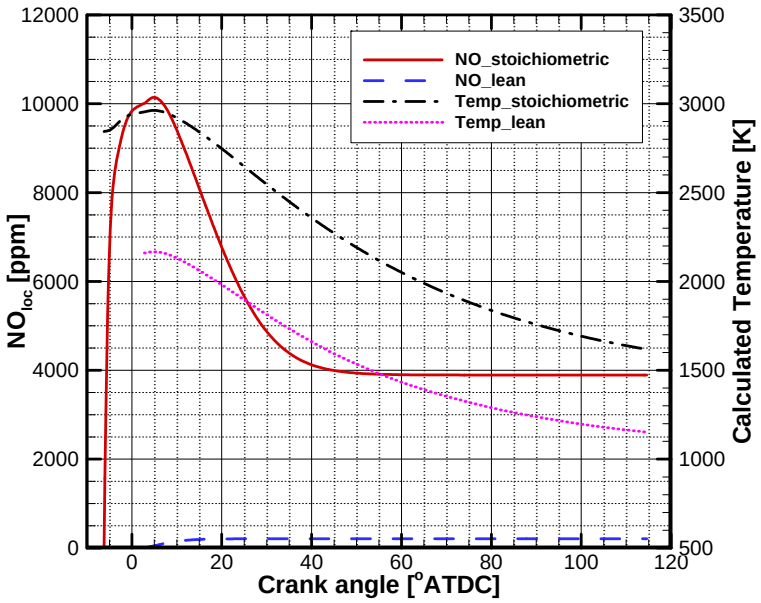

(a)

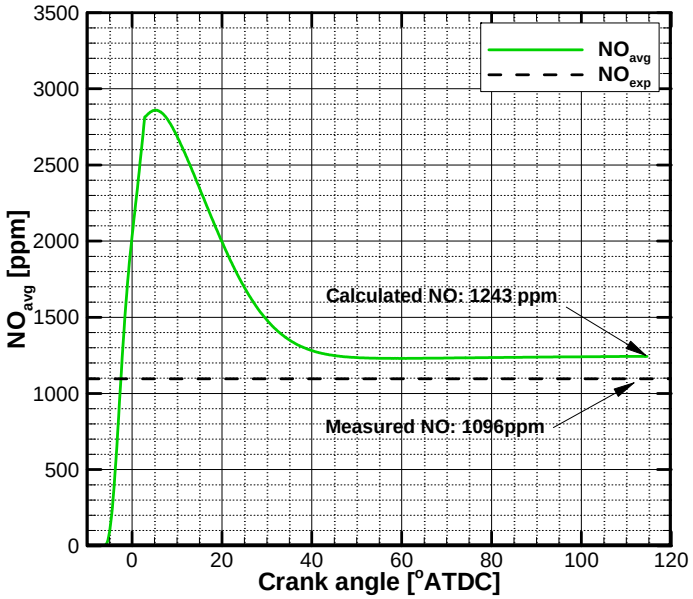

(b)

Figure 22 NO concentration with #2D at 2400 rev/min and 150 ft-lbs: (a) Zonal NO and temperatures, (b) Averaged NO concentration.

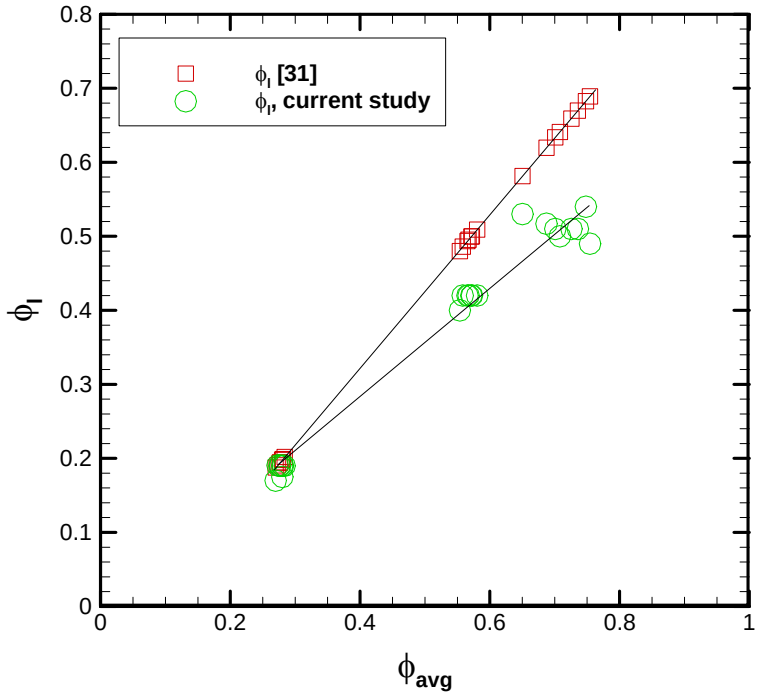

Figure 23 Correlation for the equivalence ration of the lean zone with #2D.

The initial equivalence ratio of the lean zone is calculated by using the correlation which is suggested by Szekely et al. [31]. The equivalence ratio is adjusted to match the calculated NO concentration to the experimental values. Through the NO calculations, the proper correlation for the equivalence ratio is formulated and is shown as following:

$$\phi_l = 0.748 \cdot \phi_{\text{avg}} - 0.0168 \qquad 4.1$$

where ϕ_l is the equivalence ratio of the lean zone.

ϕ_{avg} is the averaged equivalence ratio.

The slope of the correlation is lower than that suggested by Szekely et al. [31] as shown in Figure 23. When applying the above correlation to the cases with #2D, the calculated NO concentrations are shown and compared with the measured values as shown in Table 8. There are some uncertainty, which ranges up to + 14 %.

Table 8 Comparison between measured and calculated NO values with the correlation for #2D.

Engine condition	Fuel	Measured NO (ppm)	Calculated NO (ppm)	Difference (%)
1400 rev/min & 50ft-lbs	#2D	488	465	-4.7
1400 rev/min & 250ft-lbs	#2D	2391	2296	-4.0
2400 rev/min & 150ft-lbs	#2D	1096	1251	14.1

4.6 NO and FSN Results

The test results for NO concentration and Filter Smoke Number (FSN) are introduced in this section. NO results are showing real concentrations, but FSN results are relative valued. There are some correlations to convert FSN values to mass concentrations, which are suggested by Alikdas [49] and Christian et al. [50]. In the section, FSN is not converted to the mass concentration of soot. However, it would be useful to know the rough actual soot concentration to FSN as shown in Figure 24. Regarding that the maximum FSN is about 1, the corresponding mass concentration of soot would be less than 25 mg/m^3.

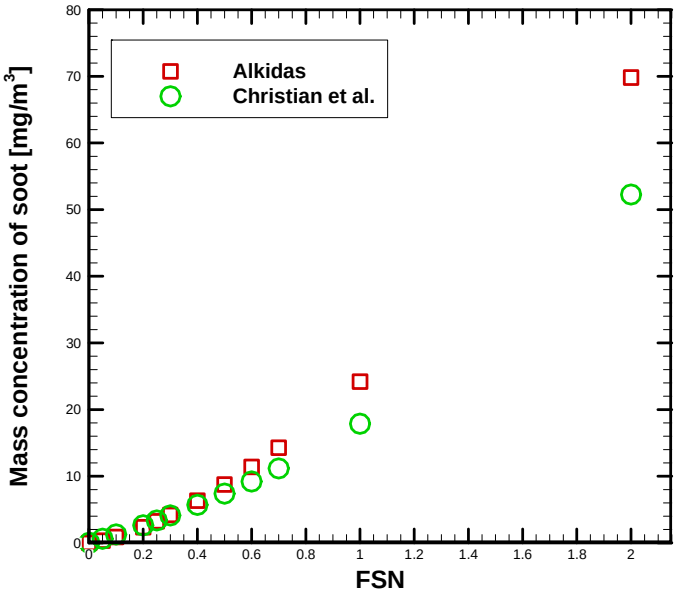

Figure 24 Mass concentration of soot calculated from FSN values.

Figure 25 through Figure 27 show the FSN and NO results with various barium additive concentrations at three different engine operating conditions. At 1400 rev/min and 50 ft-lbs in Figure 25, the fuels mixed with barium have higher NO concentrations than pure #2D, however, they have almost constant NO concentrations regardless of the barium concentration. Statistically, there is no significant difference.

At 1400 rev/min and 250 ft-lbs, it is even difficult to tell the tendency of NO concentrations as shown in Figure 26. The fuels mixed with 0.25 and 0.5 %-v barium additive show even lower NO concentrations than #2D. Considering the soot-NO trade-off, this tendency cannot be explained reasonably. Even at 2400 rev/min and 150 ft-lbs in Figure 27, there is not a clear trend of NO concentrations, either.

As a matter of fact, the barium additive clearly reduces FSN, since barium is known to effectively suppress the smoke formation during combustion processes [23], [24],[25], [51]. If there is a significant effect of soot radiation on NO concentration, the NO concentration would show the opposite tendency according to the trade-off relation. However, there is not the expected tendency of NO concentrations with the barium additive.

From this observation, two possible findings are offered. First, the soot radiation does not have as significant an influence on NO concentration as originally believed. However, the soot emissivity is estimated by using an analytical model suggested by Morel et al. [43] in the following section, since the analytical model would be able to capture the possible effect of soot that the experiment could miss. Second, there are other factors affecting NO concentration than soot radiation. Since NO is strongly dependent on thermal phenomena during combustion process, other factors can have more influence on NO concentration.

In addition to the second finding, it can be realized that the large standard deviation is caused by averaging data from two different days, even though the control parameters at any given operating condition (e.g., engine speed and load condition) are basically the same. It means that averaging data might lead to overlooking other factors to NO concentration. In order to resolve this problem, the data for each day is analyzed separately.

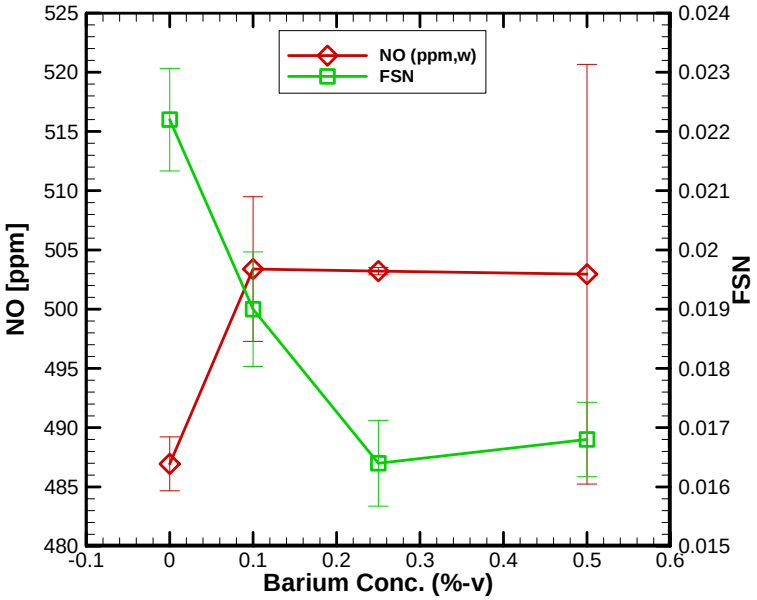

Figure 25 Filter smoke number and NO concentration results at 1400 rev/min and 50 ft-lbs with #2D.

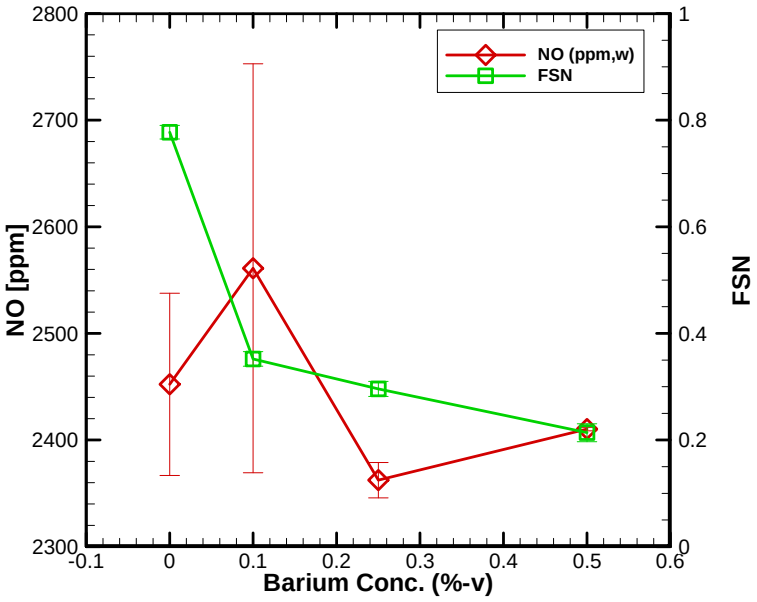

Figure 26 Filter smoke number and NO concentration results at 1400 rev/min and 250 ft-lbs with #2D.

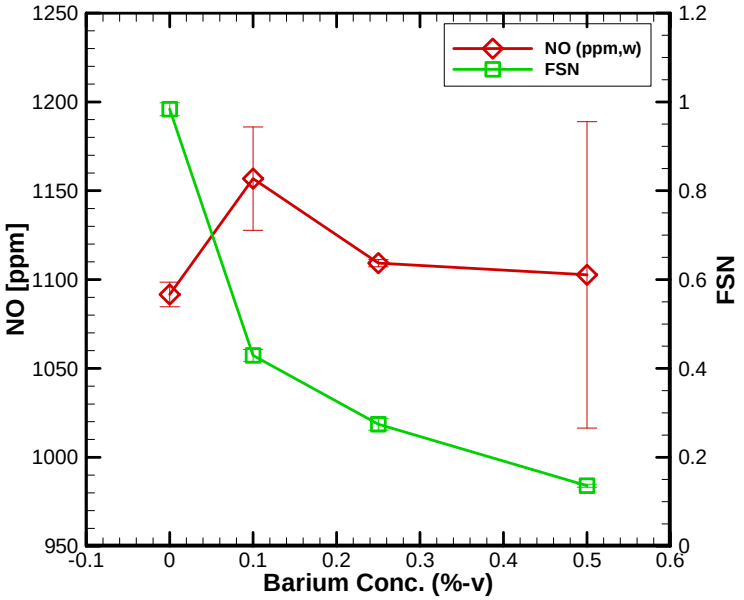

Figure 27 Filter smoke number and NO concentration results at 2400 rev/min and 150 ft-lbs with #2D.

In this study, it is assumed that NO is based on the thermal mechanism, in which temperature is a most important factor. So the measured temperature data needs to be investigated. Considering that the current engine uses ambient air without any process, the intake air temperature and humidity are totally dependent on the daily weather. It is therefore possible that the inconsistency of NO concentrations might be affected by the uncontrolled intake air conditions. In order to determine the relation of temperatures such as intake air and exhaust gas temperatures for the case of 1400 rev/min and 50 ft-lbs, the temperature data is illustrated in Figure 28. Both temperatures show the similar trend, but the case with 0.25% barium concentration of Day 2 shows a discrepancy. This point shows the highest intake air temperature and NO concentrations on Day 2, but has the second lowest exhaust temperature. Except for one case's exhaust temperature from

Day 2 (Point A in Figure 28(a)), the NO concentrations can be explained by using the intake temperature as shown in Figure 28(b). Point A has the latest start of combustion compared to other cases, which is defined using the 1% burned fuel fraction. Also it has the shortest period to burn 90 % fuel as shown in Figure 28(c). Thus, it shows the shortest combustion duration which is defined from 1 % to 90 % of the burned fuel fraction. It might mean that the fuel combustion occurs intensively in relatively short duration and causes high flame temperature. However, due to the early end of combustion, the expansion process could cool the product temperature lower than other cases. Thus, point A has higher NO concentrations possibly due to the higher temperature, but has lower exhaust temperature due to the early end of combustion.

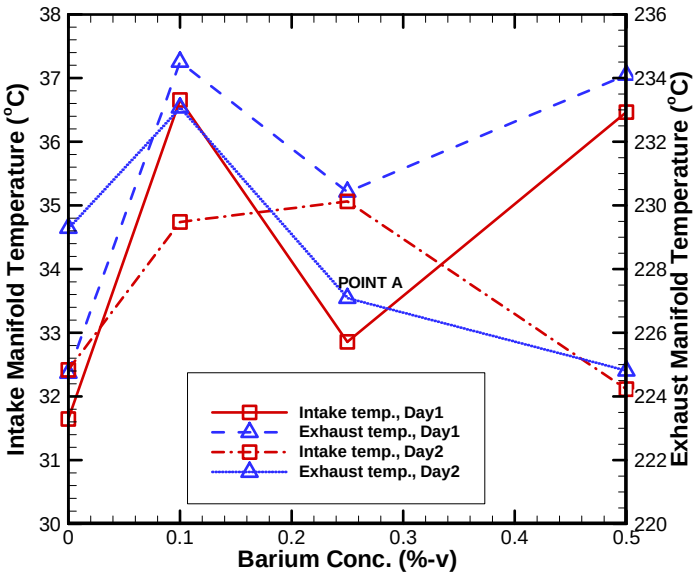

(a)

Figure 28 1400 rev/min and 50 ft-lbs: (a) intake and exhaust temperature, (b) NO concentration and intake temperature with barium additive concentration , and (c) 1 % and 90 % mass fraction burned location.

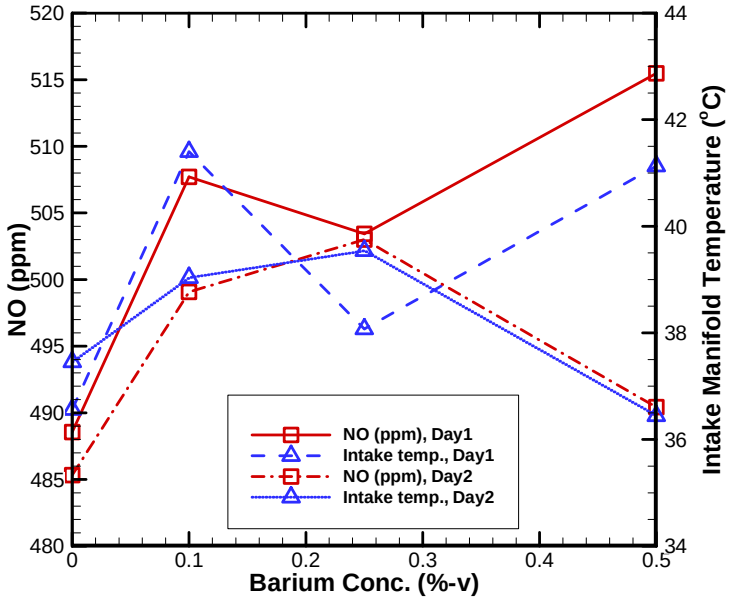

(b)

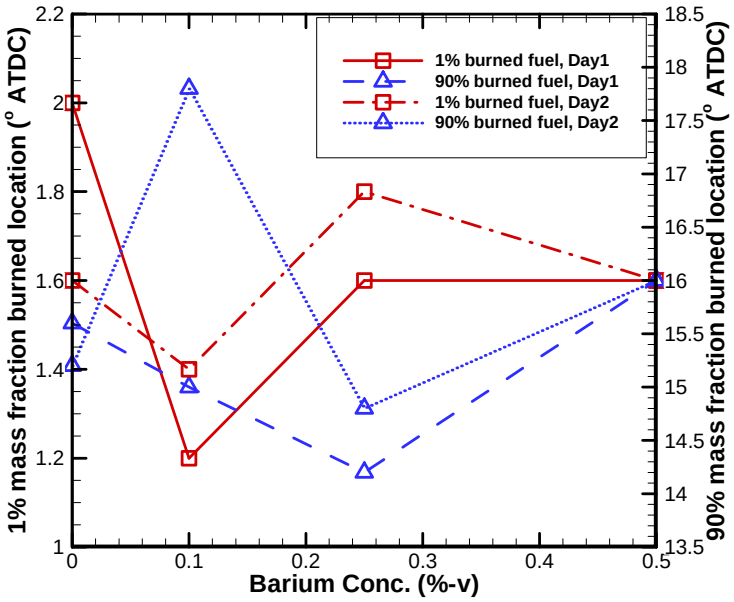

(c)

Figure 28 Continued.

The case of 1400 rev/min and 250 ft-lbs shows the similar trends between temperatures such as ambient air temperature, intake manifold air temperature, and exhaust gas temperature as shown in Figure 29 (a). However, the points, which are named as 'Point B' and 'Point C' at 0.1% barium concentration show lower intake aer temperatures (nearly ambient temperature), but higher NO concentrations as shown in Figure 29 (b). In order to investigate possible causes of the higher NO concentrations with low intake temperature, the starts and ends of combustion are compared with others. Even with low intake temperature, the cases have the earlier start and end of combustion as shown in Figure 29 (c). Thus, the higher flame temperature can be expected from the early start of combustion and might cause the increase in NO; however, the exhaust temperature is lower due to the early end of combustion and also due to the lower ambient temperature.

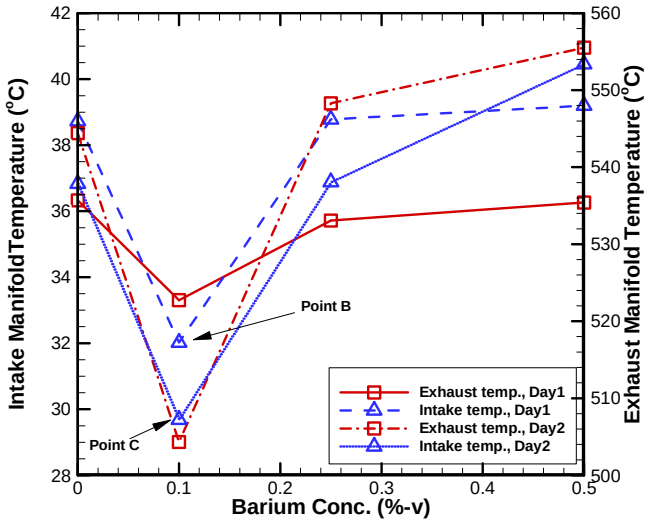

(a)

Figure 29 1400 rev/min and 250 ft-lbs: (a) intake and exhaust temperature, (b) NO concentration and intake temperature with barium additive concentration, and (c) 1 % and 90 % mass fraction burned location.

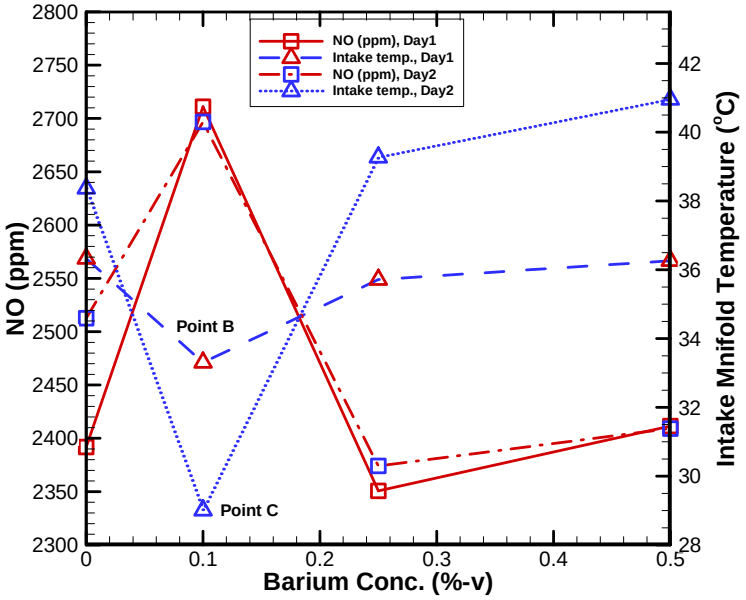

(b)

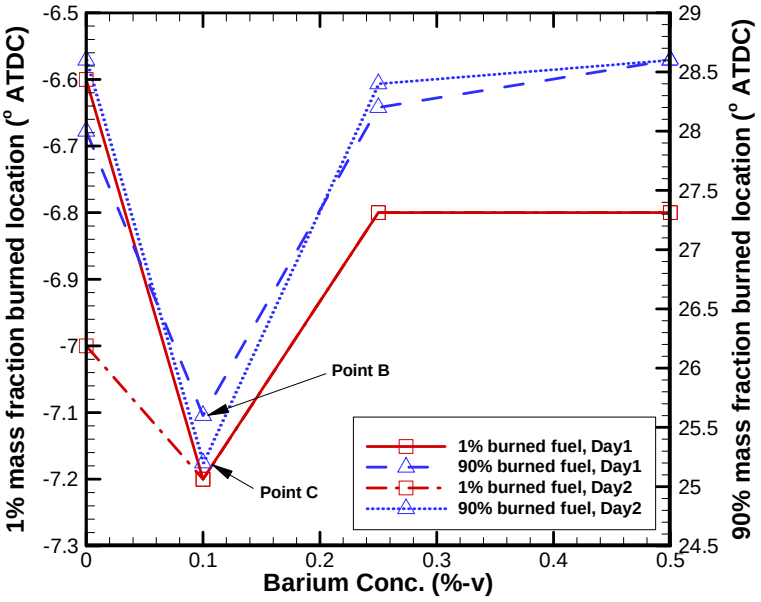

(c)

Figure 29 Continued.

Unlike the previous cases, the case of 2400 rev/min and 150 ft-lbs shows the similar trends between temperatures as shown in Figure 30. Also, NO concentrations follow the temperature trends. Thus, NO concentrations are strongly affected by the temperature since each test just has a different fuel with keeping other parameters constant.

Considering the effect of ambient temperature, the effect of soot may not have noticeable effect, even though it is decreased by the barium additive. It can be thought that the engine system does not have any equipment to control the ambient temperature. So the temperature of the system is changed by the ambient condition depending on the daily weather, even though there are several discrepancies possibly caused by the combustion characteristics.

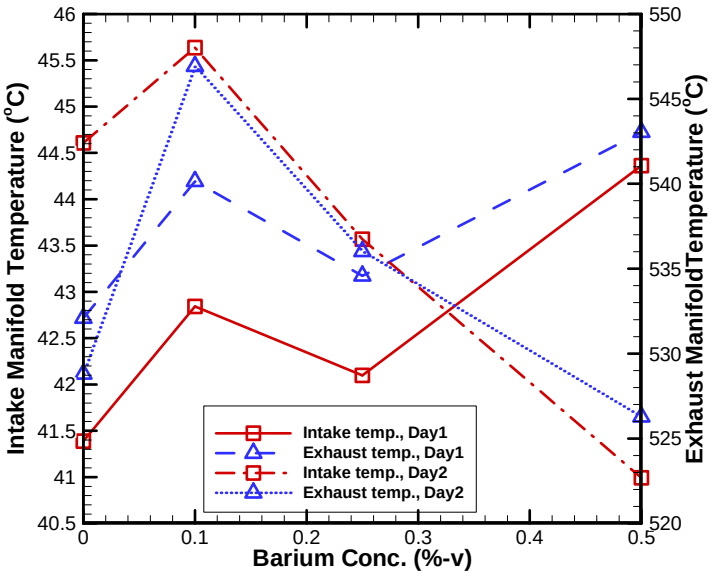

(a)

Figure 30 2400 rev/min and 150 ft-lbs: (a) intake and exhaust temperature, (b) NO concentration and intake temperature with barium additive concentration

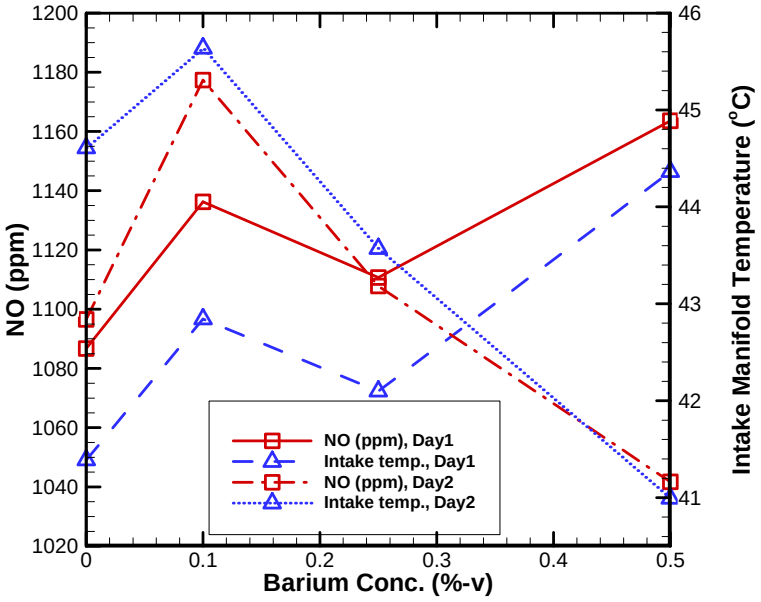

(b)

Figure 30 Continued.

4.7 Soot Emissivity

The effect of soot radiation on NO concentration is not found in the experimental results. However, it is necessary to estimate the soot emissivity in order to capture possible explanation for the trade-off relation. The soot emissivity is estimated by using the analytical model suggested by Morel et al. [43], which is empirically formulated only for diesel combustion. Thus, the correlation cannot consider the effects of the barium additive on soot radiation. In the present study, validation of the calculated soot emissivity cannot be performed as is done in [52], [53]. Regardless, the trend of emissivity with changing load in the references may be consistent with that shown in Figure 31. Since the correlation is related strongly to the in-cylinder pressure, it is reasonable to say that, if the soot radiation affects the combustion process and changes the combustion parameters such as in-cylinder pressure, the correlation is able to explain the difference of soot emissivity and, consequently, relate the soot radiation to NO concentration.

Figure 31 shows the rapid increase in emissivity with the start of combustion in each zone. However, the change of emissivity caused by the barium additive could not be found. There is a small shift of the emissivity due to the different combustion process. The calculation results show that the higher load case has higher peak emissivity in the lean zone. However, the peak emissivity in the stoichiometric zone is above 0.9 for all the fuel cases.

Thus, the emissivity calculation can show the general trend along with the combustion characteristic at each engine load condition, but cannot show the change of

soot emissivity that should exist during combustion since the experimental results shows the clear trend with the barium additive. In other words, the calculated emissivity cannot capture the influence of the barium additive on soot formation, while the FSN results clearly show the change of soot with the barium additive.

A possible reason is that the analytical model does not have detailed chemical reactions along with the diesel combustion. Thus, it might be difficult for the correlation to explain the change of combustion products. Also, it is difficult to capture the change of soot emissivity in this study where the in-cylinder pressure does not change significantly with the barium additive, since the correlation is strongly related to in-cylinder pressure.

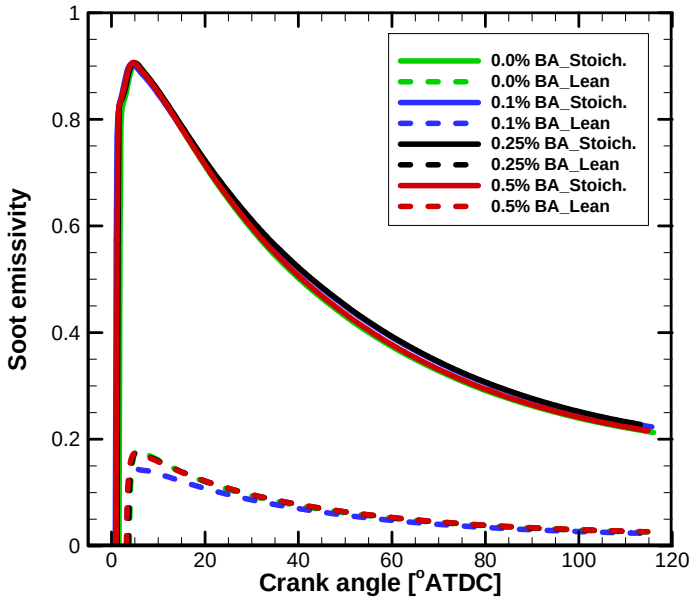

(a)

Figure 31 Soot emissivity results with #2D: (a)1400 rev/min and 50 ft-lbs, (b) 1400 rev/min and 250 ft-lbs, and (c) 2400 rev/min and 150 ft-lbs

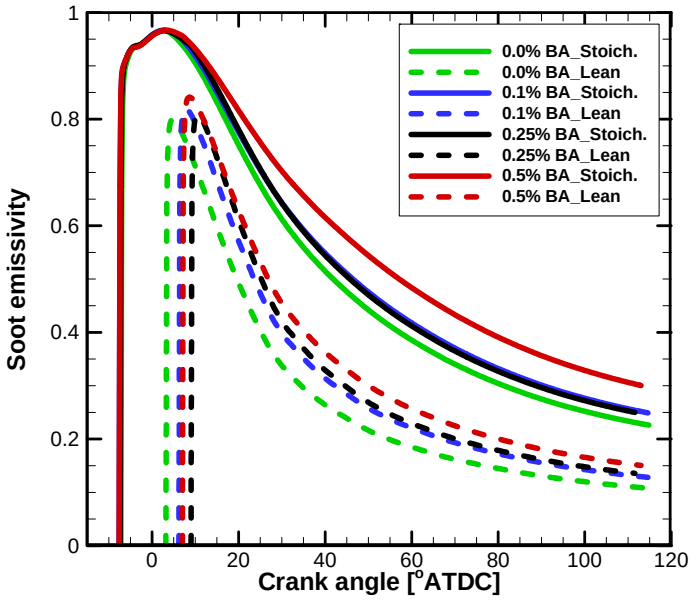

(b)

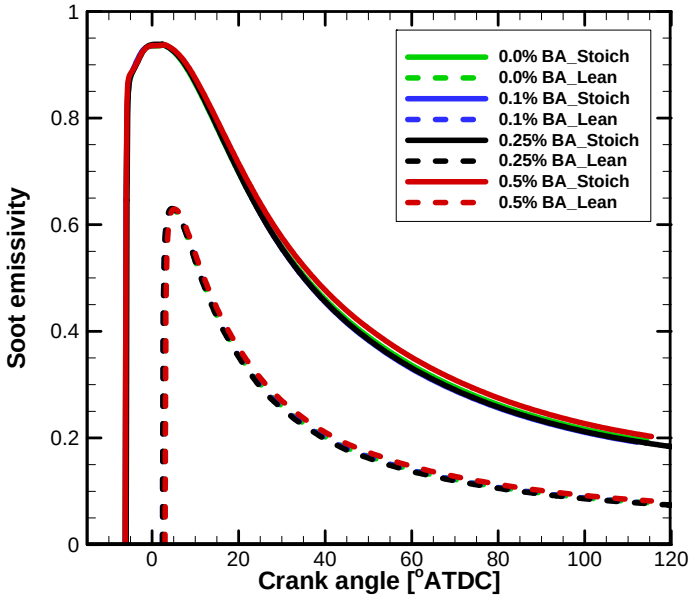

(c)

Figure 31 Continued.

4.8 Discussion

From the data analysis on each test day, it is shown that the NO concentration is affected by the ambient conditions rather than the soot concentration, which strongly affects the radiation during combustion. Since the current engine system does not have the air conditioning system, it breathes in unconditioned ambient air. It seems the effects of the ambient might be a big factor in this study, since other variable conditions do not change much except for the fuels with the barium additive. Adding the barium additive to #2D, however, does not noticeably change the fuel properties. Thus, the difference in NO concentration might be caused noticeably by the ambient condition such as intake air temperature. The analysis shows that the temperatures have the similar trends along with the ambient temperature except for a few points. The outliers (Points A, B, C) could be explained by applying the combustion characteristics such as the early start and end of combustion. The change in NO shows the similar trends as that in temperatures. Based on the thermal NO mechanisms, it is reasonable that when the combustion process could receive more thermal energy from the ambient conditions, it might have the higher flame temperature and produce more NO. Since the ambient temperature does not change dramatically daily, NO concentrations show the slight differences among the test conditions.

The two-stage model could show the calculated results such as heat release rate, burned fuel mass fraction, and NO concentrations. Regarding the heat release rate, it could not show any noticeable difference in heat release rate caused by the barium additive, but show the general trend of combustion process. In other words, the in-

cylinder pressure is not able to capture changes possibly caused by the barium additive. It would be the major reason why the soot emissivity correlation could not show any difference between different fuels.

The analytical model could show the calculated NO concentrations. In general, the NO concentration increases drastically with the start of combustion, reaches a peak value and decreases slowly to a constant value with chemically frozen species. The results show negligible NO concentrations in the lean zone, when the temperature is below 1800K. The calculation results of NO concentrations are reasonably close to the measured ones.

The soot emissivity results show the general trend with the engine load and speed. The specific change of soot emissivity caused by the barium additive, however, could not be captured. The first reason might be that the soot change by the barium could not be captured by the measured in-cylinder pressure; the empirical correlation for the soot emissivity is strongly related to in-cylinder pressure. If the experimental results could not capture the differences between fuel conditions, the soot emissivity correlation would not be able to explain the soot emissivity. The second possible cause is that the correlation itself is not able to capture the effects of the barium additive since the correlation is developed for standard diesel fuel, without regard to alternative fuels or additives. An improved “fuel-neutral” correlation could help the model to explain the soot emissivity.

5 RESULTS AND DISCUSSION OF BIODIESEL TESTS

In this section, the test results with biodiesel are discussed. For the experiments, 0.25 %-v of the barium additive is applied to the palm olein oil (B100) in order to study the possible impact of the barium additive on NO concentration excluding the biodiesel fuel effects.

For NO formation with biodiesel, three fuel types are tested: 100% petroleum diesel (#2D), a 20%-v palm olein biodiesel mix with petroleum diesel (B20), and a 100% palm olein biodiesel (B100. The engine operating conditions are the same as #2D tests: 1400 rev/min and 50 ft-lbs, 1400 rev/min and 250 ft-lbs, and 2400 rev/min and 150 ft-lbs. Along with the experimental results, the two-stage model is also used to investigate NO concentration and FSN.

5.1 The Effects of the Barium Additive on NO

In diesel fuel test, the soot effects are studied by applying the barium additive, assuming that the barium additive affects the soot formation. However, it cannot be overlooked that NO may be affected directly by the barium additive. Thus, it is necessary to investigate the possible effects of the barium additive on NO formation.

In order to exclude the fuel effects on NO formation, the pure biodiesel, B100, is used with and without the barium additive. B100 basically produces lower soot than the conventional diesel, so the possible effects of soot radiation on NO formation are

weakened by using biodiesel. Note that even with using biodiesel fuel, the soot cannot be removed completely due to the heterogeneous combustion.

At 1400 rev/min and 50 ft-lbs, B100 case shows higher FSN, but lower NO results than one with 0.25%-v BA. The barium additive reduces FSN effectively, which ranges from 0.013 to 0.040. The test results from Day 1 and Day 2 are still small degree regarding the FSN resolution of 0.001 as shown in Table 9.

NO concentration seems not to be affected by the barium additive at this condition as shown in Table 9. Rather, the intake air temperature seems to affect the NO concentration. The results of Day 1 show that the B100 case has the intake air temperature that is 4.7 ^{o}C lower than B100 with 0.25% BA. The corresponding NO concentration results show the proportional relation with the intake air temperature.

The results from Day 2 show that both B100 and B100 with 0.25% BA have almost identical intake air temperatures as shown in Table 9. Also, NO concentrations seem to be identical and have the small difference of 2 ppm.

Thus, the higher intake air temperature causes NO concentrations to increase since the higher intake air temperature can advance the start of combustion and make the available combustion duration longer enough for NO formation. Since B100 with 0.25% BA has a higher intake air temperature on Day1, it has a higher averaged NO value as shown in Figure 32(a).

Since the two fuels are differed by adding 0.25 %-v BA, the original properties of B100 would not be changed noticeably. As a result, the in-cylinder pressure profiles are observed almost identical in Figure 32(b). The corresponding heat release rates show

the identical start of combustion, peak value, and burning rate in Figure 32(c). For these reasons, the calculated temperatures of the both cases are in a good agreement as shown in Figure 32(d).

Since both cases show the similar temperature profiles, the calculated NO values based on the temperatures have the similar trends except for the small differences in the final NO value; NO is increased, reaches at the peak value, and is decreased smoothly to a constant value as shown in Figure 33.

Table 9 Changes in NO and FSN at 1400 rev/min and 50 ft-lbs with B100.

	Fuel	NO(ppm)	FSN	Intake temp.(^{o}C)	IMT(^{o}C)
Day 1	B100	344.50	2.76E-02	30.13	34.87
	B100 w/ 0.25%	358.86	1.32E-02	34.82	38.82
Day 2	B100	367.48	3.96E-02	33.12	37.97
	B100 w/ 0.25%	364.23	1.54E-02	33.80	37.66

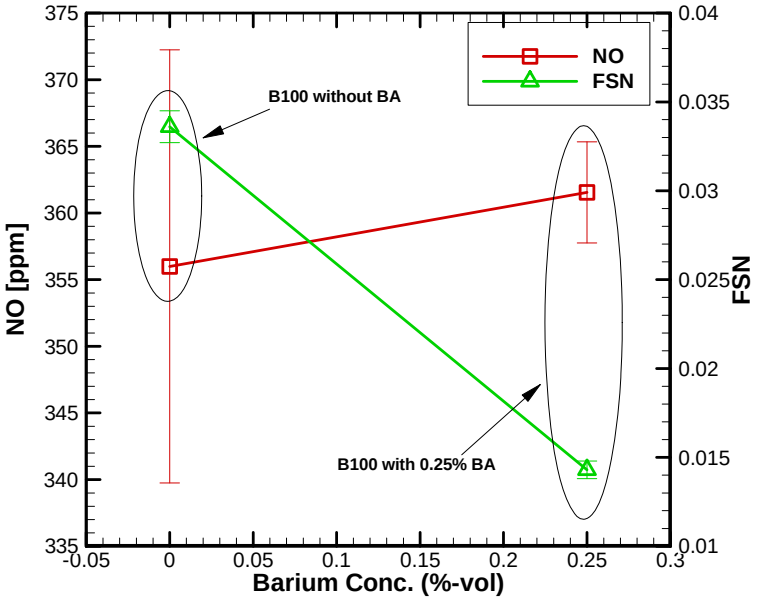

(a)

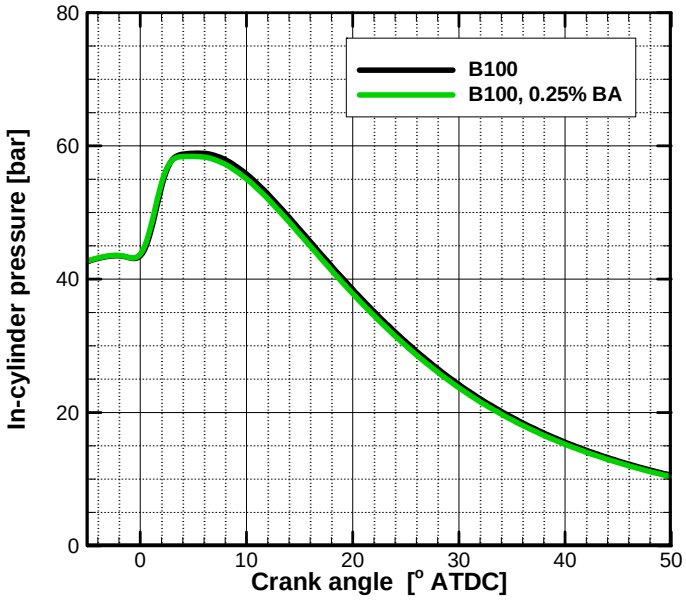

(b)

Figure 32 Experimental results at 1400 rev/min and 50ft-lbs with B100: (a) NO and FSN results, (b) in-cylinder pressure result, (c) heat release rate and mass fraction burned, and (d) average temperatures.

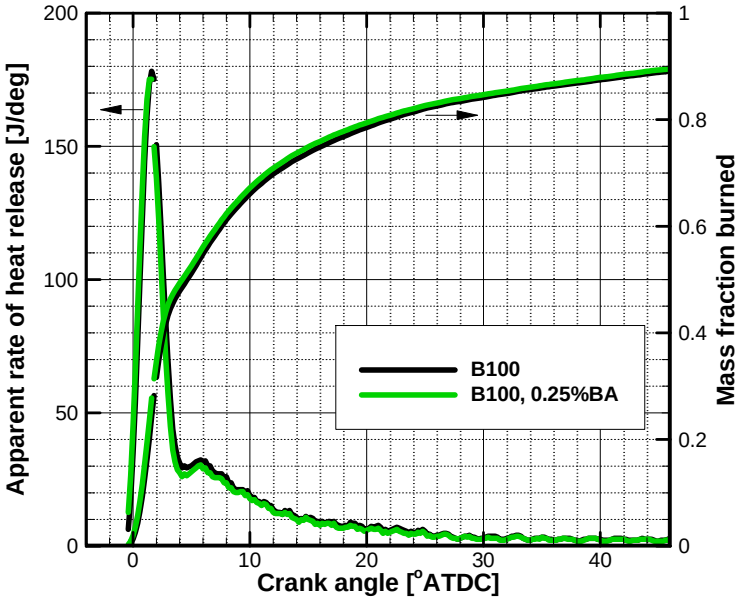

(c)

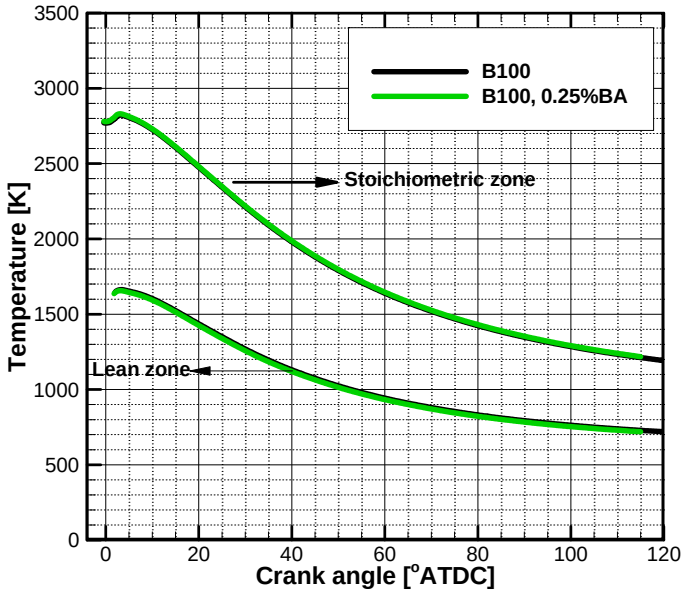

(d)

Figure 32 Continued.

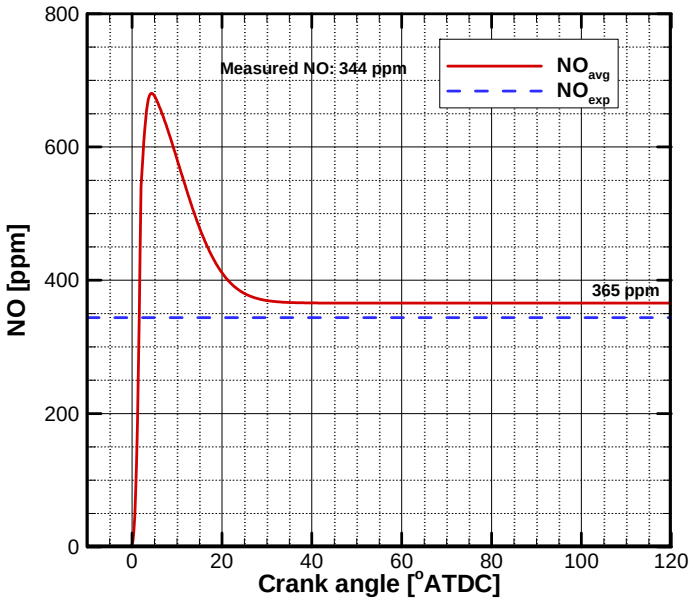

(a)

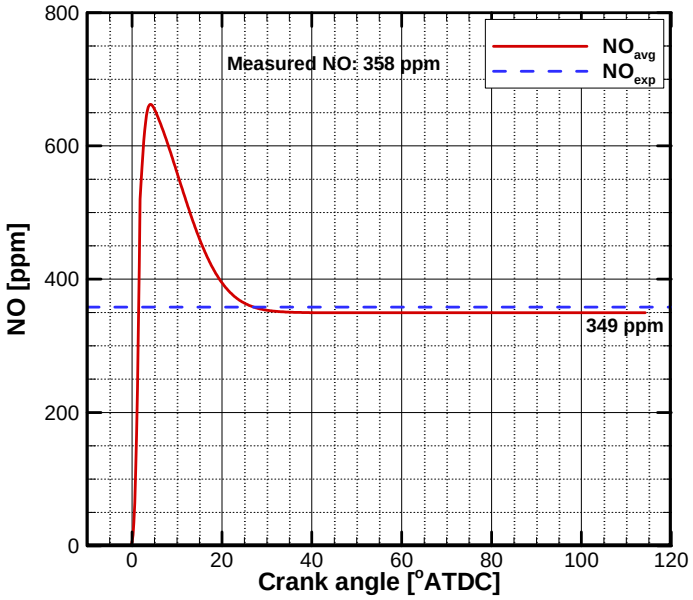

(b)

Figure 33 NO concentration (a) for B100 and (b) for B100 with 0.25 % BA at 1400 rev/min and 50 ft-lbs.

At 1400 rev/min and 250 ft-lbs, the trends of FSN and NO results are similar to the previous one: FSN is reduced by the barium additive, while NO is increased as shown in Table 10 and Figure 34(a). However, the change in NO is not as clear as that of the FSN caused by the barium additive. As taking a look at NO and intake air temperature, NO concentrations increase with the intake air temperature. From Day 2, both fuel cases have similar intake air temperature and they show similar NO concentrations. B100 with 0.25 %-v BA has higher intake air temperature and, thus, has higher NO concentrations.

Table 10 Changes in NO and FSN at 1400 rev/min and 250 ft-lbs with B100.

	Fuel	NO(ppm)	FSN	Intake temp.(^{o}C)	IMT(^{o}C)
Day 1	B100	2786.70	3.21E-01	35.60	42.05
	B100 w/ 0.25%	2878.93	8.64E-02	39.44	45.86
Day 2	B100	2839.82	3.40E-01	37.06	44.86
	B100 w/ 0.25%	2861.05	8.90E-02	38.14	44.36

Like the previous case, there are no noticeable differences in the in-cylinder pressures and heat release rates as presented in Figure 34 (b) and (c). B100 with 0.25 %-v BA shows higher temperature profiles than B100 case in Figure 34 (d). Additionally, B100 with the additive has a higher intake air temperature, so it may have higher NO concentrations.

Due to the difference in temperature, B100 case has the lower peak value as shown in Figure 35. However, the general trend of NO is similar to each other. The final values are close to the experimentally measured ones.

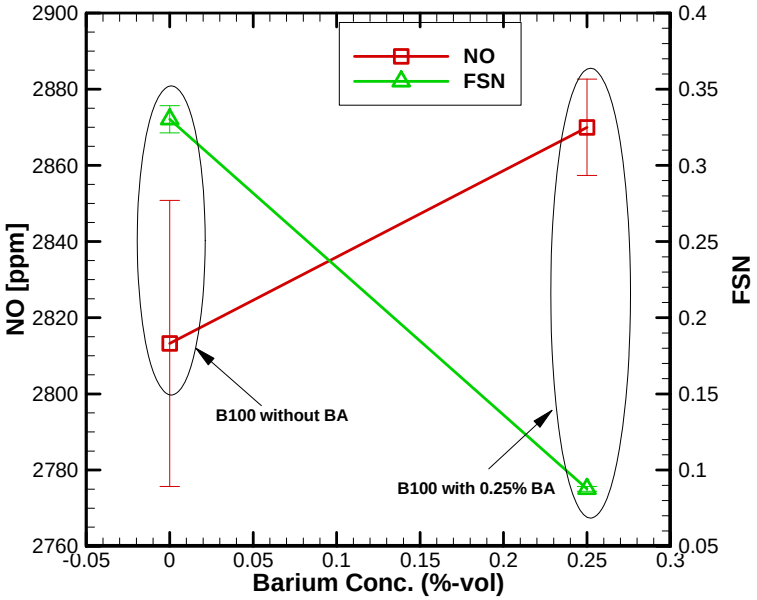

(a)

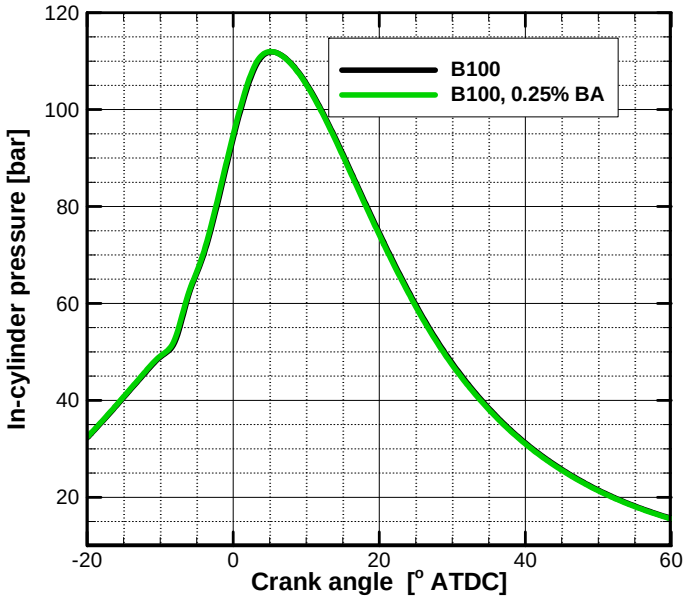

(b)

Figure 34 Experimental results at 1400 rev/min and 250ft-lbs with B100: (a) NO and FSN results, (b) in-cylinder pressure result, (c) heat release rate and mass fraction burned, and (d) average temperatures.

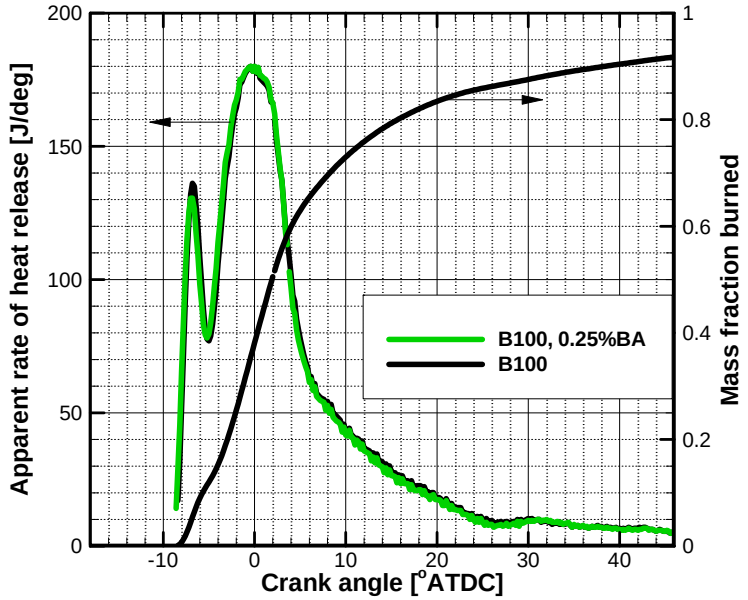

(c)

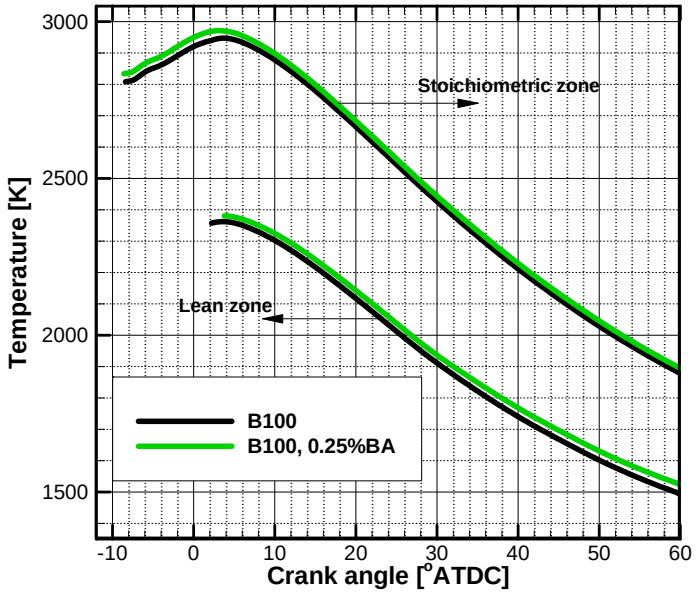

(d)

Figure 34 Continued.

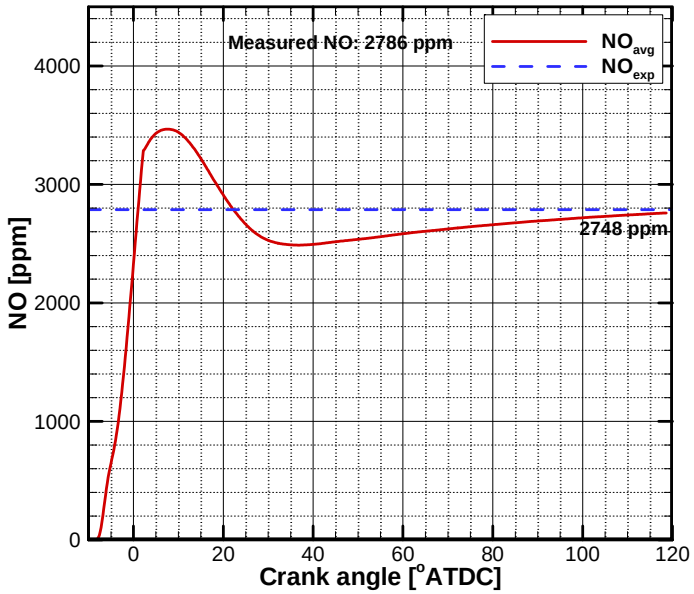

(a)

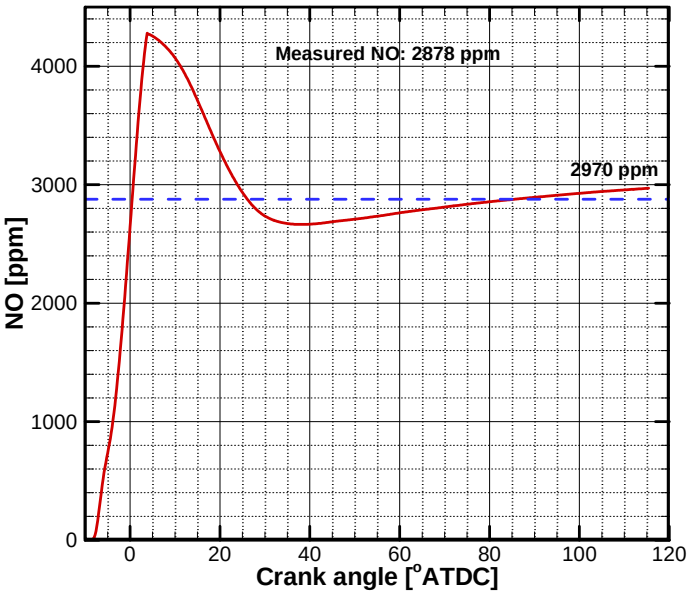

(b)

Figure 35 NO concentration (a) for B100 and (b) for B100 with 0.25 % BA at 1400 rev/min and 250 ft-lbs.

At 2400 rev/min and 150 ft-lbs, the similar trends of NO and FSN are observed. FSN is clearly decreased by the barium additive. Even with lower intake air temperature and identical start of combustion, B100 case show slightly higher in-cylinder pressure, heat release rates and calculated temperature profiles as shown in Figure 36. In terms of thermal NO mechanism, however, the differences do not seem to cause NO concentration to change because B100 case emits less NO than B100 with 0.25 %-v BA.

From Day 1, B100 case has the lowest intake air temperature and NO concentration. As shown in Table 11 at Day 2, both fuel cases have almost identical intake air temperature, thus the only difference is the fuel condition changed by the barium additive. However, the results show a proportional increase in NO with the intake air temperature. Like the previous cases, the higher intake air temperature, the higher NO. Thus, it is concluded that the barium additive does not affect NO formation, but the ambient temperature seems to be the decisive factor on NO formation.

NO concentration is estimated as shown in Figure 37. Even though B100 case has the higher peak value due to the higher temperature, the final NO value of B100 is lower than that with 0.25 %-v BA.

Table 11 Changes in NO and FSN at 2400 rev/min and 150 ft-lbs with B100.

	Fuel	NO(ppm)	FSN	Intake temp.(^{o}C)	IMT(^{o}C)
Day 1	B100	1146.72	2.49E-01	33.17	38.67
	B100 w/ 0.25%	1209.80	6.20E-02	37.80	43.21
Day 2	B100	1216.10	2.98E-01	36.47	41.64
	B100 w/ 0.25%	1228.02	6.18E-02	36.79	42.31

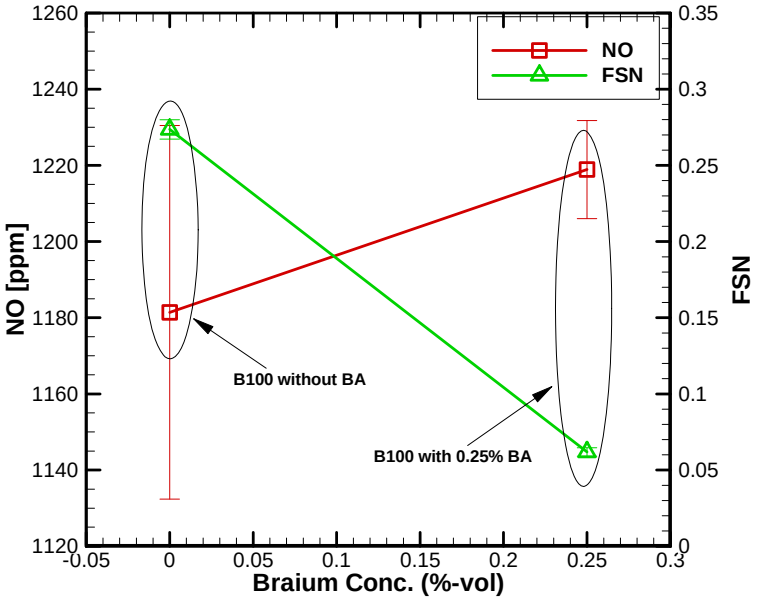

(a)

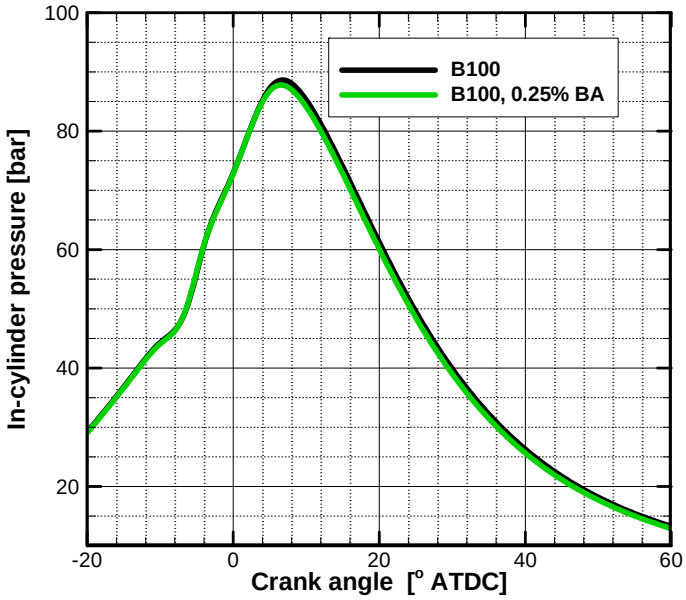

(b)

Figure 36 Experimental results at 2400 rev/min and 150ft-lbs with B100: (a) NO and FSN results, (b) in-cylinder pressure result, (c) heat release rate and mass fraction burned, and (d) average temperatures.

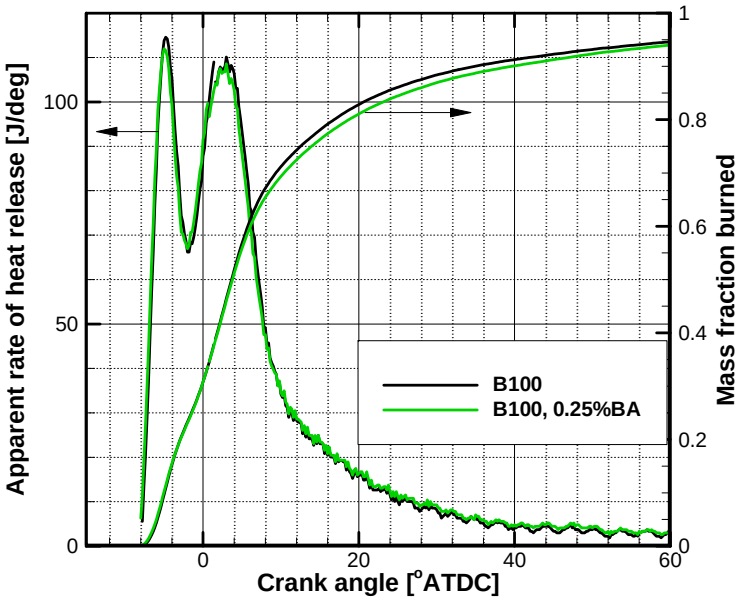

(c)

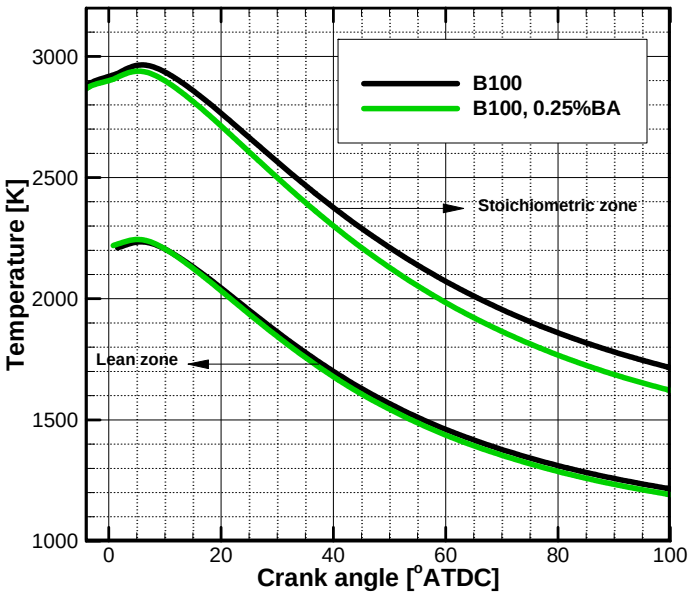

(d)

Figure 36 Continued.

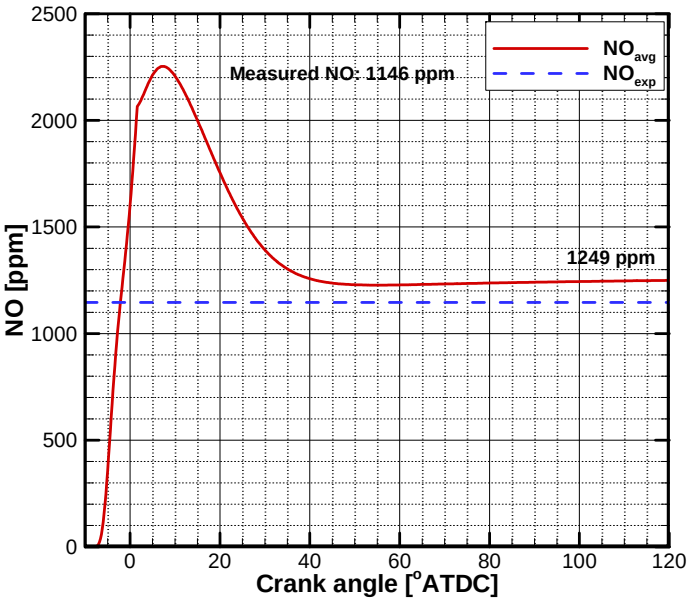

(a)

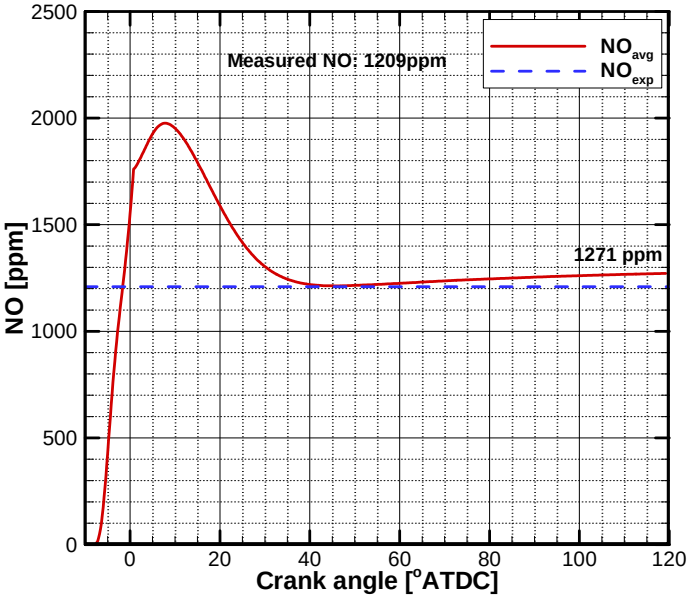

(b)

Figure 37 NO concentration (a) for B100 and (b) for B100 with 0.25 % BA at 2400 rev/min and 150 ft-lbs.

In this section, the effects of the barium additive are investigated by using the pure biodiesel fuel (B100). Even by treating the fuel with a small amount of the barium additive, FSN results show a clear trend. In contrast, the trend of NO is observed to be unaffected directly by the additive. Rather, the ambient temperature is the dominant factor to the NO formation. Therefore, it can be concluded that the barium additive does not have any direct effects on NO formation.

5.2 NO and FSN Results

In order to study NO and FSN changes in biodiesel combustion, #2D, B20 and B100 are tested. Figure 38 shows that FSN is increased, but NO is reduced with the biodiesel percentage at 1400 rev/min and 50 ft-lbs. It is opposite to the general observations in other studies [54], [55], [56] that NO concentration is increased by the content of biodiesel to the baseline diesel fuel (#2D). FSN results show 20.7 and 51.4% increase by adding biodiesel as shown in Table 12.

Figure 39 shows the in-cylinder pressure profiles at 1400 rev/min and 50 ft-lbs. The profiles are similar except for #2D case. B100 has the earliest pressure rise, and B20 in turn has the slightly later one. While #2D case has the latest one, it has the highest peak pressure.

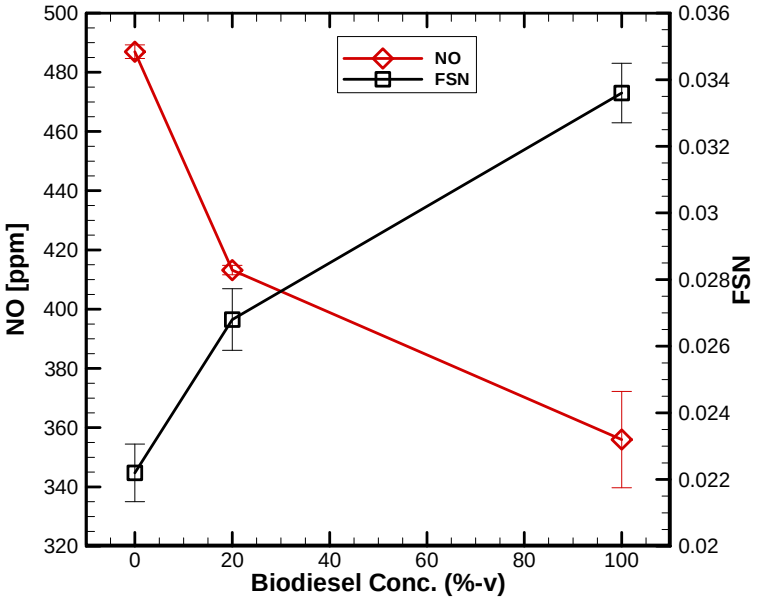

Figure 38 NO and FSN at 1400 rev/min and 50 ft-lbs with biodiesel fuels.

Table 12 Changes in NO and FSN with biodiesel fuels.

Engine condition	Fuel condition	NO[ppm]	% change	FSN	% change
1400 rev/min, 50 ft-lbs	#2D	486.9	0	0.0222	0
	B20	413.2	-15.1	0.0268	20.7
	B100	356.0	-26.90	0.0336	51.4
	B100, 0.25%BA	361.5	-25.8	0.0143	-35.6
1400 rev/min, 250 ft-lbs	#2D	2332.5	0	0.8096	0
	B20	2606.9	11.8	0.6313	-22.0
	B100	2813.3	20.6	0.3303	-59.2
	B100, 0.25%BA	2870.0	23.0	0.0877	-89.2
2400 rev/min, 150 ft-lbs	#2D	1091.6	0	0.9835	0
	B20	1118.9	2.5	0.5898	-40.0
	B100	1181.4	8.2	0.2736	-72.2
	B100, 0.25%BA	1218.9	11.7	0.0619	-93.7

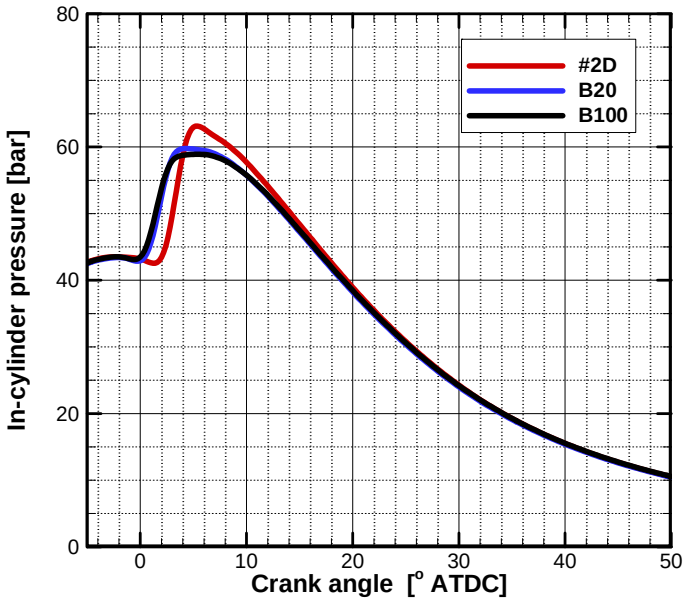

Figure 39 In-cylinder pressure at 1400 rev/min and 50 ft-lbs with biodiesel fuels.

Figure 40 illustrates heat release rates; B100 and B20 cases have earlier starts of combustion and shorter ignition delay than #2D case due to the cetane number, which is an indicator for the ignition quality in diesel fuel combustions [1]. The other properties of biodiesel such as surface tension, viscosity, and volatility may cause poor fuel evaporation and lead to smaller heat release in the premixed combustion phase, even though biodiesel combustion has earlier ignition. Due to the longer ignition delay of #2D, it has the highest peak heat release rate, which may cause the higher peak and overall temperature of #2D case.

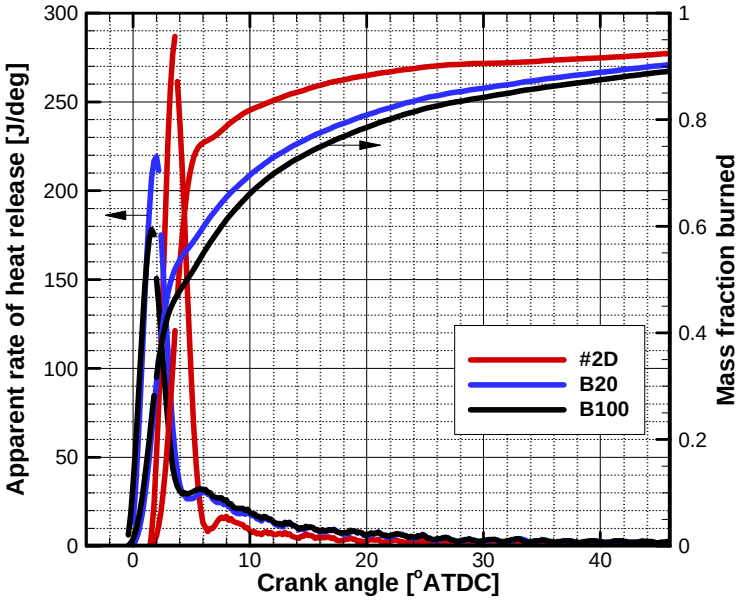

Figure 40 Apparent rate of heat release at 1400 rev/min and 50 ft-lbs with biodiesel fuels.

As shown in Figure 40, the fuel mass fraction burned shows that #2D case earliest reaches 90 % of mass fraction burned even with the latest start of combustion. Thus, #2D case has relatively faster combustion process at this engine condition. The given fuel energy is consumed for a shorter duration, and the resultant higher temperature may contribute to higher NO concentration as shown in Figure 41.

Figure 41 shows the comparison of temperatures, which are calculated by using the two-stage model. Each case has two temperature results for stoichiometric and lean zones. #2D has highest temperature in the stoichiometric combustion. Relating to the thermal NO mechanism, the higher temperature profile of #2D could explain the higher NO in the stoichiometric zone as shown in Figure 42. In the same way, B20 case shows

slightly higher temperature profile than B100, so the B20 case has higher NO than B100 as shown in Figure 43 and Figure 44.

In addition to this, the temperature of the lean zone is lower than 1800 K, which is the temperature limit for the thermal NO formation. Thus, the calculated NO is so negligibly small in the lean zones that the calculated NO for the lean zone is not presented in Figure 42 through Figure 44.

At the same time, the results raise the question, "Why does #2D have a higher peak and higher temperature profile?" Lyn et al. [47] suggests that longer ignition delay could cause higher peak in the premixed combustion. Since the #2D case shows the longest ignition delay, it might have highest peak heat release rate. As biodiesel has higher cetane number compared to #2D, B100 has the shortest ignition delay [1], [10]. This means that there is longer time for #2D and air to mix well together, so the #2D case might be able to convert more heat energy and consequently have higher temperature than biodiesel cases. In addition, shorter combustion timing means that the less time is available for NO formation before the reactions are quenched by expansion processes [57].

In terms of FSN, the shorter ignition delay (available time) seems to cause higher inhomogeneity in air-fuel mixture, which means poor combustion quality and high soot levels. Accordingly, Figure 38 shows that B100 and B20 have higher FSN than #2D, even though the differences in FSN are small since the combustion at this condition is dominated by the premixed combustion.

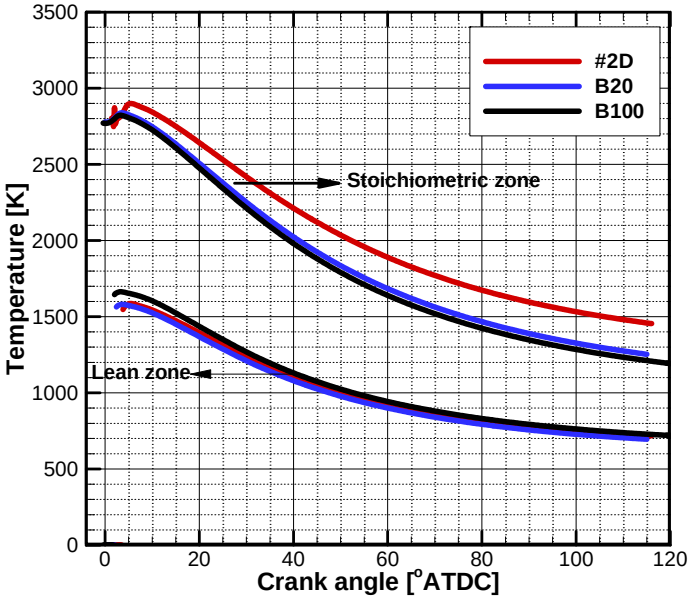

Figure 41 Average temperature calculated from the two-stage model at 1400 rev/min and 50 ft-lbs with biodiesel fuels.

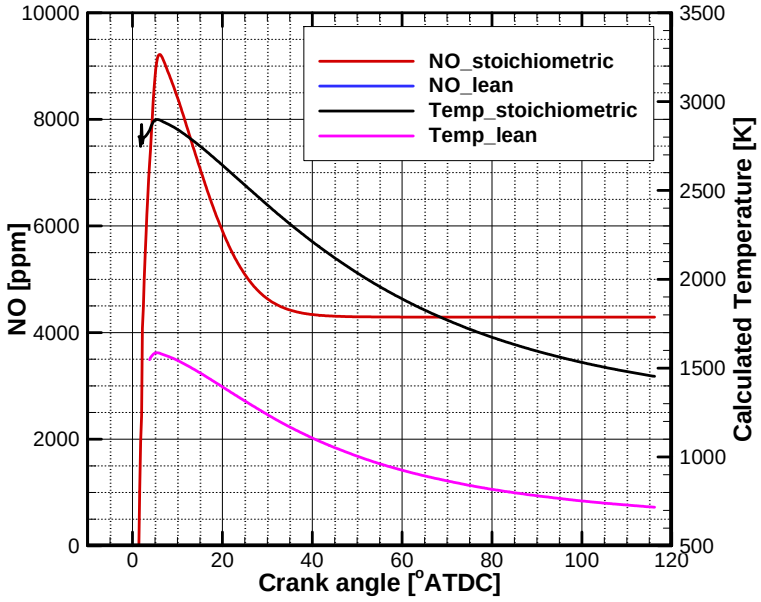

(a)

Figure 42 NO concentration for #2D at 1400 rev/min and 50 ft-lbs: (a) Zonal NO and temperatures, and (b) averaged NO concentration.

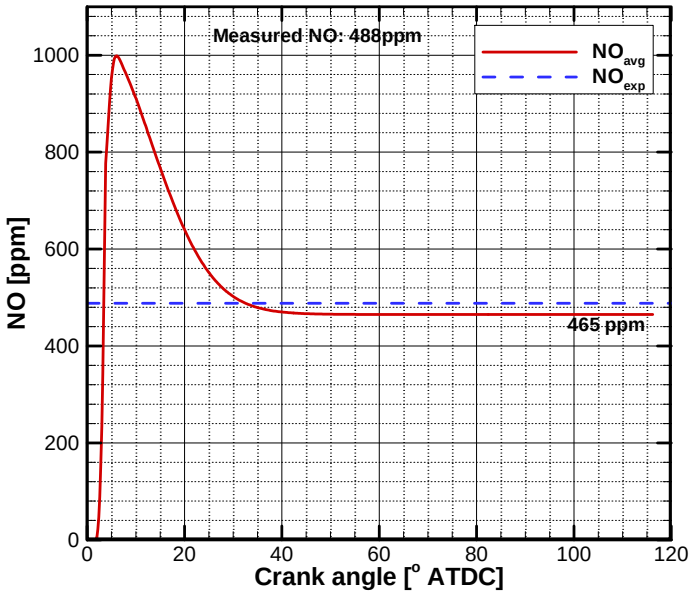

(b)

Figure 42 Continued.

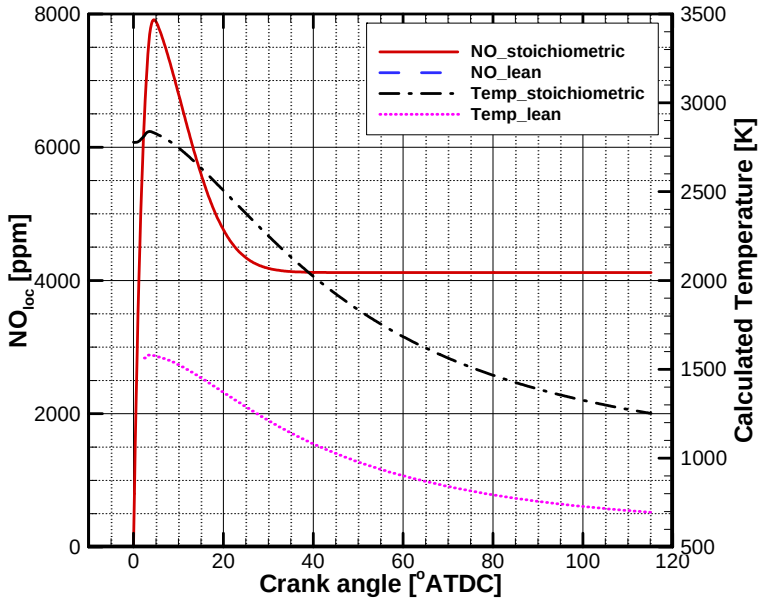

(a)

Figure 43 NO concentration for B20 at 1400 rev/min and 50 ft-lbs: (a) Zonal NO and temperatures, and (b) Averaged NO concentration.

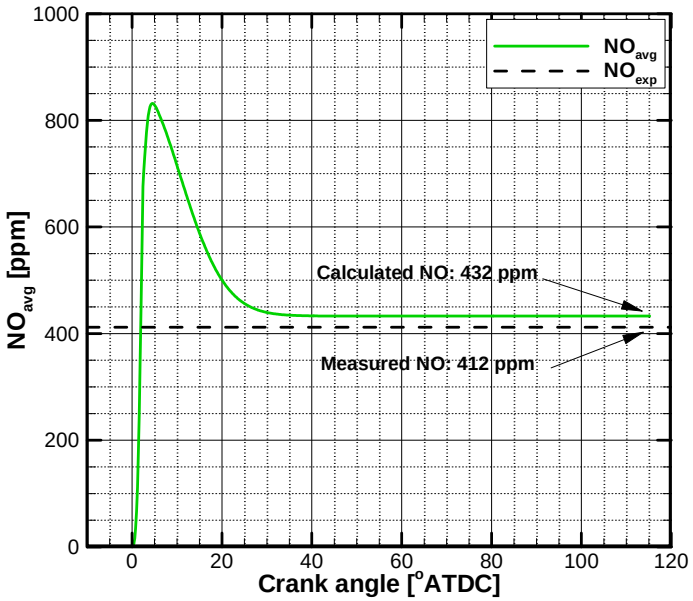

(b)

Figure 43 Continued.

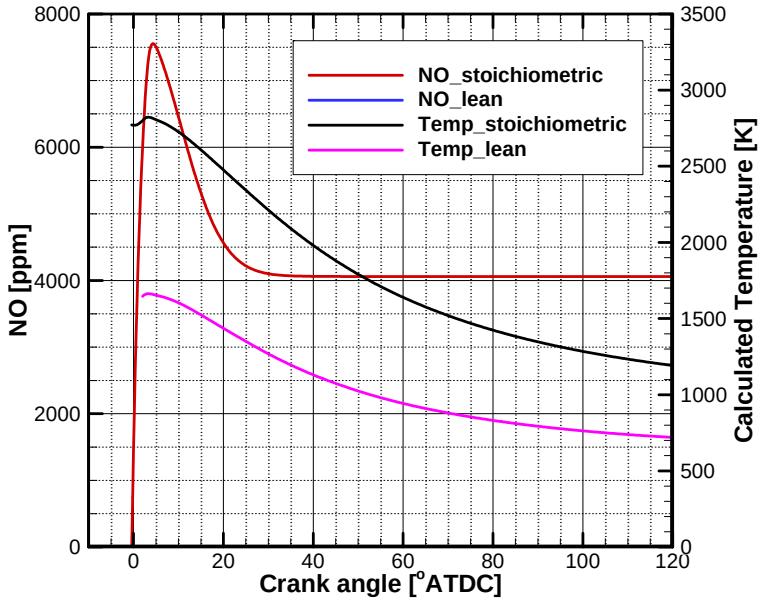

(a)

Figure 44 NO concentration for B100 at 1400 rev/min and 50 ft-lbs: (a) Zonal NO and temperatures, and (b) Averaged NO concentration.

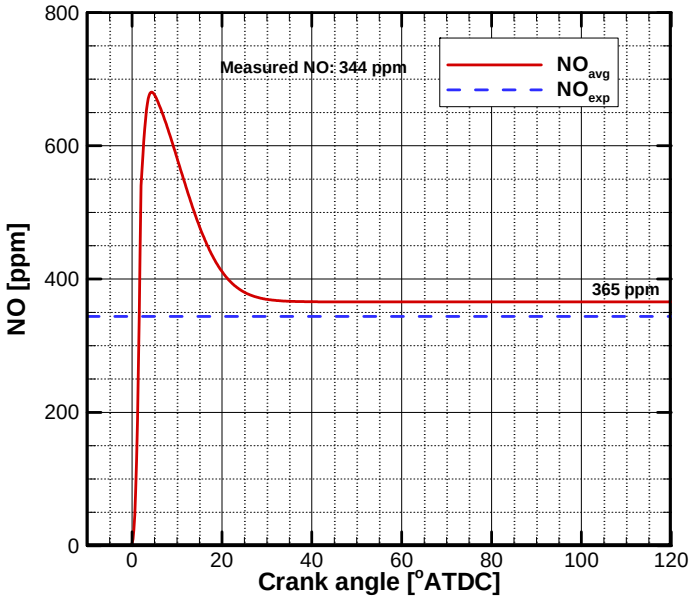

(b)

Figure 44 Continued.

At 1400 rev/min and 250 ft-lbs, NO is increased with biodiesel percentage, whereas FSN is reduced as shown in Figure 45, opposite to those of the previous case at 1400 rev/min and 50 ft-lbs.

Figure 46 shows the in-cylinder pressure profiles, which has steeper rise and higher peak value than the case at 1400 rev/min and 50 ft-lbs. The figure shows that B100 has the earliest rise compared to other fuel cases; the general shape of the pressures is similar to one another.

As shown in Figure 47, B100 has the advanced combustion phase, smaller portion of premixed combustion and broader diffusion combustion phase. Since the diffusion combustion phase is ideal for thermal NO condition [48], the larger portion of diffusion combustion can lead to higher NO concentrations.

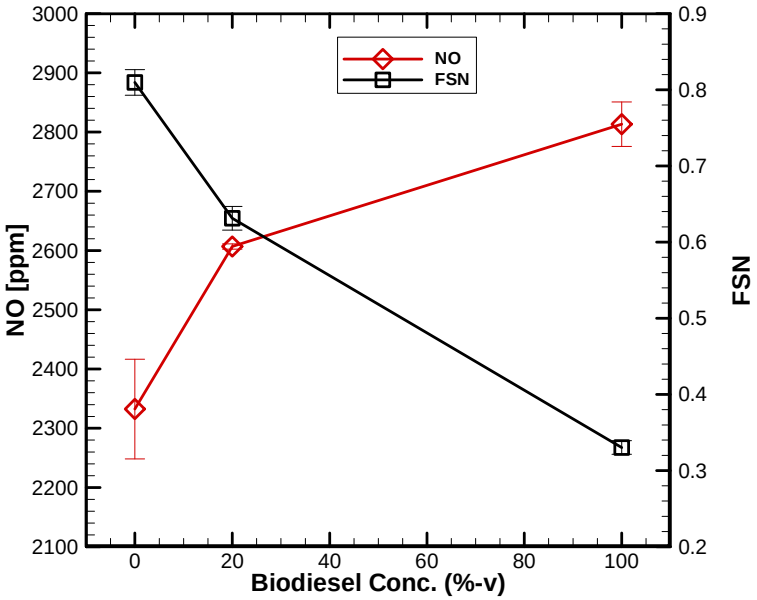

Figure 45 NO and FSN at 1400rev/min and 250 ft-lbs with biodiesel fuels.

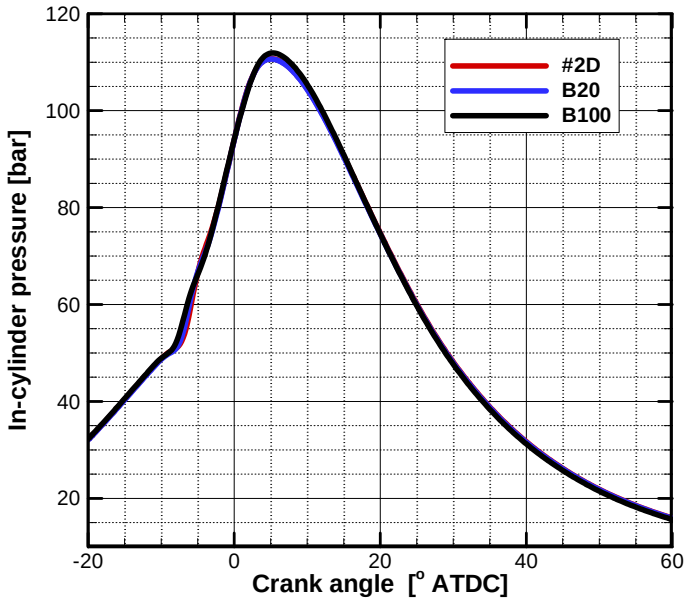

Figure 46 In-cylinder pressure for 1400 rev/min and 250 ft-lbs with biodiesel fuels.

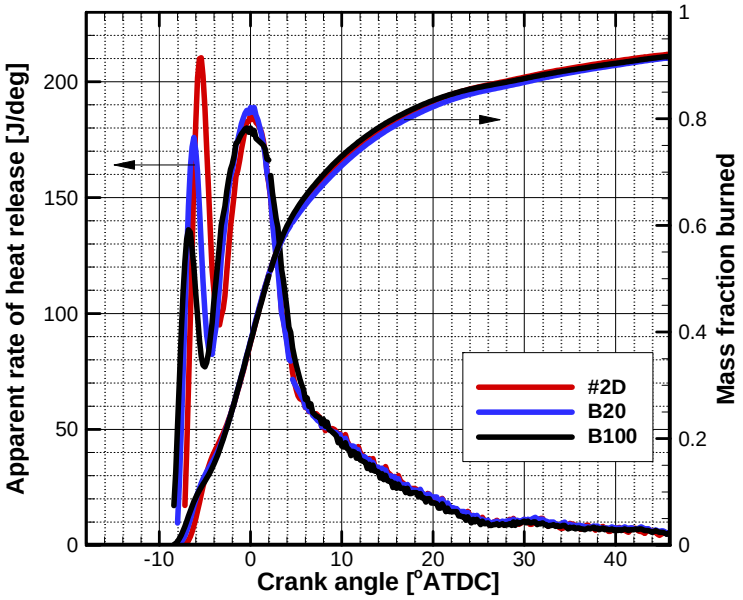

Figure 47 Apparent rate of heat release at 1400 rev/min and 250 ft-lbs with biodiesel fuels.

Figure 48 shows the temperature profiles calculated from the two-stage model. #2D case has the highest temperature profile in the stoichiometric zone, while it has the lowest temperature profile in the lean zone. Even with the highest temperature in the stoichiometric zone, #2D case has the lowest NO concentration. It may mean that the portion of the diffusion combustion is more important factor when the temperature profile is similar.

Unlike the previous cases at 1400 rev/min and 50 ft-lbs, the temperatures in the lean zone are higher than the thermal limit of 1800 K. B20 has the medium temperature, and B100 has the highest temperature profile in the lean zone. Based on the calculated temperature, the NO concentration is estimated by applying the Zeldovich thermal mechanism. Note that the two-stage model is to estimate the final engine-out NO concentration and may not be able to show the physical details of NO concentration during combustion.

As shown in Figure 48, #2D and B20 cases have the higher temperature in the stoichiometric zone than B100. Corresponding to this fact, the overall NO concentrations of the two cases in the stoichiometric zone are higher than B100 case as shown in Figure 48 through Figure 51.Similarly, #2D case has the lowest NO concentration in the lean zone, since it has the lowest temperature as shown in Figure 48.

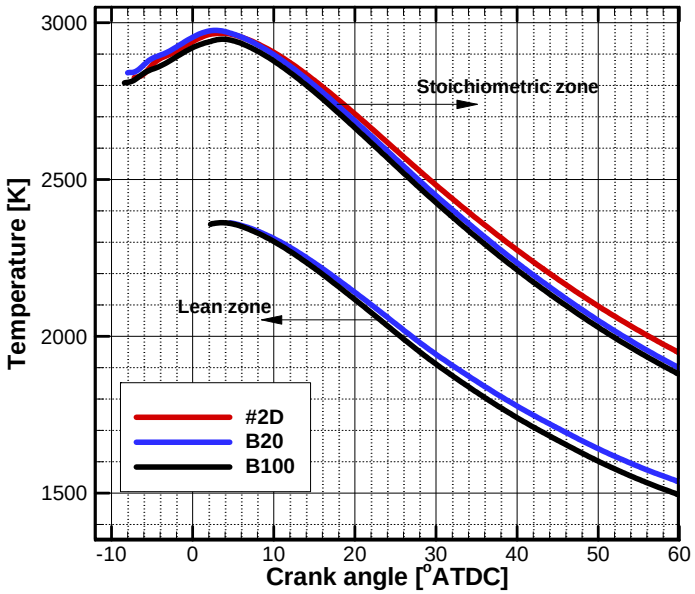

Figure 48 Average temperature calculated from the two-stage model at 1400 rev/min and 250 ft-lbs with biodiesel fuels.

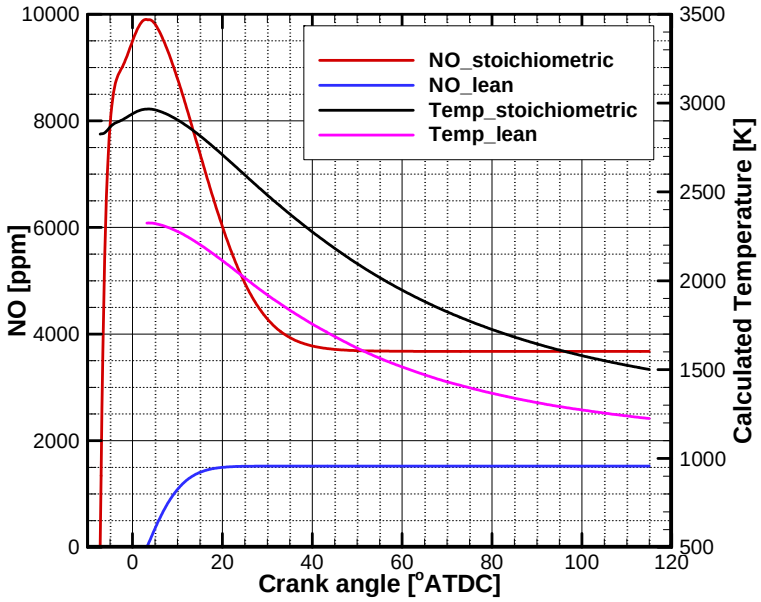

(a)

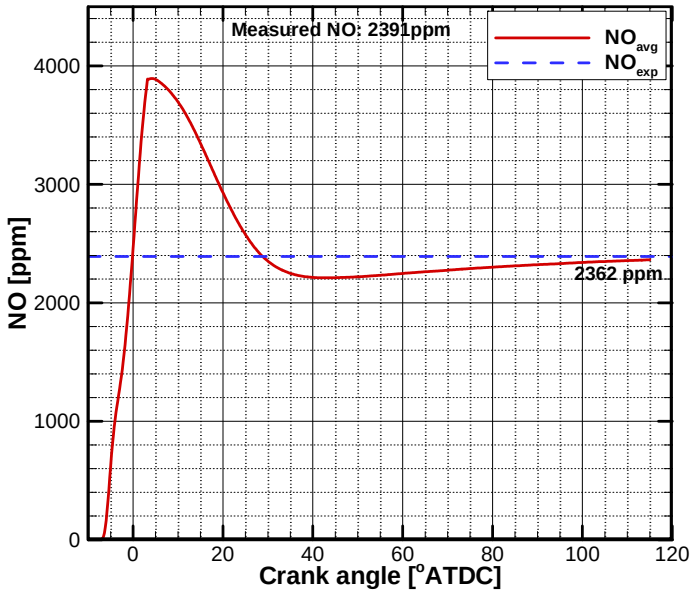

(b)

Figure 49 NO concentration for #2D at 1400 rev/min and 250 ft-lbs: (a) Zonal NO and temperatures, and (b) averaged NO concentration.

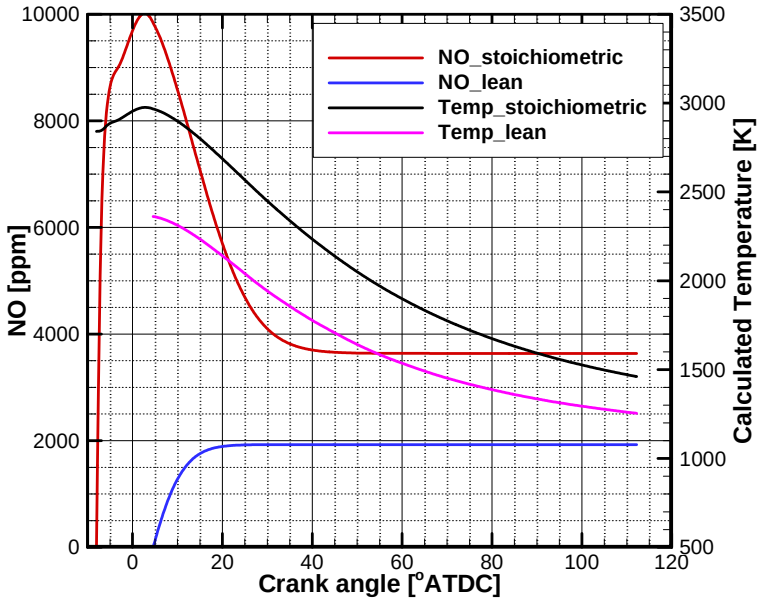

(a)

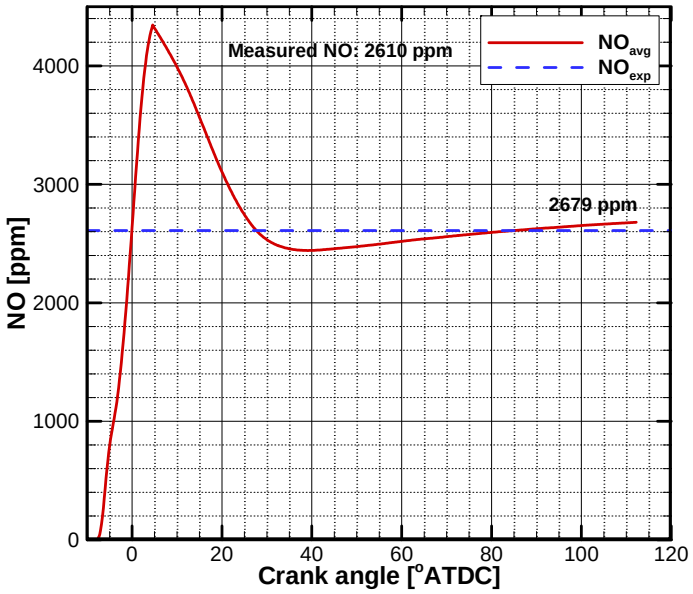

(b)

Figure 50 NO concentration for B20 at 1400 rev/min and 250 ft-lbs: (a) Zonal NO and temperatures, and (b) averaged NO concentration.

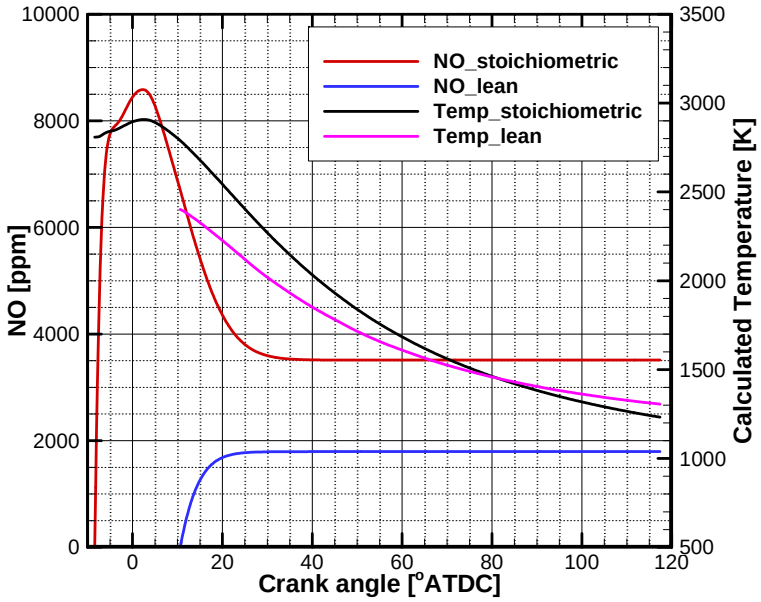

(a)

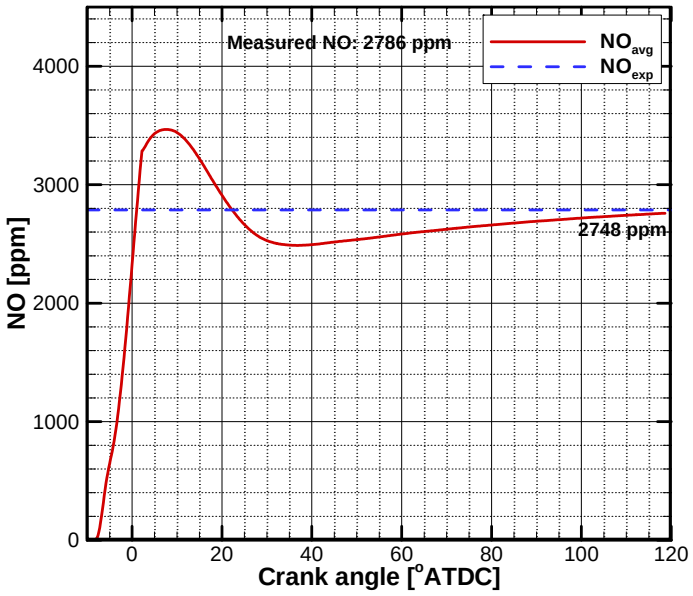

(b)

Figure 51 NO concentration for B100 at 1400 rev/min and 250 ft-lbs: (a) Zonal NO and temperatures, and (b) averaged NO concentration.

Like the previous case, the results at 2400 rev/min and 150 ft-lbs show that NO and FSN have the same trends qualitatively. The higher biodiesel concentration increase NO, but decrease FSN as shown in Figure 52.

The in-cylinder pressures at 2400 rev/min and 150 ft-lbs are shown in Figure 53. As B100 has earlier pressure rise, it has the earliest start of combustion, but slowest reach peak value. In contrast, #2D has the latest start of combustion; however, it has the steepest pressure increase and fastest reaches at the peak value as shown in Figure 53. After the peak values, all the pressures decrease almost identically. According to the pressure rise, B100 case has the most advanced combustion phase and the broadest diffusion combustion phase as shown in Figure 54. Consequently, this case has the smallest portion of the premixed combustion. In contrast to B100 case, #2D case has the biggest portion of premixed combustion phase than other cases, while it has the smallest fraction of diffusion combustion phase. Noting that most thermal NO is formed during diffusion combustion phase, biodiesel fuel can have higher NO concentration since it has higher fraction of diffusion combustion.

Also, the fuel effect of the biodiesel cannot be overlooked, even though it cannot be observed directly from the combustion chamber. Regarding the fuel effects, Mueller et al. [8] explains well about the importance of the equivalence ratio of the mixture in the auto-ignition zone. Biodiesel has the mixture closer to stoichiometric during the auto-ignition due to the fuel bound oxygen. This would lead to higher temperatures, longer residence time at high temperature, and higher thermal NO. Also, Mueller et al. [8] explain that, if the amount of oxygen at the lift-off length is higher, biodiesel has

relatively less soot formation. For these reasons, biodiesel might have higher temperature, less radiation heat loss, and, consequently, higher thermal NO formation. For these reasons, biodiesel blends might have higher NO concentrations relative to conventional diesel.

Figure 55 shows the temperature results. #2D has the higher temperature profile in the stoichiometric zone, while this case has the lower profile in the lean zone. Since the thermal NO is strongly dependent on temperature, #2D has higher peak NO concentration for the stoichiometric zone compared to other cases. Due to the lowest temperature profile in the lean zone, #2D case has the lowest NO profile compared to other cases.

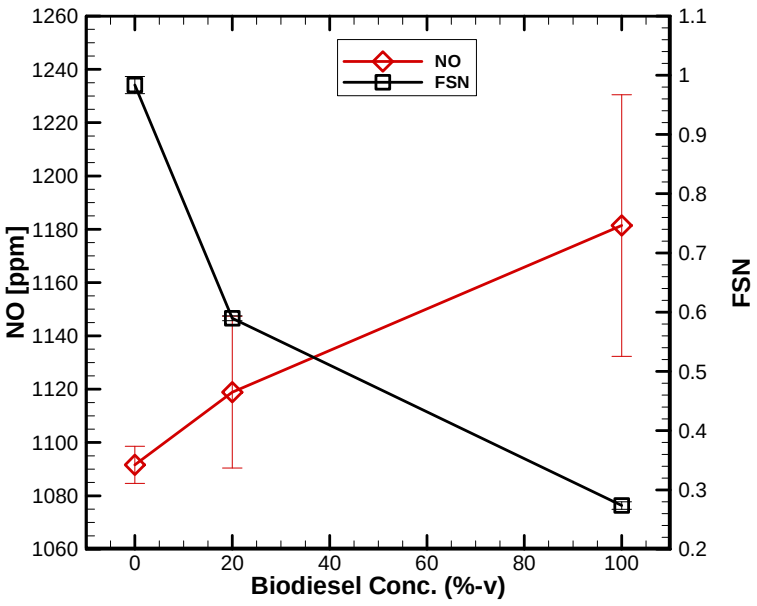

Figure 52 NO and FSN at 2400rev/min and 150 ft-lbs with biodiesel fuels.

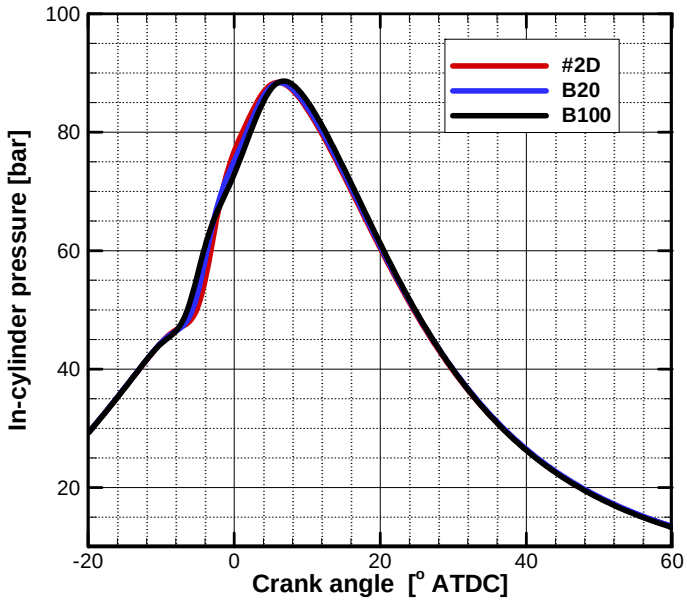

Figure 53 In-cylinder pressure for 2400 rev/min and 150 ft-lbs with biodiesel fuels.

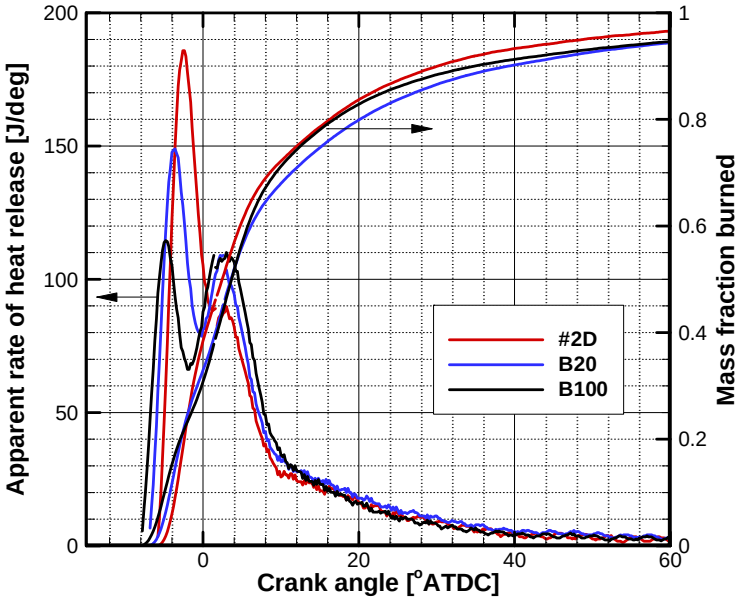

Figure 54 Apparent rate of heat release at 2400 rev/min and 150 ft-lbs with biodiesel fuels.

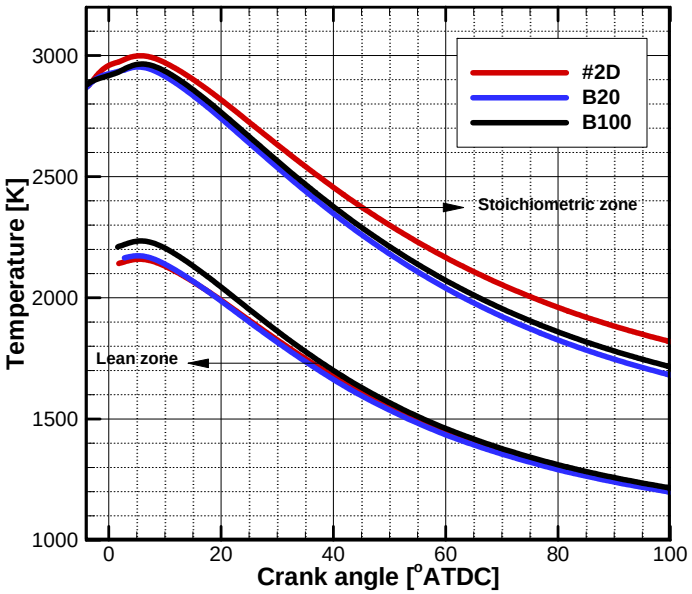

Figure 55 Average temperature for 2400 rev/min and 150 ft-lbs calculated from the two-stage model with biodiesel fuels.

Based on the temperature results, NO concentrations are estimated as shown in Figure 56 through Figure 58. Higher temperature leads to higher NO; the general trend is similar. For example, each case has steep increase in NO at the start of combustion, reaches a peak value, and decreases smoothly to a constant value. The differences between the experimental and calculated NO are less than 100 ppm.

FSN results can be affected by the combustion characteristics and also by the biodiesel fuel effects. Assuming that all the test fuels are identical, the bigger portion of the premixed combustion might cause smaller soot as shown at 50 ft-lbs. In addition to this, the case with smaller portion of the diffusion combustion would have smaller soot concentration since the diffusion phase is the heterogeneous combustion. In this way, #2D case should have the smallest FSN results. However, it cannot be explained only by

the combustion characteristics. Thus, FSN trend could be related to fuel effects of the biodiesel, since the presence of oxygen in the biodiesel tend to reduce soot concentrations [5], [58], [59]. The study by Tree et al. [16] show that 27 to 35 % of fuel oxygen content leads to soot free emission. The reduction in soot caused by the fuel bound oxygen is the results from soot formation and oxidation, since fuel bound oxygen provides more chance to react with carbon and replaces carbon which needs to be burned. Curran et al. [60] explain that carbon bonded to oxygen atoms in the fuel cannot produce soot precursors. Similarly, Cheng et al. [61] show that carbon bonded to oxygen participates less in soot formation. For these reasons, FSN might be affected also by the fuel contents, especially, oxygen in biodiesel combustion.

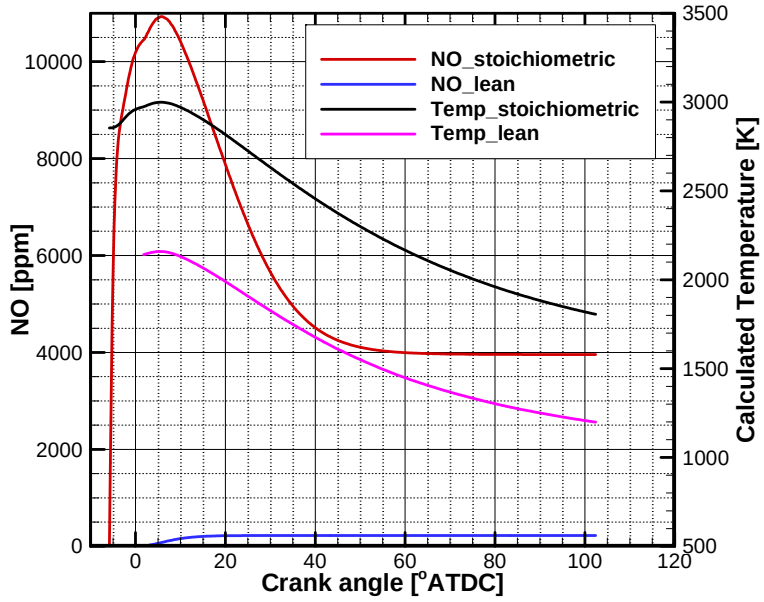

(a)

Figure 56 NO concentration for #2D at 2400 rev/min and 150 ft-lbs: (a) Zonal NO and temperatures, and (b) averaged NO concentration.

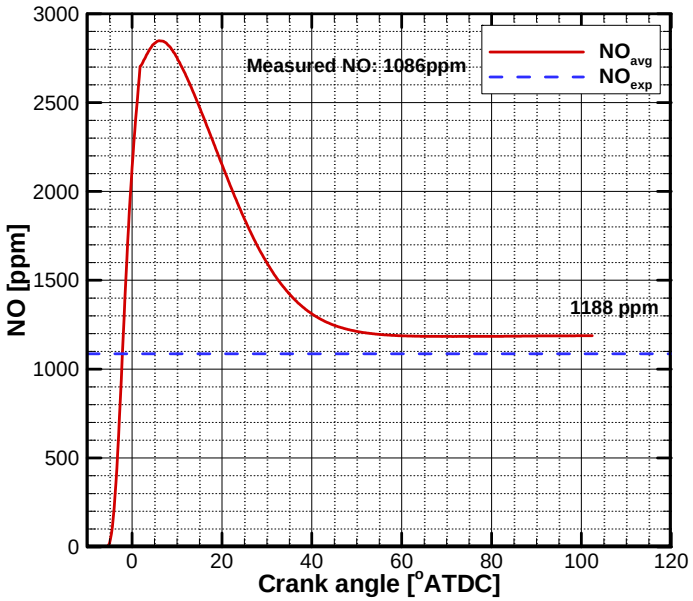

(b)

Figure 56 Continued.

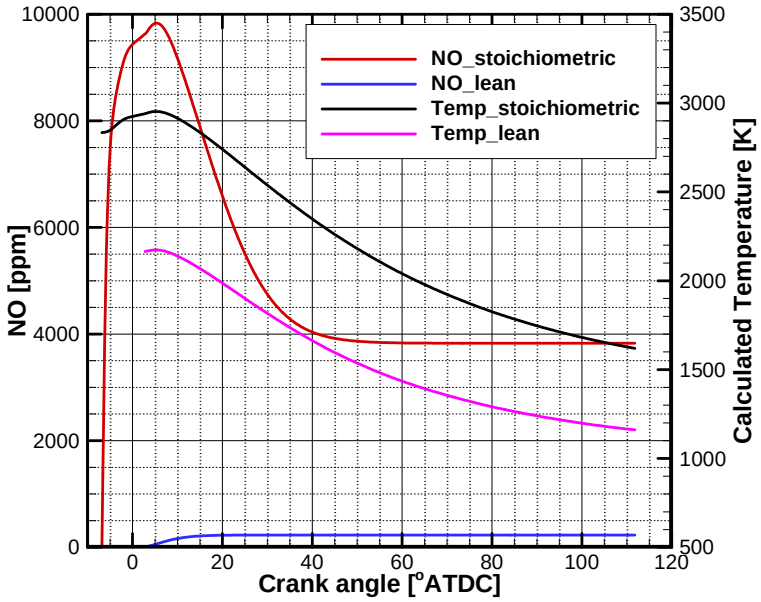

(a)

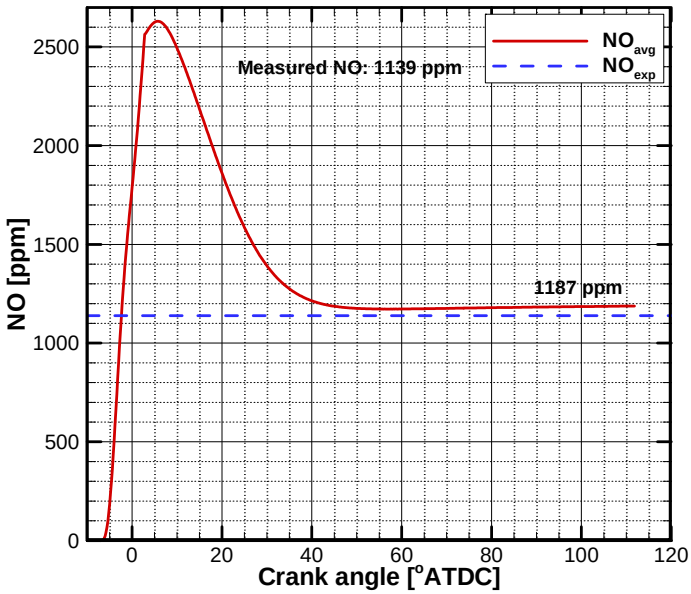

(b)

Figure 57 NO concentration for B20 at 2400 rev/min and 150 ft-lbs: (a) Zonal NO and temperatures, and (b) averaged NO concentration.

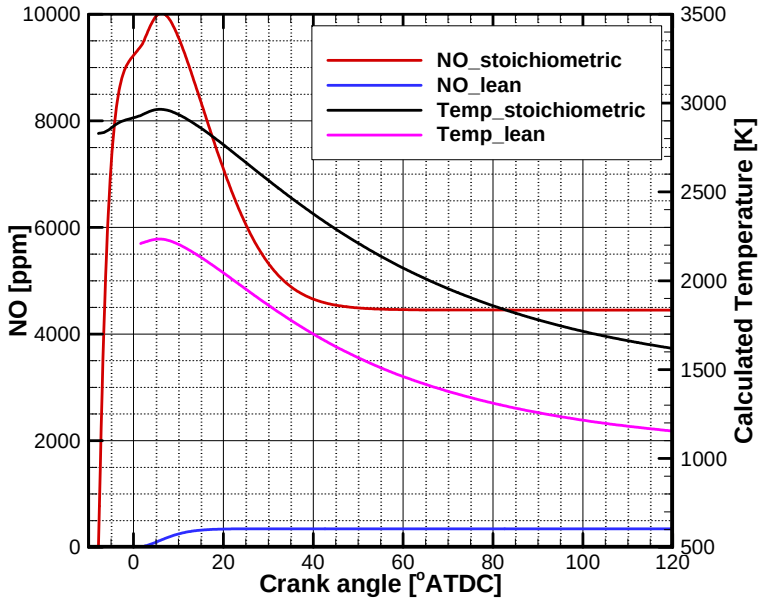

(a)

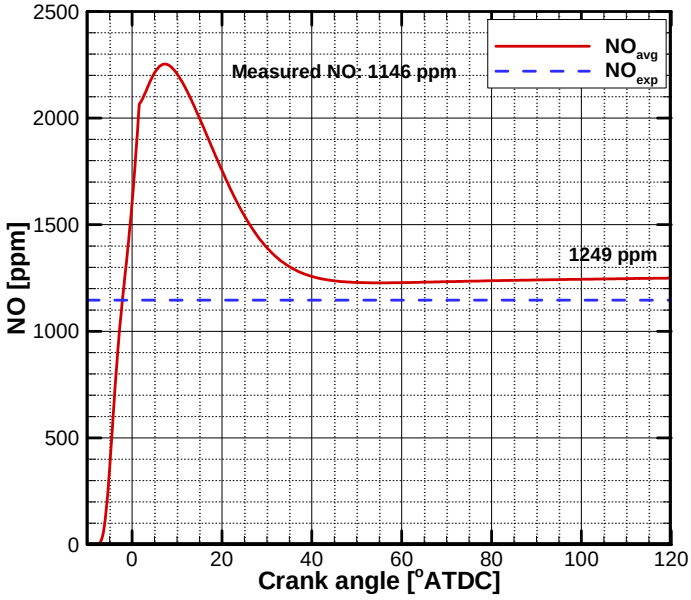

(b)

Figure 58 NO concentration for B100 at 2400 rev/min and 150 ft-lbs: (a) Zonal NO and temperatures, and (b) averaged NO concentration.

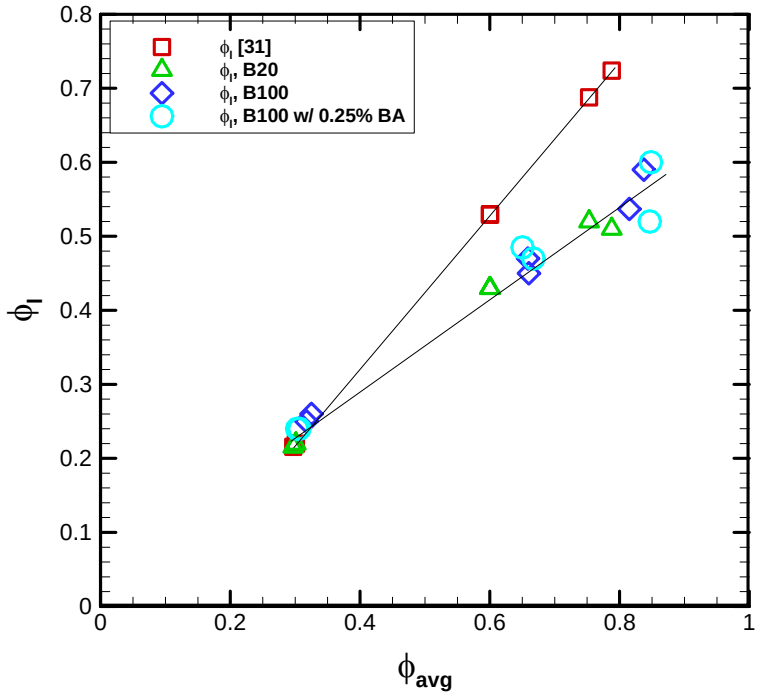

Figure 59 Correlation for the equivalence ration of the lean zone with biodiesel blends.

Like the diesel fuel tests, the correlation for the equivalence ratio of the lean zone is formulated though the NO calculations. All the biodiesel blends have similar equivalence ratios as shown in Figure 59. The common correlation is shown as following:

$$\phi_l = 0.617 \cdot \phi_{\text{avg}} - 0.0507 \qquad 5.1$$

where ϕ_l is the equivalence ratio of the lean zone.

ϕ_{avg} is the averaged equivalence ratio.

The slope of the correlation is lower than that suggested by Szekely et al. [31] as shown in Figure 59. The above correlation is applied to the cases with B100. The

calculation results are shown in Table 13. There are some differences between the measured and calculated NO values, which range up to 21.8 %.

Table 13 Comparison between measured and calculated NO values with the correlation for B100.

Engine condition	Fuel	Measured NO (ppm)	Calculated NO (ppm)	Difference (%)
1400 rev/min & 50ft-lbs	B100	344	371	7.8
1400 rev/min & 250ft-lbs	B100	2786	2402	-13.8
2400 rev/min & 150ft-lbs	B100	1146	1396	21.8

5.3 Soot Emissivity

Soot emissivity calculation is to see if the two-stage model is able to predict changes in soot emissivity. The calculation is based on the analytical model suggested by Morel et al. [43].

Figure 60 shows the rapid increase in emissivity at the start of combustion in each zone. However, the change of emissivity caused by biodiesel concentration and the barium additive (at B100) could not be found. There are small shifts of the emissivity due to the different combustion phase. The calculation results show that the higher load case has a higher peak emissivity in the lean zone. However, the peak emissivity in the stoichiometric zone is above 0.9 for all the fuel cases.

Thus, the emissivity calculation can show the general trend along with the combustion characteristic at each engine load condition, but cannot show the details of soot emissivity that should exist during combustion since the experimental results show

the clear trend with biodiesel and barium additive. In other words,FSN results prove that the calculated emissivity cannot capture the influence of the differences in fuel on soot formation, while the FSN results clearly show the change of soot.

A possible reason is that the analytical model is lack of detailed chemical reactions explaining the combustion, thus the model is not able to explain the details of the soot emissivity.

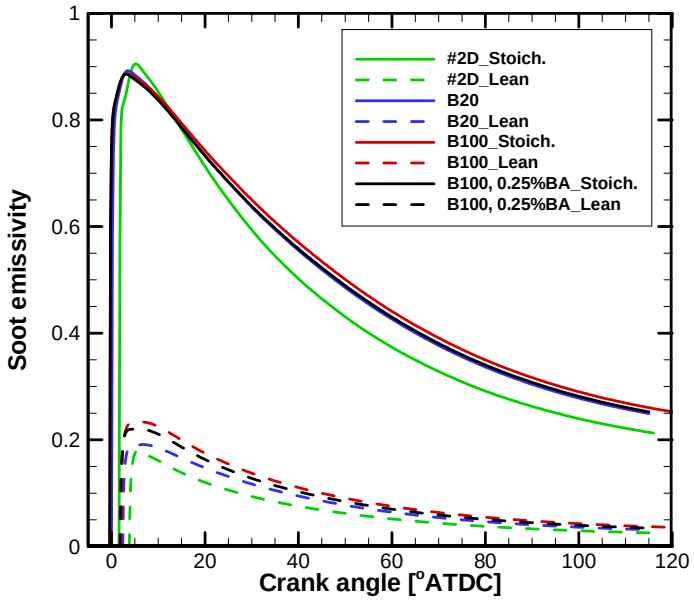

(a)

Figure 60 Soot emissivity results: (a)1400 rev/min and 50 ft-lbs, (b)1400 rev/min and 250 ft-lbs, and (c) 2400 rev/min and 150 ft-lbs with biodiesel fuels.

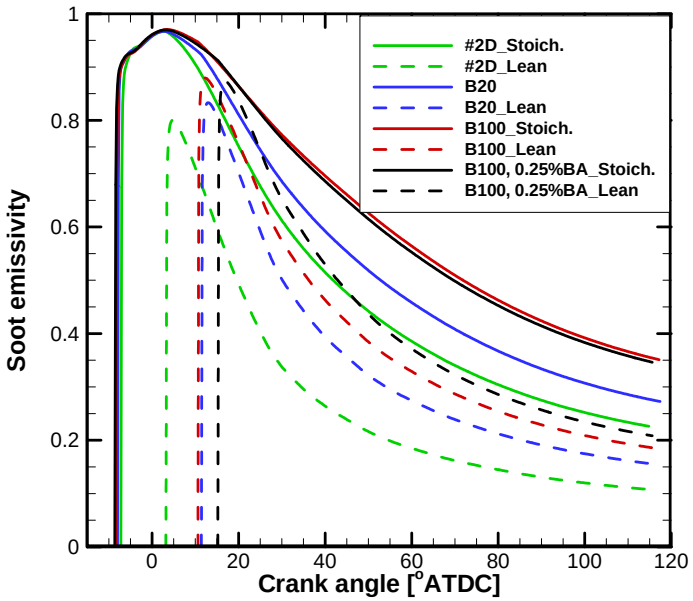

(b)

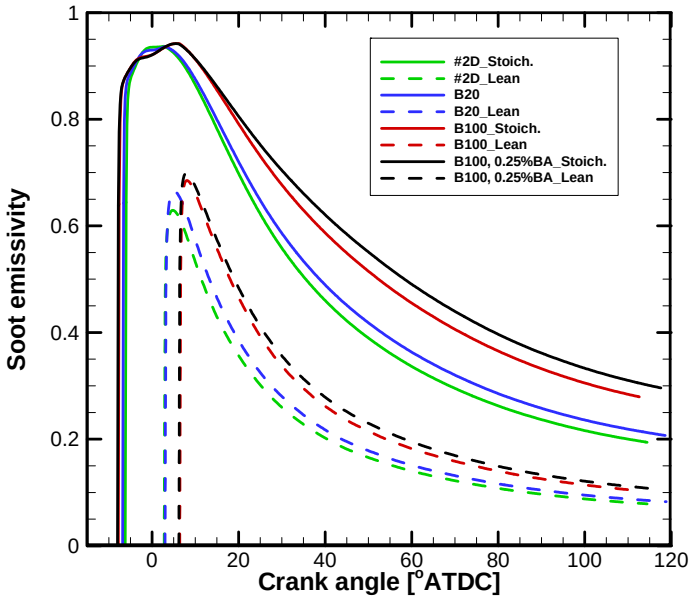

(c)

Figure 60 Continued.

5.4 Discussion

Regarding the effects of the barium additive on NO formation, B100 and 0.25 % BA are used. The results show that FSN is changed clearly by the barium additive, but NO concentration is not changed accordingly. Thus, the barium does not show any noticeable effects on NO formation.

At 1400 rev/min and 50 ft-lbs, the results show that the low engine load condition has different trends of NO and FSN opposite to the general trend with the biodiesel volume concentration. The low load case is defined mainly by the premixed combustion phase. B100 and B20 show earlier ignition indicating that the ignition is advanced with increasing volume concentration of biodiesel. It could be caused mainly by the cetane number since biodiesel has higher cetane number than #2D. The advanced ignition relatively reduces the available time to mix fuel and air before the ignition. Thus, the shorter ignition delay means that the fuel and air mixture are not mixed well enough for as much premixed as is presented in #2D. As the heat release rate profiles show, #2D has higher and broader heat release rate, also higher peak average temperature even with its longer ignition delay. At this condition, most of the fuel is consumed in the premixed combustion. The degree of fuel-air mixing during the ignition delay would be the main factor to decide NO concentration.

Based on the FSN, B100 and B20 cases, which have shorter ignition delay, show higher FSN may be caused by less complete combustion due to the fuel-air mixing. That is the reason why FSN is inversely proportional to the ignition delay.

At 1400 rev/min and 250 ft-lbs, and 2400 rev/min and 150 ft-lbs, NO and FSN follow the general trend with the biodiesel volume percentage. Unlike the previous case at 1400 rev/min and 50 ft-lbs, these are composed of both the premixed and diffusion combustion phases. The NO trend is explained by using the heat release rate results and the fuel effects. When a fuel case has earlier ignition and has a broader heat release profile during the diffusion combustion phase, the case has higher NO concentration. In addition to this, biodiesel has the mixture in the auto-ignition zone and at the lift-off length closer to stoichiometric relative to #2D. These characteristics might lead to higher NO formation.

Regarding FSN results, B100 and B20 cases show lower FSN than #2D case. The presence of fuel bound oxygen in biodiesel blends might be the reason to explain the FSN trend. Biodiesel produces less soot since it has fuel bound oxygen. The less soot may lead to smaller radiative heat losses and, thus, higher flame temperature. However, the detailed change of soot radiation could not be carried out in this study.

Soot radiation is also studied by using the emissivity calculation. The emissivity results could not show the details in emissivity by the biodiesel and also the barium additive, but the emissivity results show the general trend with the change of the load condition.

6 SUMMARY AND CONCLUSIONS

6.1 Summary

In the current study, the two-stage model is programmed based on the work by Szekely et al. [31]. It is used to calculate heat release rate, average temperature, and NO concentration. The two-stage model shows the general profiles of heat release according to the engine speeds and loads and improvements on temperature results. For this reason, Thermal NO modeling could be possible since the temperature is the most important factor to carry out the calculation. Compared to the experimental results, the calculated values show very reasonable estimations, but there are still small differences between experiment and calculation results.

Along with the two-stage model, the engine tests are carried out. The first test is to find the injection timing which has the maximum brake torque at a given condition. At 1400 rev/min and 50 ft-lbs, the injection timing is defined at -10 ^{o} ATDC. The cases at 1400 rev/min and 150 ft-lbs, and 2400 rev/min and 250 ft-lbs, respectively, have the injection timing at -15 ^{o} and -20 ^{o} ATDC.

Based on the defined injection timing, further engine tests are conducted by using #2D with the barium additive, which is known to suppress the soot formation during the combustion. The test results show that the soot concentration is reduced by the barium additive as shown in FSN results. However, the NO concentration is shown not to be affected by soot. Rather, the ambient temperature is a dominant factor to the change of NO. The expected soot change by the barium additive might not have a strong influence on NO formation during combustion.

Other than FSN, the soot emissivity is calculated by using the two-stage model. The calculated emissivity results show the general trends with the engine conditions. However, it could not capture the detailed changes by the barium additive.

To check the possible effects of the barium additive on NO formation, the pure biodiesel, B100, is used with the barium additive since the biodiesel produces smaller amount of soot than #2D. This approach is expected to weaken the soot effect on NO formation and to separate the effects of the additive from the soot. The test results show that the barium additive does not have any direct influence on NO formation.

Using the biodiesel fuel with #2D, the trends of NO and soot concentrations are studied. The results show the different trends at lower and higher load cases. At the lower load case, NO concentration is decreased with increasing the biodiesel volume percentage. #2D shows the later start of combustion, but higher peak of the heat release. Possibly, #2D case has better combustion process, since it shows lower FSN result compared to other biodiesel cases.

At the higher load cases, NO concentration is increased with the biodiesel volume percentage and the diffusion combustion phase. Also, the presence of oxygen in the biodiesel fuels may help the soot oxidation and cause FSN to be decreased.

In order to study the soot radiation, soot emissivity is estimated. The results show the general trend of soot emissivity with the engine load and speed, but cannot capture the detailed changes of soot caused by the barium additive and the biodiesel volume percentage due to the absence of the detailed chemical reactions for combustion processes.

6.2 Conclusions

In this study, the two-stage model is used as an interpreting tool. The two-stage model shows the temperature improvement compared to the single-zone model. It helps the NO model to have the calculated NO values close to the experimental ones. However, the detailed change in NO concentration during combustion could not be verified. Using the two-stage model, the heat release rates are also calculated. All the calculated results are used to interpret the different fuel test results.

In the diesel fuel tests, the soot effects on NO formation are investigated by using the barium additive. The test results show that the change in soot does not affect NO formation noticeably. Rather, the ambient temperature shows the dominant effect on the NO formation for this study.

In the biodiesel tests, the effects of the barium additive on NO are studied. The results show that the barium additive does not have any direct effects on NO formation. Also, it is shown that the presence of oxygen in biodiesel fuel reduces the soot concentration and increases NO concentration at the higher load cases where both the premixed and diffusion combustion phases are observed. Also, wider diffusion combustion phase causes higher NO concentration. However, at the low load condition, the biodiesel case shows higher soot and lower NO concentration compared to #2D case due to the combustion characteristics.

Using the two-stage model, the soot emissivity is estimated for both the diesel and biodiesel tests. The results show the general trends of the soot emissivity according to

the engine speeds and loads. However, the detailed changes in soot concentration cannot be observed due to the lack of the combustion modeling.

Through this study, the relationship between soot and NO is verified. This understanding can be applied to develop strategies to remove soot and NO at the same time. Since their trade-off relation is not dominant, controlling both of them is thought to be possible. These findings can be used to decrease NO concentration in biodiesel combustion.

Also, the two-stage model is expected to be used in an engine control loop for NO monitoring, since it shows results reasonably close to the experimental values. Also, the model is able to estimate NO concentration within a short time properly to the engine speed. For this soot emissivity, it needs more efforts to find or develop a soot emissivity model.

Lastly, this engine research is hoped to be the basis in emission research, engine control research, and biodiesel research.

6.3 Future Study

Through this study, the relationship between NO and soot is investigated. The well-known trade-off relation is not observed in this study, but the ambient air temperature, premixed and diffusion phases (combustion characteristics), presence of oxygen (fuel effect) are found to be more dominant than the expected effect of soot.

There are several things to recommend for the extended work of this research:

1. The ambient condition is observed to affect NO formation more than the attempted controlled change (i.e., in-cylinder soot formation via the use of barium additive). In order to find out possible factors, which might be hidden by the effect of the ambient condition, further research needs to be conducted with a control system for the ambient conditions.
2. The analytical model is not able to explain the detailed change of soot emissivity. In order to overcome this problem, the direct observation inside the cylinder is desirable to study the change of the soot during the combustion by the barium additive.
3. As the analytical model is able to reasonably estimate the NO concentration, a NO control program with the two-stage model may be an interesting research.

REFERENCES

[1] Heywood, J. B., 1988, *Internal Combustion Engine Fundamentals*, McGraw-Hill, Inc., New York.

[2] Graboski, M. S., and McCormick, R. L., 1998, "Combustion of fat and vegetable oil derived fuels in diesel engines," Progress in Energy and Combustion Science, 24(2), pp. 125-164.

[3] Cheng, A. S., Upatnieks, A., and Mueller , C. J., 2006, "Investigation of the impact of biodiesel fuelling on NOx emissions using an optical direct injection diesel engine," International Journal of Engine Research, 7(4), pp. 297-318.

[4] Musculus, M. P. B., 2005, "Measurements of the Influence of Soot Radiation on In-Cylinder Temperatures and Exhaust NOx in a Heavy-Duty DI Diesel Engine," SAE World CongressDetroit, Michigan, SAE Paper No. 2005- 2001 -0925.

[5] Choi, C., Bower, G., and Reitz, R., 1997, "Effects of biodiesel blended fuels and multiple injections on DI diesel engines," SAE Transactions, 106, SAE Paper No. 970218

[6] Ra, Y., Reitz, R., McFarlane, J., and Daw, C. S., 2007, "Effects of fuel physical properties on diesel engine combustion using diesel and bio-diesel fuels," Oak Ridge National Laboratory (ORNL); Fuels, Engines and Emissions Research Center.

[7] Annamalai, K., and Puri, I. K., 2007, *Combustion Science and Engineering*, CRC Press/Taylor & Francis, Boca Raton.

[8] Mueller, C. J., Boehman, A. L., and Martin, G. C., 2009, "An experimental investigation of the origin of increased NO_x emissions when fueling a heavy-duty compression-ignition engine with soy biodiesel," SAE International Journal of Fuels and Lubricants, 2, SAE Paper No. 2009-2001-1792.

[9] Zhang, Y., and Boehman, A. L., 2007, "Impact of Biodiesel on NOx Emissions in a Common Rail Direct Injection Diesel Engine," Energy Fuels, 21 (4), pp. 2003–2012.

[10] Canakci, M., 2007, "Combustion characteristics of a turbocharged DI compression ignition engine fueled with petroleum diesel fuels and biodiesel," Bioresource Technology, 98(6), pp. 1167-1175.

[11] Bowman, C. T., 1975, "Kinetics of pollutant formation and destruction in combustion," Progress in Energy and Combustion Science, 1(1), pp. 33-45.

[12] Fenimore, C., 1971, "Formation of nitric oxide in premixed hydrocarbon flames," Symposium (International) on Combustion, 13, pp. 373-380.

[13] Lavoie, G., Heywood, J., and Keck, J., 1970, "Experimental and theoretical study of nitric oxide formation in internal combustion engines," Combustion Science and Technology, 1(4), pp. 313-326.

[14] Caton, J. A., 2002, "Detailed results for nitric oxide emissions as determined from a multiple-zone cycle simulation for a spark-ignition engine," ASME 2002 Internal Combustion Engine Division Fall Technical Conference New Orleans, Louisiana, ICEF 2002-2491.

[15] Turns, S. R., 1995, *An Introduction to Combustion: Concepts and Applications*, McGraw-Hill, Inc, New York.

[16] Tree, D. R., and Svensson, K. I., 2007, "Soot processes in compression ignition engines," Progress in Energy and Combustion Science, 33(3), pp. 272-309.

[17] Smith, O. I., 1981, "Fundamentals of soot formation in flames with application to diesel engine particulate emissions," Progress in Energy and Combustion science, 7(4), pp. 275-291.

[18] Müller, J. O., Su, D. S., Jentoft, R. E., Wild, U., and Schlögl, R., 2006, "Diesel engine exhaust emission: Oxidative behavior and microstructure of black smoke soot particulate," Environmental Science & Technology, 40(4), pp. 1231-1236.

[19] McClellan, R. O., 1987, "Health effects of exposure to diesel exhaust particles," Annual review of Pharmacology and Toxicology, 27(1), pp. 279-300.

[20] Haynes, B., and Wagner, H. G., 1981, "Soot formation," Progress in Energy and Combustion Science, 7(4), pp. 229-273.

[21] Bartok, W., and Sarofim, A. F., 1991, *Fossil Fuel Combustion*, John Wiley and Sons Inc., New York.

[22] Borman, G., and Nishiwaki, K., 1987, "Internal-combustion engine heat transfer," Progress in energy and combustion science, 13(1), pp. 1-46.

[23] Cotton, D., Friswell, N., and Jenkins, D., 1971, "The suppression of soot emission from flames by metal additives," Combustion and Flame, 17(1), pp. 87-98.

[24] Bulewicz, E., Evans, D., and Padley, P., 1975, "Effect of metallic additives on soot formation processes in flames," Symposium (International) on Combustion, 15(1), pp. 1461-1470.

[25] Norman, G. R., 1965, "A New Approach to Diesel Smoke Suppression," National Fuels and Lubricants and Transportation Meetings, SAE International, Houston, Texas, SAE Paper No. 660339.

[26] Truex, T. J., Pierson, W. R., McKee, D. E., Shelef, M., and Baker, R. E., 1980, "Effects of barium fuel additive and fuel sulfur level on diesel particulate emissions," Environmental Science & Technology, 14(9), pp. 1121-1124.

[27] Draper, W. M., Phillips, J., and Zeller, H. W., 1988, "Impact of a barium fuel additive on the mutagenicity and polycyclic aromatic hydrocarbon content of diesel exhaust particulate emissions," SAE International Fall Fuels and Lubricants Meeting and Exhibition, SAE International, Portland, Oregon, SAE Paper No. 881651.

[28] Haynes, B., Jander, H., and Wagner, H., 1979, "The effect of metal additives on the formation of soot in premixed flames," Symposium (international) on Combustion, 17, pp. 1365-1374.

[29] Foster, D. E., 1985, "An overview of zero-dimensional thermodynamic models for IC engine data analysis," SAE International Fall Fuels and Lubricants Meeting and ExhibitionTulsa, Oklahoma, SAE Paper No. 852070.

[30] Krieger, R. B., and Borman, G. L., 1966, "Computation of apparent heat release for internal combustion engines," ASME Paper No. 66-WA/DGP-64.

[31] Szekely, G. A. J. A., A. C. , 1987, "A Two-Stage Heat-Release Model for Diesel Engines," SAE Technical Paper, SAE Paper No. 861272.

[32] Stull, D. R., and Prophet, H., 1971, *JANAF Thermochemical Tables*, Dow Chemical Company: Midland.

[33] Ishida, M., Ueki, H., Matsumura, N., Yamaguchi, M., and Luo, G. F., 1996, "Diesel Combustion Analysis Based on Two-Zone Model: Comparison between Model Analysis and Experiment," JSME international journal. Ser. B, Fluids and thermal engineering, 39(1), pp. 185-192.

[34] Kamimoto, T., Minagawa, T., and Kobori, S., 1997, "A two-zone model analysis of heat release rate in diesel engines," SAE International Combustion & Emissions Formation Processes in Diesel EnginesTulsa, Oklahoma, SAE Paper No. 972959

[35] Guezennec, Y. G., and Hamama, W., 1999, "Two-Zone Heat Release Analysis of Combustion Data and Calibration of Heat Transfer Correlation in An I. C. Engine," SAE International Congress & ExpositionDetroit, Michigan, SAE Paper No. 1999-1901-0218.

[36] Sitkei, G., and Sz ke, P., 1974, Heat Transfer and Thermal Loading in Internal Combustion Engines, Akadémiai Kiadó, Budapest.

[37] Kunitomo, T., Matsuoka, K., and Oguri, T., 1975, "Prediction of radiative heat flux in a diesel engine," SAE International Off-Highway and Powerplant Congress and Exposition, SAE International, Milwaukee, Wisconsin, SAE Paper No. 750786.

[38] Olikara, C., and Borman, G. L., 1975, "A computer program for calculating properties of equilibrium combustion products with some applications to I.C. engines," Automotive Engineering Congress and ExpositionDetroit, Michigan, SAE Paper No. 750468.

[39] Morris, C., and Dent, J., 1976, "The simulation of air fuel mixing in high swirl open chamber diesel engines," ARCHIVE: Proceedings of the Institution of Mechanical Engineers 1847-1982 (vols 1-196), 190(1976), pp. 503-513.

[40] Ahmad, T., and Plee, S. L., 1983, "Application of flame temperature correlations to emissions from a direct-injection diesel engine," SAE Paper No. 831734

[41] Woschni, G., 1967, "A universally applicable equation for the instantaneous heat transfer coefficient in the internal combustion engine.," SAE Transactions, SAE Paper No. 670931.

[42] Hohenberg, G. F., "Advanced approaches for heat transfer calculations," Proc. SAE Transaction Warrendale, Pennsylvania, SAE Paper No. 790825.

[43] Morel, T., and Keribar, R., 1986, "Heat radiation in DI diesel engines," SAE Technical Paper, SAE Paper No. 860445.

[44] Gardiner, W. C., 2000, *Gas-phase Combustion Chemistry*, Springer Verlag, New York.

[45] Theobald, M. A., and Alkidas, A. C., 1987, "On the Heat-Release Analysis of Diesel Engines: Effects of Filtering of Pressure Data," SAE International Fall Fuels and Lubricants Meeting and Exhibition, SAE International, Toronto, Ontario, Canada, SAE Paper No. 872059.

[46] Sastry, G., and Chandra, H., 1994, "A Three-Zone Heat Release Model for DI Diesel Engines," International Congress & Exposition, SAE International, Detroit, MI, SAE Paper No. 940671

[47] Lyn, W. T., 1962, "Study of burning rate and nature of combustion in diesel engines," Symposium (International) on Combustion, 9(1), pp. 1069 - 1082.

[48] Dec, J. E., 1997, "A conceptual model of DI diesel combustion based on laser-sheet imaging," SAE Transactions, 106, SAE Paper No. 970873.

[49] Alkidas, A. C., 1984, "Relationships between smoke measurements and particulate measurements," SAE Transactions, SAE paper No. 840412.

[50] Christian, V. R., Knopf, F., Jaschek, A., and Schindler, W., 1993, "Eine neue Meßmethodik der Bosch-Zahl mit erhöhter Empfindlichkeit," MTZ Motortechnische Zeitschrift, 54, pp. 16-22.

[51] Miller, C., 1967, "Diesel smoke suppression by fuel additive treatment," SAE Technical Paper, SAE Paper No. 670093.

[52] Wahiduzzaman, S., Morel, T., Timar, J., and Dewitt, D., 1987, "Experimental and analytical study of heat radiation in a diesel engine," SAE transactions, 96(4), pp. 583-599.

[53] Qiong, W., Pinwen, J., and Jianhua, L., 1998, "Comparison of a radiation model with experiment in a diesel engine," SAE International Spring Fuels and Lubricants Meeting and Exposition Dearborn, Michigan, SAE Paper No. 981452.

[54] McCormick, R., Graboski, M., Alvarez, J., Tyson, K., and Vertin, K., 2002, "Fuel additive and blending approaches to reducing NOx emissions from biodiesel," SAE International, SAE Paper No. 2002-2001-1658.

[55] Vaughn, T., Hammill, M., Harris, M., and Marchese, A. J., 2006, "Ignition delay of bio-ester fuel droplets," SAE Technical Paper, SAE Paper No. 2006-2001-2330.

[56] Akasaka, Y., Suzuki, T., and Sakurai, Y., 1997, "Exhaust emissions of a DI diesel engine fueled with blends of biodiesel and low sulfur diesel fuel," SAE International, SAE Paper No. 1997-10-01.

[57] Szybist, J. P., Kirby, S. R., and Boehman, A. L., 2005, "NOx emissions of alternative diesel fuels: a comparative analysis of biodiesel and FT diesel," Energy & Fuels, 19(4), pp. 1484-1492.

[58] Schmidt, K., and Van Gerpen, J., 1996, "The effect of biodiesel fuel composition on diesel combustion and emissions," SAE Technical Paper, SAE Paper No. 961086.

[59] Szybist, J. P., Song, J., Alam, M., and Boehman, A. L., 2007, "Biodiesel combustion, emissions and emission control," Fuel Processing Technology, 88(7), pp. 679-691.

[60] Curran, H. J., Fisher, E. M., Glaude, P.-A., Marinov, N. M., Pitz, W. J., Westbrook, C. K., Layton, D. W., Flynn, P. F., Durrett, R. P., Loye, A. O. z., Akinyemi, O. C., and Dryer, F. L., 2001, "Detailed chemical kinetic modeling of diesel combustion with oxygenated fuels," SAE 2001 World Congress, SAE Paper No. 2001-01-0653 .

[61] Cheng, A., Dibble, R. W., and Buchholz, B. A., 2002, "The effect of oxygenates on diesel engine particulate matter," SAE Technical Paper, SAE 2002-2001-1705.

APPENDIX A

This section shows how to calculate the thermodynamic properties such as enthalpy, internal energy, and ideal gas constant, also their partial derivative with respect to temperature, pressure, and equivalence ratio. This appendix is nothing more than a summary of the work done by Olikara et al. [38] .

Since their approach is introduced to compute the thermodynamic properties using a minimal number of critical equations, many researchers have used the idea for various combustion efforts. The predominant thought is that the gas mixture in a cylinder is in an equilibrium state at any instant, and that combustion proceeds with air and hydrocarbon fuel which contains C, H, O, and N atoms.

One simple example can explain this approach easily step by step. The combustion with a fuel, $C_nH_mO_lN_k$, and air at equivalence ratio, ϕ, takes place and the products stays in an equilibrium state. The chemical reaction equation is expressed as:

$$x_{13}\left[C_nH_mO_lN_k+\frac{n+m/4-l/2}{\phi}\{O_2+3.7224N_2+0.044Ar\}\right]\rightarrow x_1H+x_2O+x_3N+x_4H_2+x_5OH+x_6CO+x_7NO+x_8O_2+x_9H_2O+x_{10}CO_2+x_{11}N_2+x_{12}Ar \quad \text{A 1}$$

x_1 through x_{12} are the mole fractions of the product species, and x_{13} is mole of a fuel which gives one mole of the summation of the products in combustion. It means that the summation of x_1 through x_{12} is the value of one mole as:

$$\sum_{i=1}^{12} x_i = 1$$

The left hand side of the above equation can be simplified in terms of the atoms as:

$$x_{13}\left[nC + mH + rO_2 + r'N_2 + r''Ar\right]$$

where $r_O = \left(n + \frac{m}{4} - \frac{1}{2}\right) / \phi$

$$r = \frac{1}{2} + r_0$$

$$r' = \frac{r}{2} + 3.7374 \cdot r_0$$

$$r'' = 0.0444 \cdot r_0$$

In atom balance:

C: $x_6 + x_{10} = nx_{13}$

H: $x_1 + 2x_4 + x_5 + 2x_9 = mx_{13}$

O: $x_2 + x_5 + x_6 + x_7 + 2x_8 + x_9 + 2x_{10} = 2rx_{13}$

N: $x_3 + x_7 + 2x_{11} = 2r'x_{13}$

Ar: $x_{12} = r''x_{13}$

In spite of combustion proceeding in a non-equilibrium fashion, some species are believed to exist in equilibrium concentrations. With this assumption, Olikara et al. [38] suggested that the equilibrium among the products can be expressed by the following 7 non-redundant hypothetical reactions shown in Table A 1 The reference pressure is at 1.0 atmosphere (atm).

Table A 1. 7 non-redundant hypothetical reactions

Reaction	Equilibrium constant
$\frac{1}{2}H_2 \leftrightarrow H$	$K_1 = \frac{x_1 p^{1/2}}{x_4^{1/2}}$
$\frac{1}{2}O_2 \leftrightarrow O$	$K_2 = \frac{x_2 p^{1/2}}{x_8^{1/2}}$
$\frac{1}{2}N_2 \leftrightarrow N$	$K_3 = \frac{x_3 p^{1/2}}{x_{11}^{1/2}}$
$\frac{1}{2}H_2 + \frac{1}{2}O_2 \leftrightarrow OH$	$K_5 = \frac{x_5}{x_4^{1/2} x_8^{1/2}}$
$\frac{1}{2}O_2 + \frac{1}{2}N_2 \leftrightarrow NO$	$K_7 = \frac{x_7}{x_8^{1/2} x_{11}^{1/2}}$
$H_2 + \frac{1}{2}O_2 \leftrightarrow H_2O$	$K_9 = \frac{x_9}{x_4 x_8^{1/2} p^{1/2}}$
$CO + \frac{1}{2}O_2 \leftrightarrow CO_2$	$K_{10} = \frac{x_{10}}{x_6 x_8^{1/2} p^{1/2}}$

where pressure, *p*, is in units of atm.

By using x_4, x_6, x_8 and x_{12}, other mole fractions of products can be rearranged as following:

$$x_1 = C_1 x_4^{1/2} \qquad C_1 = \frac{K_1}{P^{1/2}}$$

$$x_2 = C_2 x_8^{1/2} \qquad C_2 = \frac{K_2}{P^{1/2}}$$

$$x_3 = C_3 x_{11}^{1/2} \qquad C_3 = \frac{K_3}{P^{1/2}}$$

$$x_5 = C_5 x_4^{1/2} x_8^{1/2} \qquad C_5 = K_5$$

$$x_7 = C_7 x_8^{1/2} x_{11}^{1/2} \qquad C_7 = K_7$$

$$x_9 = C_9 x_4 x_8^{1/2} \qquad C_9 = K_9 P^{1/2}$$

$$x_{10} = C_{10} x_6 x_8^{1/2} \qquad\qquad C_{10} = K_{10} P^{1/2}$$

A.1. The independent mole fractions of products: x_4, x_6, x_8 and x_{11}

Recall and rewrite the balance of atoms:

$$x_1 + 2x_4 + x_5 - 2x_9 - \frac{m}{n}(x_6 + x_{10}) = 0$$

$$x_2 + x_5 + x_6 + x_7 + 2x_8 + x_9 + 2x_{10} - \frac{2r}{n}(x_6 + x_{10}) = 0$$

$$x_3 + x_7 + 2x_{11} - \frac{2r'}{n}(x_6 + x_{10}) = 0$$

By using the equations above, the summation of moles of products can be expressed as:

$$\sum_{i=1}^{12} x_i = 1 \qquad \rightarrow \qquad \sum_{i=1}^{11} x_i + \frac{r''}{n}\left(x_6 + x_{10}\right) - 1 = 0$$

For simplification, define the symbols as

$$\frac{m}{n} = d_1, \qquad \frac{2r}{n} = d_2$$

$$\frac{2r'}{n} = d_3, \qquad \frac{r''}{n} = d_4$$

Let's assign pseudo function for each equation as followings:

$$\mathrm{f}_1 = \mathrm{c}_1 \mathrm{x}_4^{1/2} + 2\mathrm{x}_4 + c_5 \mathrm{x}_4^{1/2} \mathrm{x}_8^{1/2} + 2c_9 \mathrm{x}_4 \mathrm{x}_8^{1/2} - \frac{\mathrm{m}}{\mathrm{n}}\left(\mathrm{x}_6 + c_{10} \mathrm{x}_6 \mathrm{x}_8^{1/2}\right)$$

$$\mathrm{f}_2 = \mathrm{c}_2 \mathrm{x}_8^{1/2} + c_5 \mathrm{x}_4^{1/2} \mathrm{x}_8^{1/2} + \mathrm{x}_6 + c_7 \mathrm{x}_8^{1/2} \mathrm{x}_{11}^{1/2} + 2\mathrm{x}_8 + c_9 \mathrm{x}_4 \mathrm{x}_8^{1/2} - \frac{2\mathrm{r}}{\mathrm{n}}\left(\mathrm{x}_6 + c_{10} \mathrm{x}_6 \mathrm{x}_8^{1/2}\right)$$

$$\mathrm{f}_3 = \mathrm{c}_3 \mathrm{x}_{11}^{1/2} + c_7 \mathrm{x}_8^{1/2} \mathrm{x}_{11}^{1/2} + \mathrm{x}_{11} - \frac{2\mathrm{r}'}{\mathrm{n}}\left(\mathrm{x}_6 + c_{10} \mathrm{x}_6 \mathrm{x}_8^{1/2}\right)$$

$$f_4 = C_1 x_4^{\frac{1}{2}} + C_2 x_8^{\frac{1}{2}} + C_3 x_{11}^{\frac{1}{2}} + x_4 + C_5 x_4^{\frac{1}{2}} x_8^{\frac{1}{2}} + x_6 + C_7 x_8^{\frac{1}{2}} x_{11}^{\frac{1}{2}} + 2x_8 + C_9 x_4 x_8^{1/2} + C_{10} x_6 x_8^{1/2} + x_{11} + \frac{r}{n}\left(x_6 + C_{10} x_6 x_8^{1/2}\right) - 1$$

$$f_4 = c_1 x_4^{\frac{1}{2}} + c_2 x_8^{\frac{1}{2}} + c_3 x_{11}^{\frac{1}{2}} + x_4 + c_5 x_4^{\frac{1}{2}} x_8^{\frac{1}{2}} + x_6 + c_7 x_8^{\frac{1}{2}} x_{11}^{\frac{1}{2}} + 2x_8 + c_9 x_4 x_8^{1/2} + c_{10} x_6 x_8^{1/2} + x_{11} + \frac{r''}{n}\left(x_6 + c_{10} x_6 x_8^{1/2}\right) - 1$$

Since there are four equations (f_1, f_2, $f_3 f_3$ and $f_4 f_4$) and four unknowns (x_4, $x_6 x_6$, x_8 x_8 and $x_{11} x_{12}$), it is easy to calculate the four unknowns by using the Newton-Rhapson method:

$$f_j + \frac{\partial f_j}{\partial x_4}\Delta x_4 + \frac{\partial f_j}{\partial x_6}\Delta x_6 + \frac{\partial f_j}{\partial x_8}\Delta x_8 + \frac{\partial f_j}{\partial x_{11}}\Delta x_{11} \approx 0 \quad \rightarrow \quad \text{j=1, 2, 3, 4}$$

The four equations needs to be solved to find Δx_4, $\Delta x_6 x_6$, $\Delta x_8 x_8$ and Δx_{11}. Then, the previous value can be improved as:

$$x_i^{(2)} = x_i^{(1)} + \Delta x_i \; x_i^{(2)} = x_i^{(1)} + \Delta x_i \qquad \text{i=4, 6, 8 and 11}$$

Before solving the above equations, initial guesses should be estimated. Those guess values are the following:

For $\phi \le 1.0$, $x_{13} = \dfrac{1}{\frac{m}{4} + r + r' + r''}\, x_{13} = \frac{1}{\frac{m}{4} + r + r' + r''}$

For $\phi > 1.0$, $x_{13} = \dfrac{1}{n + \frac{m}{2} + r' + r''}\, x_{13} = \frac{1}{n + \frac{m}{2} + r' + r''}$

Then substituting x_{13} into the following equation and then, solving the equation yields x_8:

$$\frac{2c_{10}\mathrm{n}x_8^{1/2}+\mathrm{n}}{1+c_{10}\mathrm{x}_8^{1/2}}+\frac{0.5c_9\mathrm{m}x_8^{1/2}}{1+c_9\mathrm{x}_8^{1/2}}+\frac{2\mathrm{x}_8}{\mathrm{x}_{13}}-2\mathrm{r}=0$$

By substituting x_{13} and x_8 into the following equations, the independent variables can be estimated:

$$\mathrm{x}_6=\frac{\mathrm{n}x_{13}}{1+c_{10}\mathrm{x}_8^{1/2}}$$

$$\mathrm{x}_4=\frac{0.5\mathrm{m}x_{13}}{1+c_9\mathrm{x}_8^{1/2}}$$

$$\mathrm{x}_{11}=\mathrm{r}''\mathrm{x}_{13}$$

A.2. Partial derivatives of the mole fraction

The four functions and the four mole fractions are dependent on temperature, pressure and equivalence ratio. Partial derivatives with respect to temperature:

$$\frac{df_1}{dT}=\frac{d}{dT}\left[c_1x_4^{1/2}+2x_4+c_5x_4^{1/2}x_8^{1/2}+2c_9x_4x_8^{1/2}-\frac{m}{n}\left(x_6+c_{10}x_6x_8^{1/2}\right)\right]=0$$

$$\frac{df_2}{dT}=\frac{d}{dT}\left[c_2x_8^{1/2}+c_5x_4^{1/2}x_8^{1/2}+x_6+c_7x_8^{1/2}x_{11}^{1/2}+2x_8+c_9x_4x_8^{1/2}-\frac{2r}{n}\left(x_6+c_{10}x_6x_8^{1/2}\right)\right]=0$$

$$\frac{df_3}{dT}=\frac{d}{dT}\left[c_3x_{11}^{1/2}+c_7x_8^{1/2}x_{11}^{1/2}+x_{11}-\frac{2r'}{n}\left(x_6+c_{10}x_6x_8^{1/2}\right)\right]=0$$

$$\frac{df_4}{dT}=\frac{d}{dT}\left[\begin{array}{l} c_1x_4^{\frac{1}{2}}+c_2x_8^{\frac{1}{2}}+c_3x_{11}^{\frac{1}{2}}+x_4+c_5x_4^{\frac{1}{2}}x_8^{\frac{1}{2}}+x_6 \\ +c_7x_8^{\frac{1}{2}}x_{11}^{\frac{1}{2}}+2x_8+c_9x_4x_8^{1/2}+c_{10}x_6x_8^{1/2}+x_{11} \\ +\frac{r''}{n}\left(x_6+c_{10}x_6x_8^{1/2}\right)-1 \end{array}\right]$$

$$=0$$

$$\frac{df_1}{dT}=\frac{d(c_1x_4^{1/2})}{dT}+\frac{d(2x_4)}{dT}+\frac{d(c_5x_4^{1/2}x_8^{1/2})}{dT}+\frac{d(2c_9x_4x_8^{1/2})}{dT}+\frac{d}{dT}\left[-\frac{m}{n}\left(x_6+c_{10}x_6x_8^{1/2}\right)\right]$$

$$=\frac{d(c_1)}{dT}x_4^{1/2}+c_1\frac{d(x_4^{1/2})}{dT}+\frac{d(2x_4)}{dT}+\frac{d(c_5)}{dT}x_4^{1/2}x_8^{1/2}$$
$$+c_5\frac{d(x_4^{1/2}x_8^{1/2})}{dT}+\frac{d(2c_9)}{dT}x_4x_8^{1/2}+2c_9\frac{d(x_4x_8^{1/2})}{dT}-\frac{m}{n}\frac{d}{dT}(x_6)$$
$$-\frac{m}{n}\frac{d}{dT}(c_{10})x_6x_8^{1/2}-\frac{m}{n}c_{10}\frac{d}{dT}\left(x_6x_8^{1/2}\right)$$

$$=\frac{d(c_1)}{dT}x_4^{1/2}+c_1\frac{\partial(x_4^{1/2})}{\partial x_4}\frac{dx_4}{dT}+\frac{\partial(2x_4)}{\partial x_4}\frac{dx_4}{dT}+\frac{d(c_5)}{dT}x_4^{1/2}x_8^{1/2}$$
$$+c_5\frac{\partial(x_4^{1/2})}{\partial x_4}\frac{dx_4}{dT}x_8^{1/2}+c_5\frac{\partial(x_8^{1/2})}{\partial x_8}\frac{dx_8}{dT}x_4^{1/2}+\frac{d(2c_9)}{dT}x_4x_8^{1/2}$$
$$+2c_9\frac{\partial(x_4)}{\partial x_4}\frac{dx_4}{dT}x_8^{1/2}+2c_9\frac{\partial(x_8^{1/2})}{\partial x_8}\frac{dx_8}{dT}x_4-\frac{m}{n}\frac{\partial(x_6)}{\partial x_6}\frac{dx_6}{dT}$$
$$-\frac{m}{n}\frac{d\left(c_{10}\right)}{dT}x_6x_8^{1/2}-c_{10}\frac{m}{n}\frac{\partial(x_6)}{\partial x_6}\frac{dx_6}{dT}x_8^{1/2}-c_{10}\frac{m}{n}\frac{\partial(x_8^{1/2})}{\partial x_8}\frac{dx_8}{dT}x_6$$

$$=\left\{\frac{d(c_1)}{dT}x_4^{1/2}+\frac{d(c_5)}{dT}x_4^{1/2}x_8^{1/2}+\frac{d(2c_9)}{dT}x_4x_8^{1/2}-\frac{m}{n}\frac{d\left(c_{10}\right)}{dT}x_6x_8^{1/2}\right\}$$
$$+\left\{c_1\frac{\partial(x_4^{1/2})}{\partial x_4}+\frac{\partial(2x_4)}{\partial x_4}+c_5\frac{\partial(x_4^{1/2})}{\partial x_4}x_8^{1/2}+2c_9\frac{\partial(x_4)}{\partial x_4}x_8^{1/2}\right\}\frac{dx_4}{dT}$$
$$+\left\{-\frac{m}{n}\frac{\partial(x_6)}{\partial x_6}-c_{10}\frac{m}{n}\frac{\partial(x_6)}{\partial x_6}x_8^{1/2}\right\}\frac{dx_6}{dT}$$
$$+\left\{c_5\frac{\partial(x_8^{1/2})}{\partial x_8}x_4^{1/2}+2c_9\frac{\partial(x_8^{1/2})}{\partial x_8}x_4-c_{10}\frac{m}{n}\frac{\partial(x_8^{1/2})}{\partial x_8}x_6\right\}\frac{dx_8}{dT}$$

$$= \left\{ \frac{d(K_1 / P^{1/2})}{dT} x_4^{1/2} + \frac{d(K_5)}{dT} x_4^{1/2} x_8^{1/2} + \frac{d(2K_9 P^{1/2})}{dT} x_4 x_8^{1/2} - \frac{m}{n} \frac{d\left(K_{10} P^{1/2}\right)}{dT} x_6 x_8^{1/2} \right\}$$
$$+ \left\{ c_1 \frac{\partial(x_4^{1/2})}{\partial x_4} + \frac{\partial(2x_4)}{\partial x_4} + c_5 \frac{\partial(x_4^{1/2})}{\partial x_4} x_8^{1/2} + 2c_9 \frac{\partial(x_4)}{\partial x_4} x_8^{1/2} \right\} \frac{dx_4}{dT} + \left\{ -\frac{m}{n} \frac{\partial(x_6)}{\partial x_6} - c_{10} \frac{m}{n} \frac{\partial(x_6)}{\partial x_6} x_8^{1/2} \right\} \frac{dx_6}{dT}$$
$$+ \left\{ c_5 \frac{\partial(x_8^{1/2})}{\partial x_8} x_4^{1/2} + 2c_9 \frac{\partial(x_8^{1/2})}{\partial x_8} x_4 - c_{10} \frac{m}{n} \frac{\partial(x_8^{1/2})}{\partial x_8} x_6 \right\} \frac{dx_8}{dT}$$

Thus,

$$\frac{df_1}{dT} = \left\{ \frac{d(K_1)}{dT} \frac{x_4^{1/2}}{P^{1/2}} + \frac{d(K_5)}{dT} x_4^{1/2} x_8^{1/2} + \frac{d(K_9)}{dT} 2P^{1/2} x_4 x_8^{1/2} - \frac{m}{n} \frac{d\left(K_{10}\right)}{dT} P^{1/2} x_6 x_8^{1/2} \right\}$$
$$+ \left\{ \frac{1}{2} c_1 x_4^{-1/2} + 2 + \frac{1}{2} c_5 x_4^{-1/2} x_8^{1/2} + 2c_9 x_8^{1/2} \right\} \frac{dx_4}{dT} + \left\{ -\frac{m}{n} - c_{10} \frac{m}{n} x_8^{1/2} \right\} \frac{dx_6}{dT}$$
$$+ \left\{ \frac{1}{2} c_5 x_8^{-1/2} x_4^{1/2} + c_9 x_8^{-1/2} x_4 - \frac{1}{2} \frac{m}{n} c_{10} x_8^{-1/2} x_6 \right\} \frac{dx_8}{dT}$$

In a similar way,

$$\frac{df_2}{dT} = \left\{ \frac{dK_2}{dT} \frac{x_8^{1/2}}{P^{1/2}} + \frac{dK_5}{dT} x_4^{1/2} x_8^{1/2} + \frac{dK_7}{dT} x_8^{1/2} x_{11}^{1/2} + \frac{d(K_9)}{dT} P^{1/2} x_4 x_8^{1/2} + 2 \frac{d\left(K_{10}\right)}{dT} P^{1/2} x_6 x_8^{1/2} - \frac{2r}{n} \frac{d\left(K_{10}\right)}{dT} P^{1/2} x_6 x_8^{1/2} \right\}$$
$$+ \left\{ \frac{1}{2} c_5 x_4^{-1/2} x_8^{1/2} + c_9 x_8^{1/2} \right\} \frac{dx_4}{dT} + \left\{ 1 - \frac{2r}{n} (1 + c_{10} x_8^{\frac{1}{2}}) \right\} \frac{dx_6}{dT}$$

$$\frac{df_3}{dT} = \left\{ \frac{dK_3}{dT} \frac{x_{11}^{1/2}}{P^{1/2}} + \frac{dK_7}{dT} x_8^{1/2} x_{11}^{1/2} - \frac{2r'}{n} \frac{dK_{10}}{dT} P^{1/2} x_6 x_8^{1/2} \right\}$$
$$+ \left\{ -\frac{2r^{'}}{n} (1 + c_{10} x_8^{\frac{1}{2}}) \right\} \frac{dx_6}{dT} + \left\{ \frac{1}{2} c_7 x_8^{-1/2} x_{11}^{1/2} - \frac{2r'}{n} \frac{1}{2} c_{10} x_8^{-1/2} x_6 \right\} \frac{dx_8}{dT}$$
$$+ \left\{ \frac{1}{2} c_3 x_{11}^{-1/2} + \frac{1}{2} c_7 x_8^{1/2} x_{11}^{-1/2} + 1 \right\} \frac{dx_{11}}{dT}$$

$$\frac{df_4}{dT} = \left\{ \begin{array}{l} \frac{dK_1}{dT} \frac{x_4^{1/2}}{P^{1/2}} + \frac{dK_1}{dT} \frac{x_8^{1/2}}{P^{1/2}} + \frac{dK_3}{dT} \frac{x_{11}^{1/2}}{P^{1/2}} + \frac{dK_5}{dT} x_4^{1/2} x_8^{1/2} + \frac{dK_7}{dT} x_8^{\frac{1}{2}} x_{11}^{\frac{1}{2}} + \frac{dK_9}{dT} P^{1/2} x_4 x_8^{1/2} \\ + \frac{dK_{10}}{dT} P^{1/2} x_6 x_8^{1/2} + \frac{r^{''}}{n} \frac{dK_{10}}{dT} P^{1/2} x_6 x_8^{1/2} \end{array} \right\}$$
$$+ \left\{ \frac{1}{2} c_1 x_4^{-1/2} + 1 + \frac{1}{2} c_5 x_4^{-1/2} x_8^{1/2} + 2c_9 x_8^{1/2} \right\} \frac{dx_4}{dT}$$
$$+ \left\{ 1 + c_{10} x_8^{1/2} + \frac{r^{''}}{n} \left(1 + c_{10} x_8^{1/2}\right) \right\} \frac{dx_6}{dT}$$
$$+ \left\{ \frac{1}{2} c_2 x_8^{-1/2} + \frac{1}{2} c_5 x_8^{-1/2} x_4^{1/2} + \frac{1}{2} c_7 x_8^{-1/2} x_{11}^{1/2} + 2 + c_9 x_8^{-1/2} x_4 + \frac{1}{2} c_{10} x_8^{-1/2} x_6 + \frac{1}{2} \frac{r^{''}}{n} c_{10} x_8^{-1/2} x_6 \right\} \frac{dx_8}{dT}$$
$$+ \left\{ \frac{1}{2} c_3 x_{11}^{-1/2} + \frac{1}{2} c_7 x_8^{1/2} x_{11}^{-1/2} + 1 \right\} \frac{dx_{11}}{dT}$$

The equilibrium constants calculated based on JANAF Tables [32] by Olikara et al. [38] are expressed as:

$$\log K_p = A \cdot \ln T_A + \frac{B}{T_A} + C + D \cdot T_A + E \cdot T_A{}^2$$

where constants A, B, C, D, and E are shown in Table A 2.

T_A is defined as T/1000.

Table A 2 Equilibrium constants.

Constants / Reaction	A	B	C	D	E
$\frac{1}{2}H_2 \leftrightarrow H$	0.432168	-0.112464×10^{2}	0.267269×10^{1}	-0.745744×10^{-1}	0.242484×10^{-2}
$\frac{1}{2}O_2 \leftrightarrow O$	0.310805	-0.129540×10^{2}	0.321779×10^{1}	-0.738336×10^{-1}	0.344645×10^{-2}
$\frac{1}{2}N_2 \leftrightarrow N$	0.389716	-0.245828×10^{2}	0.314505×10^{1}	-0.963730×10^{-1}	0.585643×10^{-2}
$\frac{1}{2}H_2 + \frac{1}{2}O_2 \leftrightarrow OH$	−0.141784	-0.213308×10^{1}	0.853461	-0.355015×10^{-1}	$-0.310227\times10^{-}$
$\frac{1}{2}O_2 + \frac{1}{2}N_2 \leftrightarrow NO$	0.150879×10^{-1}	-0.470959×10^{1}	0.646096	0.272805×10^{-2}	$-0.154444\times10^{-}$
$H_2 + \frac{1}{2}O_2 \leftrightarrow H_2O$	−0.752364	0.124210×10^{2}	-0.260286×10^{1}	0.259556	$-0.162687\times10^{-}$
$CO + \frac{1}{2}O_2 \leftrightarrow CO_2$	-0.415302×10^{-2}	0.148627×10^{2}	-0.475746×10^{1}	0.124699	$-0.900227\times10^{-}$

APPENDIX B

This section is the summary of the work done by Szekely et al. [31]. The details of the derivation of mass at both stoichiometric and lean zones are shown. It is used to calculate the rate of heat release in the two-stage model.

B.1. Calculation of the initial mass of each zone

The initial mass of each zone is estimated as the following explanation. The total mass at the first stage is expressed as:

$$m_{total} = m_1 + m_2 + m_3 \quad \mathrm{m_{total} = m_1 + m_2 + m_3} \qquad \text{B 1}$$

The subscript indicator, i, is designated to be 1 for the burned stoichiometric-zone, 2 for the unburned stoichiometric-zone, 3 for the burned lean-zone, and 4 for the unburned lean-zone. The total mass of fuel and air is written as:

$$m_{a,total} = m_{a,1} + m_{a,2} + m_{a,3} \qquad \text{B 2}$$

$$m_{f,total} = m_{f,1} + m_{f,2} + m_{f,3} \qquad \text{B 3}$$

where subscripts *a* and *f* mean air and fuel, respectively.

By using the definition of equivalence ratio, it is expressed with the mass of fuel and air as

$$\phi_{avg} = \frac{m_{f,1} + m_{f,2} + m_{f,3}}{m_{a,1} + m_{a,2} + m_{a,3}} \cdot \frac{1}{FA_s} = \frac{m_{f,total}}{m_{a,total}} \cdot \frac{1}{FA_s} \qquad \text{B 4}$$

where ϕ_{avg} is average equivalence ratio

FA_s is stoichiometric fuel/air ratio.

The equivalence ratio of the burned stoichiometric-zone, for example, can be expressed with the following equation.

$$\phi_1 = \frac{m_{f,1}}{m_{a,1}} \cdot \frac{1}{FA_s} \qquad \text{B 5}$$

Multiplying by $m_{a,1}$ and, then, dividing by m_a yields

$$\frac{m_{a,1}}{m_{a,total}} \cdot \phi_1 = \frac{m_{f,1}}{m_{a,total}} \cdot \frac{1}{FA_s} \qquad \text{B 6}$$

Similarly, this manipulation can be applied to the other zones. Each manipulated results have the common denominator, $m_a \cdot FA_s$, so the overall equivalence ratio can be rewritten as

$$\begin{aligned} \phi_{avg} &= \frac{m_{f,total}}{m_{a,total}} \cdot \frac{1}{FA_s} \\ &= \frac{m_{f,1}}{m_{a,total}} \cdot \frac{1}{FA_s} + \frac{m_{f,2}}{m_{a,total}} \cdot \frac{1}{FA_s} + \frac{m_{f,3}}{m_{a,total}} \cdot \frac{1}{FA_s} \\ &= \frac{m_{a,1}}{m_{a,total}} \cdot \phi_1 + \frac{m_{a,2}}{m_{a,total}} \cdot \phi_2 + \frac{m_{a,3}}{m_{a,total}} \cdot \phi_3 \end{aligned} \qquad \text{B 7}$$

Arranging the overall equivalence ratio for $m_{a,2}$ gives

$$m_{a,2} = \frac{\left(m_{a,total} \cdot \phi_{avg} - m_{a,1} \cdot \phi_1 - m_{a,3} \cdot \phi_3\right)}{\phi_2} \qquad \text{B 8}$$

Substituting into $m_{a,2}$ the equation of total mass of air as

$$\begin{aligned} m_{a,total} &= m_{a1} + \mathrm{m}_{a2} + \mathrm{m}_{a3} \\ &= m_{a1} + \frac{\left(m_{a,total} \cdot \phi_{avg} - m_{a,1} \cdot \phi_1 - m_{a,3} \cdot \phi_3\right)}{\phi_2} + \mathrm{m}_{a3} \end{aligned} \qquad \text{B 9}$$

Rearranging above equation for the mass of air in the unburned lean-zone,

$$\mathrm{m}_{a,3} = \frac{\left(1-\frac{\phi_{avg}}{\phi_2}\right)\cdot m_{a,total} - \left(1-\frac{\phi_1}{\phi_2}\right)\cdot m_{a,1}}{\left(1-\frac{\phi_3}{\phi_2}\right)} \qquad \text{B 10}$$

As $\phi_1 = \phi_2$,

$$\mathrm{m}_{a,3} = \frac{\left(1-\frac{\phi_{avg}}{\phi_2}\right)\cdot m_{a,total}}{\left(1-\frac{\phi_3}{\phi_2}\right)} = \frac{\left(\phi_2-\phi_{avg}\right)}{\left(\phi_2-\phi_3\right)}\cdot m_{a,total} \qquad \text{B 11}$$

Since the total mass is expressed as

$$m_{total} = m_{a,total} + \mathrm{m}_{f,total} \qquad \text{B 12}$$

Dividing by $\mathrm{m}_{a,total}$ yields

$$\frac{m_{total}}{m_{a,total}} = 1+FA_{act} = 1+FA_s\cdot\phi_{avg}$$

$$m_{a,total} = \frac{m_{total}}{1+FA_s\cdot\phi} \qquad \text{B 13}$$

Similarly the mass of air in the unburned lean zone can be expressed as

$$m_{a,3} = \frac{m_3}{1+FA_s\cdot\phi_3} \qquad \text{B 14}$$

$$m_3 = m_{a,3}\cdot\left(1+FA_s\cdot\phi_3\right) \qquad \text{B 15}$$

Therefore, the total mass of the unburned lean zone can be calculated by substituting B11 and B13 into B15 as

$$
\begin{aligned}
m_3 &= m_{a,3} \cdot \left(1+FA_s \cdot \phi_3\right) \\
&= \frac{\left(\phi_2 - \phi_{avg}\right)}{\left(\phi_2 - \phi_3\right)} \cdot m_a \cdot \left(1+FA_s \cdot \phi_3\right) \\
&= \frac{\left(\phi_2 - \phi_{avg}\right)}{\left(\phi_2 - \phi_3\right)} \cdot \frac{m_{total}}{1+FA_s \cdot \phi_{avg}} \cdot \left(1+FA_s \cdot \phi_3\right) \\
&= \frac{\left(1+FA_s \cdot \phi_3\right)}{\left(1+FA_s \cdot \phi_{avg}\right)} \cdot \frac{\left(\phi_2 - \phi_{avg}\right)}{\left(\phi_2 - \phi_3\right)} \cdot m_{total}
\end{aligned}
\qquad \text{B 16}
$$

B.2. Stoichiometric-zone combustion with no fuel injection

The total cylinder mass is constant due to the assumption that stoichiometric-zone combustion takes place without fuel injection:

$$\frac{\mathrm{dm}}{\mathrm{d}\theta}=0 \qquad \text{B 17}$$

where θ designates the crank angle.

The mass of the unburned-lean zone does not change while the unburned-stoichiometric zone is combusting:

$$\frac{\mathrm{dm}_3}{\mathrm{d}\theta}=0 \qquad \text{B 18}$$

Since the total mass is constant and so is the mass of unburned-lean zone, the exchange between the burned and the unburned-stoichiometric zone can be expressed:

$$\frac{dm_2}{d\theta} = -\frac{dm_1}{d\theta} \qquad \text{B 19}$$

The unburned zones (unburned-stoichiometric and lean zone) have a uniform mixture without fuel injection. Thus, the ideal-gas constants for unburned zones are

constant. The differential derivative of the ideal-gas law can be simplified for the unburned-lean zone:

$$\frac{1}{p}\frac{dp}{d\theta}=\frac{1}{T_3}\frac{dT_3}{d\theta}-\frac{1}{V_3}\frac{dV_3}{d\theta},\frac{dR}{d\theta}=0 \qquad \text{B 20}$$

Unburned-stoichiometric zone:

$$\frac{1}{p}\frac{dp}{d\theta}=\frac{1}{m_2}\frac{dm_2}{d\theta}+\frac{1}{T_2}\frac{dT_2}{d\theta}-\frac{1}{V_2}\frac{dV_2}{d\theta} \qquad \text{B 21}$$

Rearrange the above equations for the volume derivative:

$$\frac{dV_2}{d\theta}=\frac{V_2}{T_2}\frac{dT_2}{d\theta}+\frac{V_2}{m_2}\frac{dm_2}{d\theta}-\frac{V_2}{p}\frac{dp}{d\theta}$$

where $\frac{dm_2}{d\theta}=-\frac{dm_1}{d\theta}$

Thus,

$$\frac{dV_2}{d\theta}=\frac{V_2}{T_2}\frac{dT_2}{d\theta}-\frac{V_2}{m_2}\frac{dm_1}{d\theta}-\frac{V_2}{p}\frac{dp}{d\theta} \qquad \text{B 22}$$

$$\frac{dV_3}{d\theta}=\frac{V_3}{T_3}\frac{dT_3}{d\theta}-\frac{V_3}{p}\frac{dp}{d\theta} \qquad \text{B 23}$$

The volume derivative of the burned-stoichiometric zone can be obtained by using the volume equation and the above equations as:

$$\begin{aligned}\frac{dV_1}{d\theta}&=\frac{dV}{d\theta}-\frac{dV_2}{d\theta}-\frac{dV_3}{d\theta}\\&=\frac{dV}{d\theta}-\left[\frac{V_2}{T_2}\frac{dT_2}{d\theta}-\frac{V_2}{m_2}\frac{dm_1}{d\theta}-\frac{V_2}{p}\frac{dp}{d\theta}\right]-\left[\frac{V_3}{T_3}\frac{dT_3}{d\theta}-\frac{V_3}{p}\frac{dp}{d\theta}\right]\\&=\frac{dV}{d\theta}+\frac{V_2}{m_2}\frac{dm_1}{d\theta}-\frac{V_2}{T_2}\frac{dT_2}{d\theta}-\frac{V_3}{T_3}\frac{dT_3}{d\theta}+\left(\frac{V_2+V_3}{p}\right)\frac{dp}{d\theta}\end{aligned} \qquad \text{B 24}$$

Since the exchange of mass between stoichiometric-zones occurs with the same equivalence ratio, there is no change of equivalence ratio. This is also true with the unburned-lean zone. Thus, the derivatives of ideal-gas constant and internal energy can be reduced as:

$$\frac{dR}{d\theta}=\frac{\partial R}{\partial p}\frac{dp}{d\theta}+\frac{\partial R}{\partial T}\frac{dT}{d\theta} \qquad \text{B 25}$$

$$\frac{du}{d\theta}=\frac{\partial u}{\partial p}\frac{dp}{d\theta}+\frac{\partial u}{\partial T}\frac{dT}{d\theta} \qquad \text{B 26}$$

Substituting all the above equations into the derivative of internal energy yields:

Burned-stoichiometric zone:

$$m_1\left(\frac{\partial u_1}{\partial p}\frac{dp}{d\theta}+\frac{\partial u_1}{\partial T_1}\frac{dT_1}{d\theta}\right)+u_1\frac{dm_1}{d\theta}=-p\frac{dV_1}{d\theta}+\frac{\delta Q_1}{d\theta}+h_1\frac{dm_1}{d\theta} \qquad \text{B 27}$$

Unburned-stoichiometric zone:

$$m_2\left(\frac{\partial u_2}{\partial p}\frac{dp}{d\theta}+\frac{\partial u_2}{\partial T_2}\frac{dT_2}{d\theta}\right)+u_2\frac{dm_2}{d\theta}=-p\frac{dV_2}{d\theta}+\frac{\delta Q_2}{d\theta}+h_2\frac{dm_2}{d\theta} \qquad \text{B 28}$$

Unburned-lean zone:

$$m_3\left(\frac{\partial u_3}{\partial p}\frac{dp}{d\theta}+\frac{\partial u_3}{\partial T_3}\frac{dT_3}{d\theta}\right)+u_3\frac{dm_3}{d\theta}=-p\frac{dV_3}{d\theta}+\frac{\delta Q_3}{d\theta} \qquad \text{B 29}$$

$$\text{where } \frac{dm_3}{d\theta}=0$$

By substituting equations B 22 and B 23 into equations B 28 and B 29, the temperature derivative for the two unburned zones can be obtained:

$$m_2\left(\frac{\partial u_2}{\partial p}\frac{dp}{d\theta}+\frac{\partial u_2}{\partial T_2}\frac{dT_2}{d\theta}\right)+u_2\frac{dm_2}{d\theta}=-p\left[\frac{V_2}{T_2}\frac{dT_2}{d\theta}-\frac{V_2}{m_2}\frac{dm_1}{d\theta}-\frac{V_2}{p}\frac{dp}{d\theta}\right]+\frac{\delta Q_2}{d\theta}+h_2\frac{dm_2}{d\theta}$$

$$\left(m_2\frac{\partial u_2}{\partial T_2}+p\frac{V_2}{T_2}\right)\frac{dT_2}{d\theta}+\left(m_2\frac{\partial u_2}{\partial p}-p\frac{V_2}{p}\right)\frac{dp}{d\theta}+\left(u_2-h_2\right)\frac{dm_2}{d\theta}-p\frac{V_2}{m_2}\frac{dm_1}{d\theta}=\frac{\delta Q_2}{d\theta}$$

where

$$\left(u_2-h_2\right)\frac{dm_2}{d\theta}-p\frac{V_2}{m_2}\frac{dm_1}{d\theta}=\left(u_2-h_2+p\frac{V_2}{m_2}\right)\frac{dm_2}{d\theta}$$

$$=\left[\left(u_2+p\frac{V_2}{m_2}\right)-h_2\right]\frac{dm_2}{d\theta}$$

$$=\left[h_2-h_2\right]\frac{dm_2}{d\theta}$$

$$=0$$

Thus,

$$\frac{dT_2}{d\theta}=\frac{\left[\left(V_2-m_2\frac{\partial u_2}{\partial p}\right)\frac{dp}{d\theta}+\frac{\delta Q_2}{d\theta}\right]}{\left(m_2\frac{\partial u_2}{\partial T_2}+p\frac{V_2}{T_2}\right)} \qquad \text{B 30}$$

Similarly,

$$\frac{dT_3}{d\theta}=\frac{\left[\left(V_3-m_3\frac{\partial u_2}{\partial p}\right)\frac{dp}{d\theta}+\frac{\delta Q_3}{d\theta}\right]}{\left(m_3\frac{\partial u_3}{\partial T_3}+p\frac{V_3}{T_3}\right)} \qquad \text{B 31}$$

For the burned-stoichiometric zone, substituting equation B 25 into the differentiated ideal gas equation yields the temperature derivative:

$$\frac{1}{p}\frac{dp}{d\theta}=\frac{1}{m_1}\frac{dm_1}{d\theta}+\frac{1}{R_1}\frac{dR_1}{d\theta}+\frac{1}{T_1}\frac{dT_1}{d\theta}-\frac{1}{V_1}\frac{dV_1}{d\theta}$$

$$\frac{1}{p}\frac{dp}{d\theta}=\frac{1}{m_1}\frac{dm_1}{d\theta}+\frac{1}{R_1}\left[\frac{\partial R_1}{\partial p}\frac{dp}{d\theta}+\frac{\partial R_1}{\partial T_1}\frac{dT_1}{d\theta}\right]+\frac{1}{T_1}\frac{dT_1}{d\theta}-\frac{1}{V_1}\frac{dV_1}{d\theta}$$

$$\left(\frac{1}{T_1}+\frac{1}{R_1}\frac{\partial R_1}{\partial T_1}\right)\frac{dT_1}{d\theta}=\left(\frac{1}{p}-\frac{1}{R_1}\frac{\partial R_1}{\partial p}\right)\frac{dp}{d\theta}+\frac{1}{V_1}\frac{dV_1}{d\theta}-\frac{1}{m_1}\frac{dm_1}{d\theta}$$

$$\frac{dT_1}{d\theta}=\frac{\left(\frac{1}{p}-\frac{1}{R_1}\frac{\partial R_1}{\partial p}\right)\frac{dp}{d\theta}+\frac{1}{V_1}\frac{dV_1}{d\theta}-\frac{1}{m_1}\frac{dm_1}{d\theta}}{\left(\frac{1}{T_1}+\frac{1}{R_1}\frac{\partial R_1}{\partial T_1}\right)} \qquad \text{B 32}$$

where $\alpha_1=\dfrac{1}{\left(\frac{1}{T_1}+\frac{1}{R_1}\frac{\partial R_1}{\partial T_1}\right)}$

The mass derivative of the burned-stoichiometric region can be expressed by substituting equations B 24 and B 32 into equation B 27:

$$m_1\left\{\alpha_1\frac{\partial u_1}{\partial T_1}\left[\left(\frac{1}{p}-\frac{1}{R_1}\frac{\partial R_1}{\partial p}\right)\frac{dp}{d\theta}+\frac{1}{V_1}\frac{dV_1}{d\theta}-\frac{1}{m_1}\frac{dm_1}{d\theta}\right]+\frac{\partial u_1}{\partial p}\frac{dp}{d\theta}\right\}+u_1\frac{dm_1}{d\theta}$$

$$=-p\frac{dV_1}{d\theta}+\frac{\delta Q_1}{d\theta}+h_1\frac{dm_1}{d\theta}$$

$$m_1\alpha_1\frac{\partial u_1}{\partial T_1}\left(\frac{1}{p}-\frac{1}{R_1}\frac{\partial R_1}{\partial p}\right)\frac{dp}{d\theta}+\frac{m_1\alpha_1}{V_1}\frac{\partial u_1}{\partial T_1}\frac{dV_1}{d\theta}-\frac{m_1\alpha_1}{m_1}\frac{\partial u_1}{\partial T_1}\frac{dm_1}{d\theta}+m_1\frac{\partial u_1}{\partial p}\frac{dp}{d\theta}+u_1\frac{dm_1}{d\theta}$$

$$=-p\frac{dV_1}{d\theta}+\frac{\delta Q_1}{d\theta}+h_1\frac{dm_1}{d\theta}$$

$$m_1\alpha_1\frac{\partial u_1}{\partial T_1}\left(\frac{1}{p}-\frac{1}{R_1}\frac{\partial R_1}{\partial p}\right)\frac{dp}{d\theta}-\alpha_1\frac{\partial u_1}{\partial T_1}\frac{dm_1}{d\theta}+m_1\frac{\partial u_1}{\partial p}\frac{dp}{d\theta}++u_1\frac{dm_1}{d\theta}$$

$$=-\left[\frac{m_1\alpha_1}{V_1}\frac{\partial u_1}{\partial T_1}+p\right]\frac{dV_1}{d\theta}+\frac{\delta Q_1}{d\theta}+h_1\frac{dm_1}{d\theta} \qquad \text{B 33}$$

Substituting equation B 24 into equation B 33:

$$m_1\alpha_1\frac{\partial u_1}{\partial T_1}\left(\frac{1}{p}-\frac{1}{R_1}\frac{\partial R_1}{\partial p}\right)\frac{dp}{d\theta}-\alpha_1\frac{\partial u_1}{\partial T_1}\frac{dm_1}{d\theta}+m_1\frac{\partial u_1}{\partial p}\frac{dp}{d\theta}+u_1\frac{dm_1}{d\theta}$$
$$=-\left[\frac{m_1\alpha_1}{V_1}\frac{\partial u_1}{\partial T_1}+p\right]\left[\frac{dV}{d\theta}+\frac{V_2}{m_2}\frac{dm_1}{d\theta}-\frac{V_2}{T_2}\frac{dT_2}{d\theta}-\frac{V_3}{T_3}\frac{dT_3}{d\theta}+\left(\frac{V_2+V_3}{p}\right)\frac{dp}{d\theta}\right]+\frac{\delta Q_1}{d\theta}+h_1\frac{dm_1}{d\theta}$$

$$\frac{dm_1}{d\theta}\left[-\alpha_1\frac{\partial u_1}{\partial T_1}+u_1-h_1+\frac{V_2}{m_2}\left(\frac{m_1\alpha_1}{V_2}\frac{\partial u_1}{\partial T_1}+p\right)\right]$$
$$=\frac{dT_2}{d\theta}\left[\frac{V_2}{T_2}\left(\frac{m_1\alpha_1}{V_1}\frac{\partial u_1}{\partial T_1}+p\right)\right]+\frac{dT_3}{d\theta}\left[\frac{V_3}{T_3}\left(\frac{m_1\alpha_1}{V_1}\frac{\partial u_1}{\partial T_1}+p\right)\right]-\frac{dV}{d\theta}\left[\frac{m_1\alpha_1}{V_1}\frac{\partial u_1}{\partial T_1}+p\right] \qquad \text{B 34}$$
$$+\frac{\delta Q_1}{d\theta}+\frac{dp}{d\theta}\left[-m_1\alpha_1\frac{\partial u_1}{\partial T_1}\left(\frac{1}{p}-\frac{1}{R_1}\frac{\partial R_1}{\partial p}\right)-m_1\frac{\partial u_1}{\partial p}-\frac{V_2}{T_2}\left(\frac{m_1\alpha_1}{V_1}\frac{\partial u_1}{\partial T_1}+p\right)\left(\frac{V_2+V_3}{p}\right)\right]$$

The left hand side:

$$\frac{dm_1}{d\theta}\left[-\alpha_1\frac{\partial u_1}{\partial T_1}+u_1-h_1+\frac{V_2}{m_2}\left(\frac{m_1\alpha_1}{V_2}\frac{\partial u_1}{\partial T_1}+p\right)\right]$$
$$=\frac{dm_1}{d\theta}\left[u_1-h_1-\alpha_1\left(1-\frac{V_2m_1}{m_2V_1}\right)\frac{\partial u_1}{\partial T_1}+\frac{pV_2}{m_2}\right]$$

where $\frac{pV_2}{m_2}=RT_2$ and $h_1=h_2$

Thus,

$$\frac{dm_1}{d\theta}\left[u_1-h-\alpha_1\left(1-\frac{V_2m_1}{m_2V_1}\right)\frac{\partial u_1}{\partial T_1}+RT_2\right]$$
$$=\frac{dm_1}{d\theta}\left[u_1-\left(h_1-RT_2\right)-\alpha_1\left(1-\frac{V_2m_1}{m_2V_1}\right)\frac{\partial u_1}{\partial T_1}\right]$$
$$=\frac{dm_1}{d\theta}\left[u_1-u_2-\alpha_1\left(1-\frac{V_2m_1}{m_2V_1}\right)\frac{\partial u_1}{\partial T_1}\right]$$

The right hand side,

$$\frac{dT_2}{d\theta}\left[\frac{V_2}{T_2}\left(\frac{m_1\alpha_1}{V_1}\frac{\partial u_1}{\partial T_1}+p\right)\right]+\frac{dT_3}{d\theta}\left[\frac{V_3}{T_3}\left(\frac{m_1\alpha_1}{V_1}\frac{\partial u_1}{\partial T_1}+p\right)\right]-\frac{dV}{d\theta}\left[\frac{m_1\alpha_1}{V_1}\frac{\partial u_1}{\partial T_1}+p\right]$$
$$+\frac{\delta Q_1}{d\theta}+\frac{dp}{d\theta}\left[-m_1\alpha_1\frac{\partial u_1}{\partial T_1}\left(\frac{1}{p}-\frac{1}{R_1}\frac{\partial R_1}{\partial p}\right)-m_1\frac{\partial u_1}{\partial p}-\frac{V_2}{T_2}\left(\frac{m_1\alpha_1}{V_1}\frac{\partial u_1}{\partial T_1}+p\right)\left(\frac{V_2+V_3}{p}\right)\right]$$
$$=\frac{dT_2}{d\theta}\left[\frac{pV_2}{T_2}+\alpha_1\frac{m_1V_2}{V_1T_2}\frac{\partial u_1}{\partial T_1}\right]+\frac{dT_3}{d\theta}\left[\frac{pV_3}{T_3}+\alpha_1\frac{m_1V_3}{V_1T_3}\frac{\partial u_1}{\partial T_1}\right]-\frac{dV}{d\theta}\left[\frac{m_1\alpha_1}{V_1}\frac{\partial u_1}{\partial T_1}+p\right]$$
$$+\frac{\delta Q_1}{d\theta}-\frac{dp}{d\theta}\left[V_2+V_3+m_1\frac{\partial u_1}{\partial p}+m_1\alpha_1\frac{\partial u_1}{\partial T_1}\left(\frac{1}{p}-\frac{1}{R_1}\frac{\partial R_1}{\partial p}+\frac{V_2+V_3}{V_1p}\right)\right]$$

Therefore, equation B 34 is rewritten as:

$$\frac{dm_1}{d\theta}\left[u_1-u_2-\alpha_1\left(1-\frac{V_2m_1}{m_2V_1}\right)\frac{\partial u_1}{\partial T_1}\right]$$
$$=\frac{dT_2}{d\theta}\left[\frac{pV_2}{T_2}+\alpha_1\frac{m_1V_2}{V_1T_2}\frac{\partial u_1}{\partial T_1}\right]+\frac{dT_3}{d\theta}\left[\frac{pV_3}{T_3}+\alpha_1\frac{m_1V_3}{V_1T_3}\frac{\partial u_1}{\partial T_1}\right]-\frac{dV}{d\theta}\left[\frac{m_1\alpha_1}{V_1}\frac{\partial u_1}{\partial T_1}+p\right]$$
$$+\frac{\delta Q_1}{d\theta}-\frac{dp}{d\theta}\left[V_2+V_3+m_1\frac{\partial u_1}{\partial p}+m_1\alpha_1\frac{\partial u_1}{\partial T_1}\left(\frac{1}{p}-\frac{1}{R_1}\frac{\partial R_1}{\partial p}+\frac{V_2+V_3}{V_1p}\right)\right]$$

$$\frac{dm_1}{d\theta}=\frac{\left\{\begin{array}{l}\left[\frac{dT_2}{d\theta}\left[\frac{pV_2}{T_2}+\alpha_1\frac{m_1V_2}{V_1T_2}\frac{\partial u_1}{\partial T_1}\right]+\frac{dT_3}{d\theta}\left[\frac{pV_3}{T_3}+\alpha_1\frac{m_1V_3}{V_1T_3}\frac{\partial u_1}{\partial T_1}\right]-\frac{dV}{d\theta}\left[\frac{m_1\alpha_1}{V_1}\frac{\partial u_1}{\partial T_1}+p\right]\right]\\+\frac{\delta Q_1}{d\theta}-\frac{dp}{d\theta}\left[V_2+V_3+m_1\frac{\partial u_1}{\partial p}+m_1\alpha_1\frac{\partial u_1}{\partial T_1}\left(\frac{1}{p}-\frac{1}{R_1}\frac{\partial R_1}{\partial p}+\frac{V_2+V_3}{V_1p}\right)\right]\end{array}\right\}}{\left[u_1-u_2-\alpha_1\left(1-\frac{V_2m_1}{m_2V_1}\right)\frac{\partial u_1}{\partial T_1}\right]}$$

B.3. Lean-zone combustion with no product mixing

Since only the unburned-lean zone is combusting, the mass of the burned-stoichiometric zone is constant:

$$\frac{dm_1}{d\theta} = 0 \qquad \text{B 35}$$

Since only the exchange of mass between lean-zones takes place, the relation can be expressed as:

$$\frac{dm_4}{d\theta} = -\frac{dm_3}{d\theta} \qquad \text{B 36}$$

For the burned-stoichiometric zone, there is no mass change. Thus, the differential form of ideal gas constant can be written as:

$$\frac{dR_1}{d\theta} = \frac{\partial R_1}{\partial p}\frac{dp}{d\theta} + \frac{\partial R_1}{\partial T_1}\frac{dT_1}{d\theta} \qquad \text{B 37}$$

Similarly before, the derivative of the ideal gas law can be expressed as:

$$\frac{1}{p}\frac{dp}{d\theta} = \frac{1}{m_1}\frac{dm_1}{d\theta} + \frac{1}{R_1}\frac{dR_1}{d\theta} + \frac{1}{T_1}\frac{dT_1}{d\theta} - \frac{1}{V_1}\frac{dV_1}{d\theta} \qquad \text{B 38}$$

where $\frac{dm_1}{d\theta} = 0$

Substituting equation B 37 into equation B 38 yields:

$$\frac{1}{p}\frac{dp}{d\theta} = \frac{1}{m_1}\frac{dm_1}{d\theta} + \frac{1}{R_1}\left[\frac{\partial R_1}{\partial p}\frac{dp}{d\theta} + \frac{\partial R_1}{\partial T_1}\frac{dT_1}{d\theta}\right] + \frac{1}{T_1}\frac{dT_1}{d\theta} - \frac{1}{V_1}\frac{dV_1}{d\theta}$$

$$\frac{1}{V_1}\frac{dV_1}{d\theta} = \left[\frac{1}{T_1} + \frac{1}{R_1}\frac{\partial R_1}{\partial T_1}\right]\frac{dT_1}{d\theta} - \left[\frac{1}{p} - \frac{1}{R_1}\frac{\partial R_1}{\partial p}\right]\frac{dp}{d\theta}$$

$$\frac{dV_1}{d\theta}=\left[\frac{V_1}{T_1}+\frac{V_1}{R_1}\frac{\partial R_1}{\partial p}\right]\frac{dT_1}{d\theta}-\left[\frac{V_1}{p}-\frac{V_1}{R_1}\frac{\partial R_1}{\partial p}\right]\frac{dp}{d\theta} \qquad \text{B 39}$$

For the unburned-lean zone, the derivative of the ideal gas law can be written as below and it is rearranged in respect of volume:

$$\frac{1}{p}\frac{dp}{d\theta}=\frac{1}{m_3}\frac{dm_3}{dc}+\frac{1}{R_3}\frac{dR_3}{d\theta}+\frac{1}{T_3}\frac{dT_3}{d\theta}-\frac{1}{V_3}\frac{dV_3}{d\theta}$$

where $\frac{dR_3}{dc}=0$

Thus,

$$\frac{dV_3}{d\theta}=\frac{V_3}{T_3}\frac{dT_3}{d\theta}+\frac{V_3}{m_3}\frac{dm_3}{d\theta}-\frac{V_3}{p}\frac{dp}{d\theta} \qquad \text{B 40}$$

An expression for the volume derivative of the burned-lean zone can be induced as:

$$\frac{dV_4}{d\theta}=\frac{dV}{d\theta}-\frac{dV_1}{d\theta}-\frac{dV_3}{d\theta}$$

$$=\frac{dV}{d\theta}-\left\{\left[\frac{V_1}{T_1}+\frac{V_1}{R_1}\frac{\partial R_1}{\partial p}\right]\frac{dT_1}{d\theta}-\left[\frac{V_1}{p}-\frac{V_1}{R_1}\frac{\partial R_1}{\partial p}\right]\frac{dp}{d\theta}\right\}-\left\{\frac{V_3}{T_3}\frac{dT_3}{d\theta}+\frac{V_3}{m_3}\frac{dm_3}{d\theta}-\frac{V_3}{p}\frac{dp}{d\theta}\right\}$$

where $\frac{dm_3}{d\theta}=-\frac{dm_4}{d\theta}$

Thus,

$$\frac{dV_4}{d\theta}=\frac{dV}{d\theta}-\frac{V_3}{m_3}\frac{dm_3}{d\theta}-\left[\frac{V_1}{T_1}+\frac{V_1}{R_1}\frac{\partial R_1}{\partial p}\right]\frac{dT_1}{d\theta}-\frac{V_3}{T_3}\frac{dT_3}{d\theta}+\left[\frac{V_1+V_3}{p}-\frac{V_1}{R_1}\frac{\partial R_1}{\partial p}\right]\frac{dp}{d\theta} \qquad \text{B 41}$$

The energy equation of each zone can be written similarly to the previous derivations as:

$$m_1\left(\frac{\partial u_1}{\partial p}\frac{dp}{d\theta}+\frac{\partial u_1}{\partial T_1}\frac{dT_1}{d\theta}\right)+u_1\frac{dm_1}{d\theta}=-p\frac{dV_1}{d\theta}+\frac{\delta Q_1}{d\theta} \qquad \text{B 42}$$

$$m_3\left(\frac{\partial u_3}{\partial p}\frac{dp}{d\theta}+\frac{\partial u_3}{\partial T_3}\frac{dT_3}{d\theta}\right)+u_3\frac{dm_3}{d\theta}=-p\frac{dV_3}{d\theta}+\frac{\delta Q_3}{d\theta}+h_3\frac{dm_3}{d\theta} \qquad \text{B 43}$$

And

$$m_4\left(\frac{\partial u_4}{\partial p}\frac{dp}{d\theta}+\frac{\partial u_4}{\partial T_4}\frac{dT_4}{d\theta}\right)+u_4\frac{dm_4}{d\theta}=-p\frac{dV_4}{d\theta}+\frac{\delta Q_4}{d\theta}+h_4\frac{dm_4}{d\theta} \qquad \text{B 44}$$

In order to obtain the temperature derivatives for the burned stoichiometric and the unburned-lean zones, equations B 39 and B 40 are substituted into equations B 42 and B 43.

Burned-stoichiometric zone:

$$m_1\left(\frac{\partial u_1}{\partial p}\frac{dp}{d\theta}+\frac{\partial u_1}{\partial T_1}\frac{dT_1}{d\theta}\right)+u_1\frac{dm_1}{d\theta}=-p\left\{\left[\frac{V_1}{T_1}+\frac{V_1}{R_1}\frac{\partial R_1}{\partial T_1}\right]\frac{dT_1}{d\theta}-\left[\frac{V_1}{p}-\frac{V_1}{R_1}\frac{\partial R_1}{\partial p}\right]\frac{dp}{d\theta}\right\}+\frac{\delta Q_1}{d\theta}$$

$$\frac{dT_1}{d\theta}\left[m_1\frac{\partial u_1}{\partial T_1}+\frac{pV_1}{T_1}+\frac{pV_1}{R_1}\frac{\partial R_1}{\partial T_1}\right]=\left[V_1-\frac{pV_1}{R_1}\frac{\partial R_1}{\partial p}-m_1\frac{\partial u_1}{\partial p}\right]\frac{dp}{d\theta}+\frac{\delta Q_1}{d\theta}$$

where $\frac{pV_1}{R_1}=m_1T_1$

Thus,

$$\frac{dT_1}{d\theta}=\frac{\left[V_1-\frac{pV_1}{R_1}\frac{\partial R_1}{\partial p}-m_1\frac{\partial u_1}{\partial p}\right]\frac{dp}{d\theta}+\frac{\delta Q_1}{d\theta}}{\left[m_1\frac{\partial u_1}{\partial T_1}+\frac{pV_1}{T_1}+m_1T_1\frac{\partial R_1}{\partial T_1}\right]} \qquad \text{B 45}$$

Similarly, the energy equation of the burned-stoichiometric region is rearranged as:

$$m_3\left(\frac{\partial u_3}{\partial p}\frac{dp}{d\theta}+\frac{\partial u_3}{\partial T_3}\frac{dT_3}{d\theta}\right)+u_3\frac{dm_3}{d\theta}=-p\left[\frac{V_3}{T_3}\frac{dT_3}{d\theta}+\frac{V_3}{m_3}\frac{dm_3}{d\theta}-\frac{V_3}{p}\frac{dp}{d\theta}\right]+\frac{\delta Q_3}{d\theta}+h_3\frac{dm_3}{d\theta}$$

$$\frac{dT_3}{d\theta}\left[m_3\frac{\partial u_3}{\partial T_3}+\frac{pV_3}{T_3}\right]=\frac{dp}{d\theta}\left[V_3-m_3\frac{\partial u_3}{\partial p}\right]+\left[h_3-u_3\right]\frac{dm_3}{d\theta}+\frac{\delta Q_3}{d\theta}$$

$$\text{Since}\frac{dm_3}{d\theta}=0,\ \frac{dT_3}{d\theta}=\frac{\frac{dp}{d\theta}\left[V_3-m_3\frac{\partial u_3}{\partial p}\right]+\frac{\delta Q_3}{d\theta}}{\left[m_3\frac{\partial u_3}{\partial T_3}+\frac{pV_3}{T_3}\right]} \qquad \text{B 46}$$

For the unburned-lean zone, the temperature derivative is obtained as following:

$$\frac{1}{p}\frac{dp}{d\theta}=\frac{1}{m_4}\frac{dm_4}{d\theta}+\frac{1}{R_4}\frac{dR_4}{d\theta}+\frac{1}{T_4}\frac{dT_4}{d\theta}-\frac{1}{V_4}\frac{dV_4}{d\theta}$$

$$\text{where}\ \frac{dR_4}{d\theta}=\frac{\partial R_4}{\partial p}\frac{dp}{d\theta}+\frac{\partial R_4}{\partial T_4}\frac{dT_4}{d\theta}$$

Thus,

$$\frac{1}{p}\frac{dp}{d\theta}=\frac{1}{m_4}\frac{dm_4}{d\theta}+\frac{1}{R_4}\left[\frac{\partial R_4}{\partial p}\frac{dp}{d\theta}+\frac{\partial R_4}{\partial T_4}\frac{dT_4}{d\theta}\right]+\frac{1}{T_4}\frac{dT_4}{d\theta}-\frac{1}{V_4}\frac{dV_4}{d\theta}$$

$$\frac{dT_4}{d\theta}\left[\frac{1}{T_4}+\frac{1}{R_4}\frac{\partial R_4}{\partial T_4}\right]=\left[\frac{1}{p}-\frac{1}{R_4}\frac{\partial R_4}{\partial p}\right]\frac{dp}{d\theta}+\frac{1}{V_4}\frac{dV_4}{d\theta}-\frac{1}{m_4}\frac{dm_4}{d\theta}$$

$$\frac{dT_4}{d\theta}=\frac{\left[\frac{1}{p}-\frac{1}{R_4}\frac{\partial R_4}{\partial p}\right]\frac{dp}{d\theta}+\frac{1}{V_4}\frac{dV_4}{d\theta}-\frac{1}{m_4}\frac{dm_4}{d\theta}}{\left[\frac{1}{T_4}+\frac{1}{R_4}\frac{\partial R_4}{\partial T_4}\right]}$$

$$\frac{dT_4}{d\theta}=\alpha_4\left[\frac{1}{p}-\frac{1}{R_4}\frac{\partial R_4}{\partial p}\right]\frac{dp}{d\theta}+\frac{1}{V_4}\frac{dV_4}{d\theta}-\frac{1}{m_4}\frac{dm_4}{d\theta} \qquad \text{B 47}$$

where $\alpha_4 = \dfrac{1}{\left[\dfrac{1}{T_4} + \dfrac{1}{R_4}\dfrac{\partial R_4}{\partial T_4}\right]}$

The mass derivative for the burned-lean region can be obtained by substituting equations B 45 and B 47 into the expanded energy equation B 44:

$$m_4\left(\frac{\partial u_4}{\partial p}\frac{dp}{d\theta} + \frac{\partial u_4}{\partial T_4}\frac{dT_4}{d\theta}\right) + u_4\frac{dm_4}{d\theta} = -p\frac{dV_4}{d\theta} + \frac{\delta Q_4}{d\theta} + h_4\frac{dm_4}{d\theta}$$

$$m_4\left\{\frac{\partial u_4}{\partial p}\frac{dp}{d\theta} + \frac{\partial u_4}{\partial T_4}\alpha_4\left[\left(\frac{1}{p} - \frac{1}{R_4}\frac{\partial R_4}{\partial p}\right)\frac{dp}{d\theta} + \frac{1}{V_4}\frac{dV_4}{d\theta} - \frac{1}{m_4}\frac{dm_4}{d\theta}\right]\right\} + u_4\frac{dm_4}{d\theta} = -p\frac{dV_4}{d\theta} + \frac{\delta Q_4}{d\theta} + h_4\frac{dm_4}{d\theta}$$

$$m_4\left\{\frac{\partial u_4}{\partial p}\frac{dp}{d\theta} + \frac{\partial u_4}{\partial T_4}\alpha_4\left[\left(\frac{1}{p} - \frac{1}{R_4}\frac{\partial R_4}{\partial p}\right)\frac{dp}{d\theta} - \frac{1}{m_4}\frac{dm_4}{d\theta}\right]\right\} + u_4\frac{dm_4}{d\theta} = \left(-p - \alpha_4\frac{m_4}{V_4}\frac{\partial u_4}{\partial T_4}\right)\frac{dV_4}{d\theta} + \frac{\delta Q_4}{d\theta} + h_4\frac{dm_4}{d\theta}$$

$$m_4\left\{\frac{\partial u_4}{\partial p}\frac{dp}{d\theta} + \alpha_4\frac{\partial u_4}{\partial T_4}\left[\left(\frac{1}{p} - \frac{1}{R_4}\frac{\partial R_4}{\partial p}\right)\frac{dp}{d\theta} - \frac{1}{m_4}\frac{dm_4}{d\theta}\right]\right\} + u_4\frac{dm_4}{d\theta}$$

$$= \left(-p - \alpha_4\frac{m_4}{V_4}\frac{\partial u_4}{\partial T_4}\right)\left\{\frac{dV}{d\theta} - \frac{V_3}{m_3}\frac{dm_3}{d\theta} - \left[\frac{V_1}{T_1} + \frac{V_1}{R_1}\frac{\partial R_1}{\partial p}\right]\frac{dT_1}{d\theta} - \frac{V_3}{T_3}\frac{dT_3}{d\theta} + \left[\frac{V_1 + V_3}{p} - \frac{V_1}{R_1}\frac{\partial R_1}{\partial p}\right]\frac{dp}{d\theta}\right\} + \frac{\delta Q_4}{d\theta} + h_4\frac{dm_4}{d\theta}$$

$$\begin{aligned}
&\frac{dm_4}{d\theta}\left[-m_4\alpha_4\frac{\partial u_4}{\partial T_4} + u_4 + \left(p + \alpha_4\frac{m_4}{V_4}\frac{\partial u_4}{\partial T_4}\right)\frac{V_3}{m_3} - h_4\right] \\
&= \frac{dT_1}{d\theta}\left[\left(p + \alpha_4\frac{m_4}{V_4}\frac{\partial u_4}{\partial T_4}\right)\left(\frac{V_1}{T_1} + \frac{V_1}{R_1}\frac{\partial R_1}{\partial p}\right)\right] + \frac{dT_3}{d\theta}\left[\frac{V_3}{T_3}\left(p + \alpha_4\frac{m_4}{V_4}\frac{\partial u_4}{\partial T_4}\right)\right] \\
&- \frac{dV}{d\theta}\left(p + \alpha_4\frac{m_4}{V_4}\frac{\partial u_4}{\partial T_4}\right) \\
&- \frac{dp}{d\theta}\left\{\alpha_4 m_4\frac{\partial u_4}{\partial T_4}\left[\left(\frac{1}{p} - \frac{1}{R_4}\frac{\partial R_4}{\partial p}\right) + m_4\frac{\partial u_4}{\partial p} + \left(p + \alpha_4\frac{m_4}{V_4}\frac{\partial u_4}{\partial T_4}\right)\left(\frac{V_1 + V_3}{p} - \frac{V_1}{R_1}\frac{\partial R_1}{\partial p}\right)\right]\right\} \\
&+ \frac{\delta Q_4}{d\theta}
\end{aligned} \qquad \text{B 48}$$

The right hand side of the above equation is rearranged as:

$$\frac{dm_4}{d\theta}\left[-m_4\alpha_4\frac{\partial u_4}{\partial T_4}+u_4+\left(p+\alpha_4\frac{m_4}{V_4}\frac{\partial u_4}{\partial T_4}\right)\frac{V_3}{m_3}-h_4\right]=\frac{dm_4}{d\theta}\left[u_4-\left(h_4-\frac{pV_3}{m_3}\right)-\alpha_4\left(1-\frac{V_3m_4}{V_4m_3}\right)\frac{\partial u_4}{\partial T_4}\right]$$

Since $\frac{pV_3}{m_3}=RT_3$ and $h_3=h_4$,

$$\frac{dm_4}{d\theta}\left[-m_4\alpha_4\frac{\partial u_4}{\partial T_4}+u_4+\left(p+\alpha_4\frac{m_4}{V_4}\frac{\partial u_4}{\partial T_4}\right)\frac{V_3}{m_3}-h_4\right]=\frac{dm_4}{d\theta}\left[u_4-u_3-\alpha_4\left(1-\frac{V_3m_4}{V_4m_3}\right)\frac{\partial u_4}{\partial T_4}\right]$$

Therefore, equation B 48 is rewritten as following:

$$\begin{aligned}
&\frac{dm_4}{d\theta}\left[u_4-u_3-\alpha_4\left(1-\frac{V_3m_4}{V_4m_3}\right)\frac{\partial u_4}{\partial T_4}\right]\\
&=\frac{dT_1}{d\theta}\left[\left(p+\alpha_4\frac{m_4}{V_4}\frac{\partial u_4}{\partial T_4}\right)\left(\frac{V_1}{T_1}+\frac{V_1}{R_1}\frac{\partial R_1}{\partial p}\right)\right]+\frac{dT_3}{d\theta}\left[\frac{V_3}{T_3}\left(p+\alpha_4\frac{m_4}{V_4}\frac{\partial u_4}{\partial T_4}\right)\right]\\
&-\frac{dV}{d\theta}\left(p+\alpha_4\frac{m_4}{V_4}\frac{\partial u_4}{\partial T_4}\right)\\
&-\frac{dp}{d\theta}\left\{V_1+V_3+m_4\frac{\partial u_4}{\partial p}-\frac{pV_1}{R_1}\frac{\partial R_1}{\partial p}+\alpha_4m_4\frac{\partial u_4}{\partial T_4}\left(\frac{1}{p}-\frac{1}{R_4}\frac{\partial R_4}{\partial p}+\frac{V_1+V_3}{pV_4}-\frac{V_1}{V_4R_1}\frac{\partial R_1}{\partial p}\right)\right\}\\
&+\frac{\delta Q_4}{d\theta}
\end{aligned}$$

$$\frac{dm_4}{d\theta}=\frac{\left\{\begin{array}{l}\frac{dT_1}{d\theta}\left[\left(p+\alpha_4\frac{m_4}{V_4}\frac{\partial u_4}{\partial T_4}\right)\left(\frac{V_1}{T_1}+\frac{V_1}{R_1}\frac{\partial R_1}{\partial p}\right)\right]+\frac{dT_3}{d\theta}\left[\frac{V_3}{T_3}\left(p+\alpha_4\frac{m_4}{V_4}\frac{\partial u_4}{\partial T_4}\right)\right]\\ -\frac{dV}{d\theta}\left(p+\alpha_4\frac{m_4}{V_4}\frac{\partial u_4}{\partial T_4}\right)\\ -\frac{dp}{d\theta}\left\{V_1+V_3+m_4\frac{\partial u_4}{\partial p}-\frac{pV_1}{R_1}\frac{\partial R_1}{\partial p}+\alpha_4m_4\frac{\partial u_4}{\partial T_4}\left(\frac{1}{p}-\frac{1}{R_4}\frac{\partial R_4}{\partial p}+\frac{V_1+V_3}{pV_4}-\frac{V_1}{V_4R_1}\frac{\partial R_1}{\partial p}\right)\right\}\\ +\frac{\delta Q_4}{d\theta}\end{array}\right\}}{\left[u_4-u_3-\alpha_4\left(1-\frac{V_3m_4}{V_4m_3}\right)\frac{\partial u_4}{\partial T_4}\right]} \qquad \text{B 49}$$

VITA

Name: Hoseok Song

Address: Department of Mechanical Engineering
College of Engineering
Texas A&M University
3123 TAMU
College Station, TX 77843

Email Address: hoseok.song@gmail.com

Education: B.S., Mechanical Engineering, Inha University, 2004
M.S., Mechanical Engineering, Kansas State University, 2007
PhD., Mechanical Engineering, Texas A&M University, 2012